Highly Reliable and Low Temperature Process for Amorphous Oxide Thin-Film Transistors toward Flexible Displays

（フレキシブルディスプレイ実現に向けた非晶質酸化物薄膜トランジスタの高信頼性実現と低温プロセス）

June 2015

Juan Paolo BERMUNDO

Graduate School of Materials Science

Nara Institute of Science and Technology

To my loved ones

Abstract

The growth of society is largely influenced by the availability of information and its effective dissemination. Displays are one of the most efficient terminals used to show and disseminate information. It is not surprising, therefore, that most information and communication devices include displays. Central to modern displays are thin-film transistors (TFTs) which act as switches to control individual pixels and sometimes as current drivers in the display circuit. Amorphous silicon (*a*-Si) is the de facto material that is used as channel material for TFTs. However, for next-generation displays which require transparency, flexibility, and high performance, *a*-Si is not an appropriate channel material. Amorphous Indium-Gallium-Zinc-Oxide (*a*-IGZO) has been tagged as the material that will fulfill these requirements. It has a wide band gap (~3.2 eV), can be processed at room temperature, and has mobility more than ten times higher than *a*-Si. Moreover, because it is amorphous, it can be used in large area applications. Deposition can also be performed via solution process or printing which makes it more attractive.

Nevertheless, stability is a major issue for *a*-IGZO. Instability is due to many factors and some of these mechanisms are not yet well understood. There are three key locations where degradation is most common: the gate insulator and its interface with the channel, the channel bulk, and the backchannel. Ambient effects at the backchannel are main causes of instability which is why passivation layers are mandatory. Several passivation layers have been proposed most of them inorganic. Inorganic passivation materials, however, require a more complicated vacuum process and can induce process damage during fabrication. Organic passivation materials can be fabricated in a simpler manner but their performance is not very good. Another issue in *a*-IGZO is that annealing up to 400 ^{o}C is required to ensure good electrical characteristics and stability. This high

temperature is not compatible with most flexible materials. In this thesis, an organic-inorganic hybrid passivation material based on polysilsesquioxane (PSQ) is introduced. Two types of PSQ are introduced: non-photosensitive and photosensitive and their merits are discussed. Different mechanisms on how it improves the stability are examined. This study also demonstrates the use of excimer laser annealing (ELA) as a low temperature annealing alternative. These methods are critical in developing stable devices for transparent and flexible applications.

This thesis is divided into 5 chapters. Chapter 1 gives a brief history of displays and TFTs. Properties, stability issues, and future applications of *a*-IGZO are discussed. Identification of the problem and objectives of the thesis can also be found in this chapter.

Chapter 2 starts by giving an overview of the two major types of passivation layers: inorganic and organic layers. Non-photosensitive PSQ passivation layers are then introduced. Reliability of *a*-IGZO TFT passivated with non-photosensitive PSQ was tested by subjecting them to humidity stress and three different types of bias stress: positive bias stress, negative bias stress, and negative bias illumination stress. For comparison, the reliability of unpassivated *a*-IGZO TFTs was also tested. Results show the impressive reliability of PSQ passivated *a*-IGZO TFTs after each stress. The voltage threshold (V_{th}) shift recorded was very small – much better compared to organic passivation layers, and comparable to inorganic passivation layers. Elemental analysis by secondary ion mass spectrometry (SIMS) reveals that large amount of hydrogen and carbon is introduced into the *a*-IGZO channel after passivation. In addition, XPS analysis uncovers a reduction in oxygen vacancies (V_O) and an increase in the hydrogen and carbon related bonds. This implies that both H and C occupy the V_O site. However, further analysis reveals that formation energy of C at V_O site (C_O) is quite high and that C

plus two oxygen interstitials substituting at Zn site ($C_{Zn} + 2_{Oi}$), which is an acceptor, is more probable. The V_O reduction, formation of additional acceptor states, and the superb barrier ability of the non-photosensitive PSQ explain its impressive reliability.

Chapter 3 first describes the potential process damage that can be induced while fabricating *a*-IGZO TFTs. Central to this is the plasma damage incurred by TFTs when passivation contact holes are formed. Plasma damage causes the V_{th} to shift negatively. The development and use of photosensitive PSQ on *a*-IGZO TFTs are discussed in this chapter. Photosensitive PSQ enables the fabrication of passivation layers with contact holes without any use of dry etching, thus preventing process damage. Like in the non-photosensitive case, the photosensitive PSQ was effective against humidity and bias stress. Furthermore, hump effect in the transfer characteristics before and after bias stress was suppressed. A high amount of C and H in the channel was also revealed by SIMS. In addition, a high amount of fluorine was present in the channel region. Analysis shows that F reduced the V_O and stabilized weak oxygen and hydroxide bonds.

Chapter 4 discusses the necessity of annealing in improving the electrical characteristics and stability. ELA, a low temperature annealing alternative, was performed on already-passivated *a*-IGZO TFTs. Two types of ELA were analyzed: XeCl ELA and KrF ELA. Results show that both ELA types are effective in improving the electrical characteristics. COMSOL Multiphysics shows heating localization in the upper layers and that temperature at the substrate is very low (<30 ^{o}C). X-ray diffraction measurements reveal that the *a*-IGZO is still amorphous after ELA. Introduction of C and H from the passivation is also observed, although most are confined in the top few nm and at the interface.

Chapter 5 discusses the conclusions derived from this study and presents several

suggestions for future work. Pertinent challenges that need to be addressed are identified and possible solutions are proposed.

Contents

Chapter 1
Introduction

1.1 Background

Society is built through information and its effective dissemination. Several technologies have been developed to effectively relay information to a growing number of people. These technologies are categorized into printed media such as newspapers, books, and magazines; audio media such as radio and music; video media such as television and film; and digital media such as computer games, content hosted in the internet, and all other types of media saved in a digital format. Displays are very important in two of these media types, which are video and digital media. For instance, displays enable people to see content and are faster and more versatile than printed media in displaying information. While the information in printed media is static, the information relayed in televisions or any display device is dynamic. Furthermore, compared to audio media like radio, information on a display is more permanent unlike in radio wherein the relayed information is fleeting.

Computers and other devices such as smartphones are needed to access and consume digital media. In this case, displays have been the de facto method by which a user can interact with these devices. The role of displays as a bridge or interface between humans and devices is highlighted by the way phones have been built in the past few decades. Fig 1.1 shows the evolution of mobile phones over the past few decades starting with the introduction of Motorola DynaTAC 8000x in 1984. Older phones had visible antennas and were quite bulky and thick. As advancements in technology were developed,

phones became smaller, portable, and powerful. The computation power of modern phones has improved so much that it can already perform tasks that were previously reserved for desktop computers. Fig 1.1 also shows how the display revolutionized mobile phones. One only needs to look at how the size of displays in mobile phones increased over the years. Initially, displays only occupied a very small area of the phone. Now, almost all area in the front face of the mobile phone is dedicated to displays. Furthermore, displays were previously limited as media to just see and consume content. Apple popularized the use of touchscreen displays with their introduction of the iPhone. Displays have therefore become an interface for users to interact with machine and no longer limited as a terminal that only shows content. In the future, there will be a growing demand for hyper-connective, portable, and ubiquitous devices. Displays and its related electronics will once again play an important role in these next-generation devices.

Fig 1.1 Evolution of mobile phones from 1980's to present. (Images from Google Images)

1.2 Thin-Film Transistor

1.2.1 Overview of TFT

The first inception of thin-film transistors (TFT) have been credited to either J.E

Lilienfield with his patents on MESFET [1] and MISFET [2] devices in 1930 and 1933, respectively, or O. Heil [3] with his patent in 1935. However, these patents did not contain transfer curves or data of actual devices. Lilienfield even incorrectly posited that the channel should have higher conductivity than the substrate/gate [4]. Still, these patents presented the idea that current can be controlled or influenced in a material by a transverse electric field due to voltage application. It would take a few more years before the first operational TFT was demonstrated by Weimer in 1962 [5]. Weimer was able to obtain good electrical characteristics by first depositing gold electrodes as source and drain on a glass substrate, then, depositing Cadmium Sulfide (CdS) between the electrodes and finally, placing an insulator on the CdS prior to the deposition of the gate. TFTs would not have many significant applications until the application of Cadmium Selenide (CdSe) TFTs to drive individual pixels in an active matrix [6]. This idea of using TFTs to drive the LCD was first proposed by Lechner in 1971 [7] and Brody's work was the first demonstration of an active matrix liquid crystal display (AM-LCD) [6]. Brody and his colleagues would then extend this active matrix design to an electroluminescent display panel [8].

By then, TFTs were becoming useful in several applications, but performance of CdS and CdSe were not yet impressive. During this time, researchers such as Spear and LeComber have discovered that *a*-Si can be doped to enable p-type and n-type behavior [9, 10]. This discovery is crucial to the eventual development of hydrogenated *a*-Si (*a*-Si:H) TFTs which was achieved by decomposing silane in a glow discharge [11]. Ever since then, *a*-Si has become the dominant channel material in TFT, with most large-area displays opting for *a*-Si because of its uniformity and ease of process. The performance of *a*-Si is sufficient for previous displays since the main requirement then was that the

transistor was able to merely switch, how fast it switched was not yet very important. However for high resolution and Organic Light-Emitting Diode (OLED) displays, which need a higher frequency and current, the electrical characteristics of *a*-Si is not sufficient.

Other channel materials have also been proposed. For instance, the performance of *a*-Si can be radically improved by Excimer Laser Annealing (ELA) [12-15], metal-induced lateral crystallization [16], or solid phase crystallization [17] to form poly-Si. The resulting poly-Si TFTs have very high mobilities ranging from 150 – 400 cm^2/Vs. However, application of poly-Si is limited to smaller form factors since being polycrystalline, its grain size uniformity becomes worse as the area increases.

Organic semiconductors were first applied as channel materials in TFTs during the 1980's [18-20]. Even though the mobilities then were very low, in the order of 10^{-5} cm^2/Vs, these results demonstrated the large potential of organic semiconductors in device applications. Organic TFTs with mobility greater than 1 cm^2/Vs which is comparable to *a*-Si:H TFTs were finally achieved in 1997 by using Pentacene [21]. The performance of organic TFTs has since improved further that they are being widely used in flexible organic transistors and complementary circuits [22-24]. Despite these advancements, it would still be difficult to integrate organic semiconductors in applications that require high performance such as in next generation high resolution displays.

1.2.2 Oxide TFT

Oxide TFTs have been proposed as channel materials in thin-film transistors as early as 1964 with SnO_2 TFTs [25] and in 1968 with Li-doped ZnO TFTs [26]. However, the performance of these proposed TFTs were not yet very good. Nevertheless, these

materials demonstrated that transparent semiconductors can be utilized as channel materials in TFTs. The idea of wide band gap oxide semiconductors with high electron mobilities were primarily introduced by Hosono in his two papers in 1996 [27, 28]. In these papers, he presented the idea that novel oxide amorphous semiconductors having an electronic configuration of $(n-1)d^{10}s^0$ with $n \geq 4$ will have high electron mobility [27, 28]. In 2003, Nomura and co-workers reported single crystalline InGaZnO (sc-IGZO) with a very high mobility of ~80 cm^2/Vs and on/off current ratio of ~10^6 [29]. This represented the first true breakthrough in the utilization of transparent oxide semiconductors in high performance devices such as in TFTs. The biggest breakthrough, however, occurred the following year when amorphous InGaZnO (*a*-IGZO) was used as the channel material in TFTs [30]. Unlike sc-IGZO which was annealed upwards of 1400 ^oC to achieve high performance, *a*-IGZO was deposited at room temperature on a flexible substrate by pulsed laser deposition [30]. Compared with other channel materials, the electrical characteristics observed are much better compared to both *a*-Si and organic semiconductors and competitive with poly-Si. In large area applications, *a*-IGZO becomes much superior to poly-Si because of its better large area uniformity. Table 1.I is a comparison of different channel materials for TFTs. As seen from the table, *a*-IGZO has advantage in mobility in all channel materials except poly-Si. The on/off ratio of *a*-IGZO is superior to all other channel materials with the off current even reaching in the order of 10^{-14}. This high on/off ratio and very low off current makes *a*-IGZO attractive in applications that require low power and battery consumptions such as in smartphones and tablets. The fact that *a*-IGZO can be deposited at room temperature (RT) over a large area like organic semiconductors while having better electrical characteristics makes it very attractive in high performance large area displays. Printability of *a*-IGZO is also possible,

although a higher temperature than RT is needed to complete the film formation process. Industrial integration is also easier for *a*-IGZO since it can have a device structure similar with *a*-Si:H by just replacing the *a*-Si channel with *a*-IGZO. The biggest issues with *a*-IGZO channel materials are: first, its instability especially to ambient effects and light, although it is still more stable compared to *a*-Si; second, CMOS is very difficult to achieve in *a*-IGZO because of its very strong n-type characteristics. To achieve CMOS technology in *a*-IGZO, organic transistors or carbon nanotubes [31] can be used as complementary p-type transistors because of their very strong p-type characteristics. Other p-type oxide semiconductors such as SnO_x [32] and Cu_xO [33, 34] can also be used.

Table 1.I Comparison of different channel materials for TFTs.

	organic	***a*-Si:H**	**Poly-Si**	***a*-IGZO**
Mobility (μ, cm^2/Vs)	< 2	< 1	> 100	~10 - 40
On/off ratio	$< 10^8$	$< 10^6$	$< 10^7$	$> 10^8$
Uniformity	Very good	Excellent	Poor	Very good
Process T	RT – 200 ºC	150 – 350 ºC	250 – 500 ºC	RT – 400 ºC
Bias stress stability	Poor	Poor	Good	> *a*-Si
Light stability	Poor	Poor	Good	> *a*-Si
OLED pixel circuit	Complex	Complex	Complex	Simple
Polarity	CMOS (PMOS > NMOS)	NMOS	CMOS	NMOS
Printable	Yes	No	Yes (ELA)	Yes (150 – 400ºC)
Process cost	Low	Very low	Very High	Low – Average
Industrial applications	Difficult to Integrate	Fully Integrated	Fully Integrated	Emerging

a-IGZO is not the only oxide semiconductor that is attracting wide attention. Polycrystalline oxide semiconductors such as ZnO [35-38] have also been researched as TFT channel material. ZnO has attracted much attention because it is transparent and can also be fabricated at room temperature. However, it is very difficult to form amorphous

ZnO films and they require a high voltage to turn on [38]. Other amorphous oxide semiconductors have also been employed such as *a*-InZnO [39-43], *a*-ZnSnO [44, 45], *a*-InSnZnO [46-49], and more recently amorphous-like ZnON [50, 51]. Table 1.II compares the structure, electrical properties, and stability of the different oxide semiconductors. Oxide semiconductors usually have comparable electrical properties with each other. The advantage of *a*-IGZO is that *S* is usually low and on/off current ratio is often superior compared to other oxide semiconductors. Optimized *a*-InSnZnO TFTs usually have better electrical properties but their stability is inferior to *a*-IGZO. Oxide semiconductors such as *a*-ZnSnO and *a*-InSnZnO were developed to lower the dependence on expensive and rare In or Ga. ZnON have very good electrical characteristics and better light stability compared to other oxide semiconductors due to a narrower band gap with the addition of N. However, because of the narrower band gap, ZnON is not transparent.

Table 1.II Comparison of different oxide channel materials for TFTs.

	InZnO	**ZnO**	**InSnZnO**	**ZnON**	***a*-IGZO**
Structure	Amorphous	Polycrystalline	Amorphous	Amorphous-like	Amorphous
Mobility (μ, cm^2/Vs)	~5 – 30	~5 – 20	> 20	> 40	~10 - 40
On/off ratio	< 10^8	10^5 – 10^{10}	>10^8	~ 10^8	> 10^8
Subthreshold swing (*S*, V/dec)	~ 0.3 – 0.8	~ 0.2 – 1	~ 0.2 – 0.4	0.8 – 1	0.1 – 0.2
Process T	~300 ^{o}C	200 – 300 ^{o}C	~300 ^{o}C	250 – 350 ^{o}C	RT – 400 ^{o}C
Bias stress stability	Poor	Poor	Poor	Poor	> other oxides
Light stability	Poor	Poor	Poor	Good	Poor

1.2.3 Material properties of *a*-IGZO TFTs

The emergence of oxide semiconductors such as *a*-IGZO as the channel material in

next generation displays is due to their impressive properties. For an amorphous material, *a*-IGZO has superb electrical properties. The room temperature processability and wide band gap ensure that *a*-IGZO will have applications in flexible and transparent applications [52, 53]. The development of printing and low temperature technologies will also enable *a*-IGZO applications in more advanced settings like in wearable and ubiquitous applications. Studying *a*-IGZO in more detail especially the degradation mechanisms is very important since it is expected that transparent displays will have a huge market in the next few decades. Fig 1.2 shows the growth projection of transparent displays in comparison with flat panel displays [54]. The flat panel display market will eventually saturate and is expected to slightly decrease in the coming years. However, the market for transparent displays is projected to become an emerging market and eventually supplant flat panel displays.

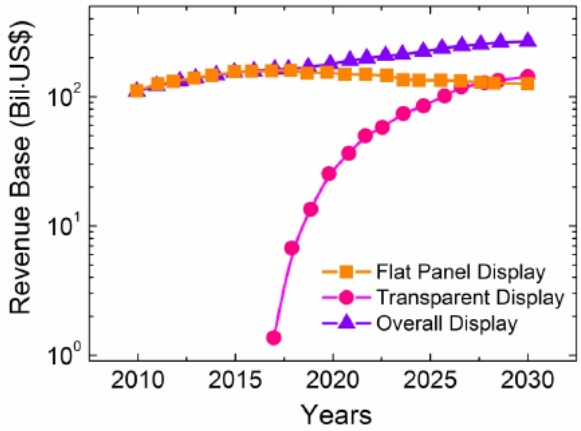

Fig 1.2 Projection of the growth of the overall display, flat panel, and transparent display market in the next decades (from [54]).

Figure 1.3 shows the comparison in the manufacturing capacity growth between oxide and Low temperature poly-Si (LTPS) [55]. Currently, the manufacturing capacity

of oxide TFT lags behind LTPS. However, it is expected that as the research and development and manufacturing technologies of oxide TFTs mature, its manufacturing capacity will further grow. This bodes well with the situation that is projected in Fig 1.4 [56]. It is expected that by 2016, OLED TVs will outship 4K (Liquid Crystal Display) LCD TV. The moniker 4k means that these displays will have a resolution of 4096 x 2160 pixels. At such very high resolutions, a channel material that has high mobility, low power consumption, and more compact and smaller size is needed. Oxide semiconductors such as *a*-IGZO can achieve these requirements. Furthermore, for OLED TVs, *a*-IGZO is much more attractive than other channel materials since only a simple circuit, 2 Transistor + 1 Capacitor circuit (2T +1C), is needed for its integration to an OLED circuit [53]. Other channel materials require additional circuit elements to compensate for the instability of *a*-Si, poly-Si, or organic TFTs. These compensation circuits are needed since a slight change in the electrical characteristics of the TFT will lead to uneven brightness and the *mura* effect [53, 57, 58]. OLED also require very good electrical properties such as good mobility since the brightness of the OLED will depend on the current. Channel materials such as *a*-Si:H and organic semiconductors do not have the minimum mobility or produce a high enough current to drive these OLED displays. On the other hand, poly-Si may have a high mobility but it cannot be applied to large OLED TVs since its non-uniformity necessitates a lot of additional circuits to compensate for the non-uniformity.

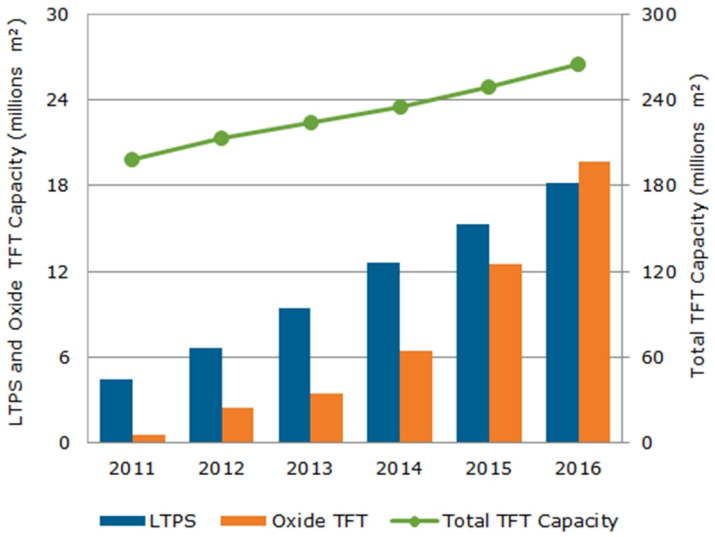

Fig 1.3 Comparison of LTPS and Oxide TFT manufacturing capacity (from [55])

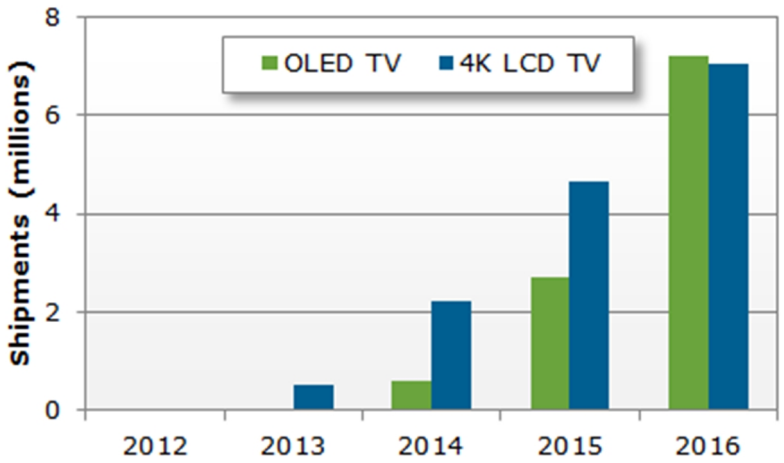

Fig 1.4 Comparison of projected shipments between OLED TV and 4K LCD TV (from [56])

OLED and LCD TVs are not the only display categories where oxide semiconductors such as *a*-IGZO can be applied. Quantum dot displays is another emerging display technology where oxide semiconductors will be used. Oxide semiconductor TFTs as the driver of quantum displays have been demonstrated [59]. This is made possible because of the constant current behavior observed in amorphous oxide semiconductors. This constant current behavior can be further improved if the oxide TFT

adopts a Corbino structure; so that *W/L* ratio is not changed after pinch-off leading to a more uniform current [60]. Fig 1.5 predicts how there will be steady increase in Quantum Dot Technology penetration in different platforms [61]. Because OLED, 4K LCD TV, and Quantum Dot Technology are expected to grow, the role of oxide semiconductors such as *a*-IGZO in these technologies is also projected to expand. It is therefore necessary to investigate and analyze the different issues in *a*-IGZO.

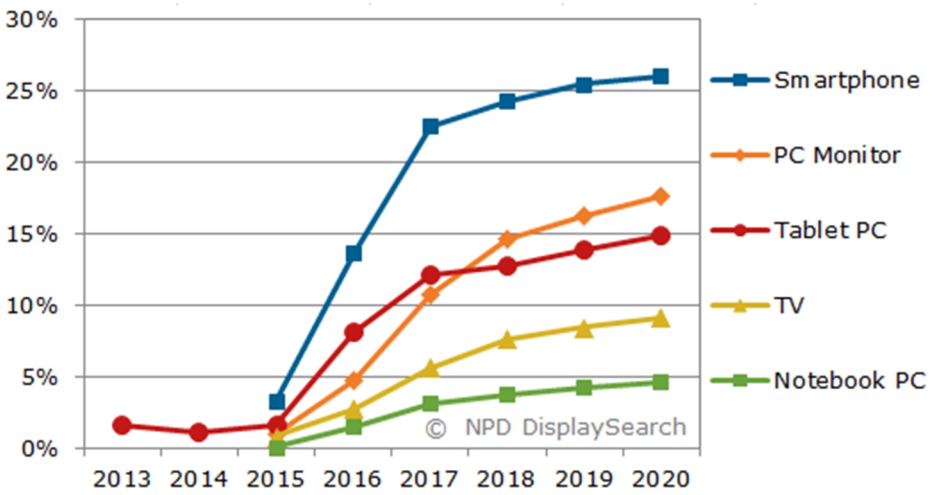

Fig 1.5 Quantum Dot Technology penetration in different applications/form factors (from [61])

1.3 *a*-IGZO beyond TFTs and other advanced applications

Application of oxide semiconductors in flexible AMOLED displays have been demonstrated by many researchers [62-66]. Figs 1.6(a-c) show just some of the flexible AMOLED displays driven by *a*-IGZO TFTs that have been presented [64-66]. The low temperature processability of *a*-IGZO and the refinement of many debonding techniques contributed to the fabrication of these flexible displays. Ever since then, Sharp, Samsung, Apple, AUO, and other display companies have used *a*-IGZO for high resolution

large-area displays.

Fig 1.6 Flexible AMOLED displays driven by a-IGZO TFTs; a) 10.2 in WUXGA (1920 x 1200) flexible AMOLED panel [64]; b) 6.5 in flexible AMOLED panel [65]; c) 11.7 in qHD (960 x 540) flexible AMOLED display [66].

Nevertheless, the application of *a*-IGZO is not limited to being the channel material of TFTs in next-generation displays. The sensitivity of *a*-IGZO to light can be exploited to develop devices such as light irradiation history sensor [67] and in photosensor arrays [68] for future input/interface applications. Applications in temperature sensors [69], radio frequency identification (RFID) [70, 71] and near field communications (NFC) [72] technologies are also possible. Circuit integration of *a*-IGZO is another promising application where *a*-IGZO can excel in [31, 73]. Integrating *a*-IGZO in circuits will enable the development of high performance, transparent, and flexible electronics that cannot be achieved using other opaque semiconductor materials. Touch panel applications is also possible because of the low off-current and low noise of *a*-IGZO during the off/pause period [74]. Fig 1.7 shows device images of some of the advanced *a*-IGZO applications that were mentioned above. Other promising device application of *a*-IGZO is in memory devices [75-78]. By varying the oxygen vacancy (V_O) concentration the resistivity/conductivity of the *a*-IGZO can be varied, thus, resistive switching can be achieved.

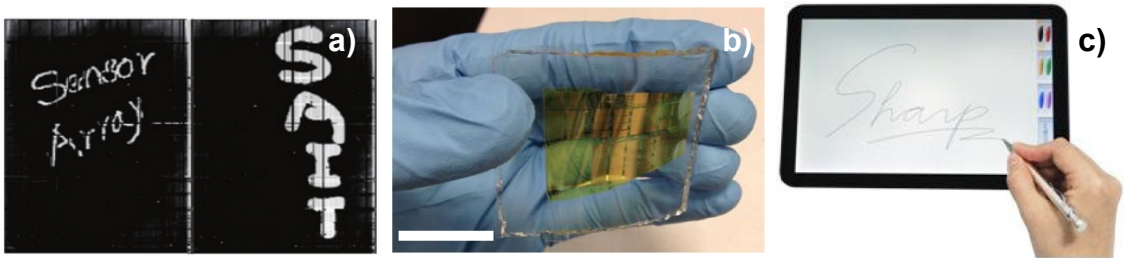

Fig 1.7 Advanced device application of *a*-IGZO; a) photosensor array [68]; b) transparent flexible circuit (ring oscillator) using hybrid CNT/IGZO transistors [31]; c) 10.1 in high performance *a*-IGZO touch panel display [74].

1.4 Stability issues of oxide TFTs

1.4.1 The gate insulator and its interface

A major issue in *a*-IGZO is its instability to bias stress, ambient effects and illumination. This instability is much worse for unannealed and unpassivated *a*-IGZO TFTs. There are three major sites where degradation may take place and these sites are also common sources or causes of degradation: first, the gate insulator and its interface with the channel; second, the channel bulk itself; and third, the backchannel and its interface with the passivation.

Selecting an appropriate gate insulator is crucial for *a*-IGZO. At the minimum, it should have good surface roughness, large resistance to dielectric breakdown, and high capacitance to reduce the operation/turn-on voltage. Instability in the gate insulator and its interface occurs when the interface quality is low such that charge trap sites are created at this interface [79]. During bias stress application, either charge trapping in the gate insulator interface or charge injection occurs [80]. Usually, there is no change in the *S* value during bias stress in *a*-IGZO which suggests that degradation mechanism is due to simple charge trapping at the gate insulator. Because the charge trapping occurs near the

gate insulator, having more charge trapping sites leads to greater degradation during bias stress. Having a very high amount of hydrogen at the gate insulator has also been shown to be detrimental to the stability since these can create additional shallow hydrogen related states that act as additional charge trapping sites [79, 81, 82]. Researchers have shown that employing gate insulators with high quality interface and reduced hydrogen concentration such as in Al_2O_3 [83] and fluorinated SiN_x [84] can improve the stability of *a*-IGZO.

1.4.2 The channel bulk

The quality of the channel material is important in the stability of the TFT. Unannealed TFTs will not have good stability since the *a*-IGZO layer will have a high concentration of native donor defects [85]**.** Instability during negative bias illumination stress (NBIS) even for passivated samples demonstrates that degradation is caused by inherent defects and states in the *a*-IGZO channel itself [86]. The creation of these states is largely dependent on the V_O amount since the nature of these created states are ionized oxygen vacancy (V_O^{2+}) [86]. These additional V_O^{2+} states act as deep hole trapping centers and increase the carrier concentration by giving free carriers in *a*-IGZO. This is why the V_O is a large source of instability in *a*-IGZO especially during NBIS [86-88].

1.4.3 The backchannel and its interface

For unpassivated *a*-IGZO TFTs, the exposed backchannel is a major source of degradation since adsorbed oxygen [89] and moisture can easily adsorb on the backchannel surface [90-92]. Figs 1.8 and 1.9 illustrate how moisture and oxygen can

readily adsorb on the backchannel, respectively. When moisture adsorbs itself on the backchannel, it can act as an electron donor by increasing the electrons in the channel. In this way, the threshold voltage (V_{th}) shifts in the negative direction because an increase in carrier concentration means that a lower voltage is needed to operate the transistor. On the other hand, when oxygen adsorbs itself on the backchannel, it captures some of the electrons in the channel forming a depletion layer in that region. Because of the reduced carrier concentration, the V_{th} shifts positively since a higher amount of voltage is now needed to modulate the transistor. Adsorbed oxygen also contributes to the instability during NBIS especially for unpassivated TFT. With illumination, the previously adsorbed oxygen on the backchannel will undergo photo-desorption [93]. By doing so, the electron previously captured by the now photodesorbed oxygen will be released into the channel. This leads to a negative V_{th} shift during NBIS.

An exposed backchannel also makes *a*-IGZO susceptible to process damage. Process damage can generate additional interface trap states which can affect the uniformity and electrical characteristics of *a*-IGZO [94]. In addition, processes such as dry etching can severely damage the backchannel interface and etching residue has been shown to act as acceptor-like states in *a*-IGZO.

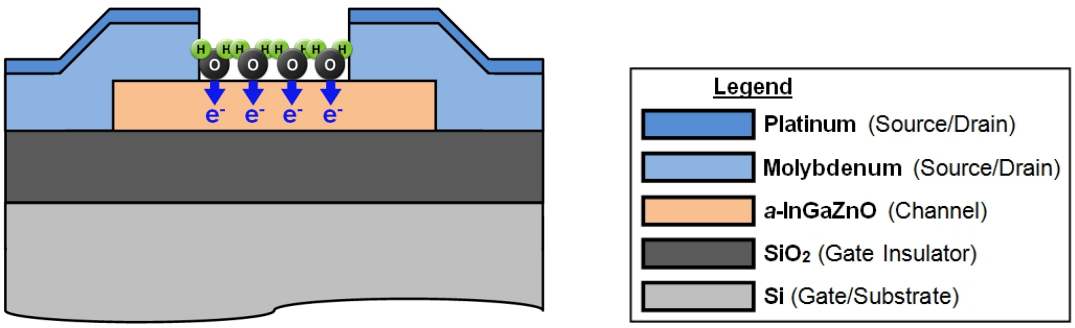

Fig 1.8 Illustration of moisture adsorption in the backchannel region of unpassivated *a*-IGZO TFTs demonstrating how moisture can introduce extra electrons into the channel.

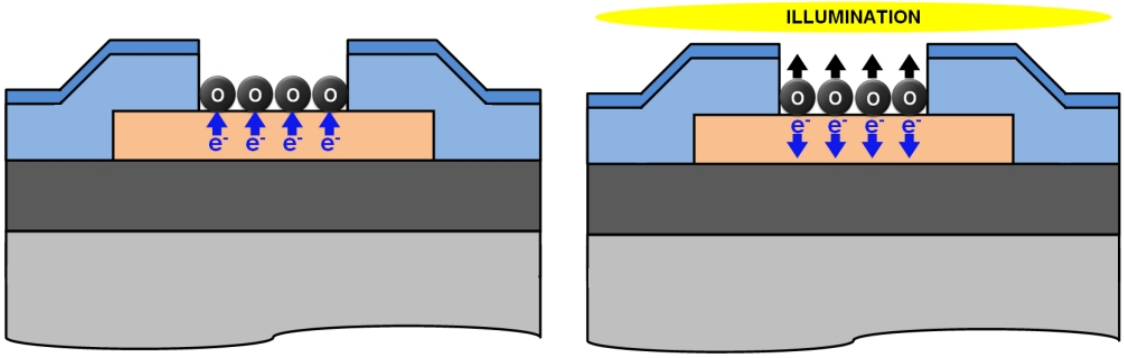

Fig 1.9 Illustration of oxygen adsorption in the backchannel region of unpassivated *a*-IGZO TFTs showing how the adsorbed oxygen captures electrons from the channel. Right figure illustrates the photo-desorption of adsorbed oxygen during illumination which causes the release of initially captured electrons into the channel.

1.5 Objectives and outline of the thesis

As discussed in the previous section, for *a*-IGZO to be successful in many applications, its stability issues need to be addressed. Furthermore, to enable application of *a*-IGZO in any substrate, a more effective low temperature annealing process should be developed and analyzed. The objectives of this thesis are three-fold:

1. *Develop a highly reliable organic-inorganic hybrid passivation layer that can be fabricated using solution process.*

An effective passivation layer is mandatory in *a*-IGZO TFTs. Developing and utilizing a passivation layer that can be fabricated by solution process is very important in future low-cost flexible applications of *a*-IGZO. Usually, there are tradeoffs when a material is fabricated by solution process. For instance, the performance of solution-processable materials like organic materials may be inferior to conventional materials. Therefore, a passivation layer that can overcome these tradeoffs will be very attractive.

2. *Understand the different degradation and reliability improvement mechanisms related to common elements incorporated into a-IGZO during fabrication.*

During fabrication of *a*-IGZO, elements such as H and C in varying degrees are incorporated into *a*-IGZO. Elements such as F are also added into materials to modify their characteristics. Understanding the role of these elements and especially how they affect the characteristics and reliability of *a*-IGZO is important if highly reliable *a*-IGZO TFTs are to be developed.

3. *Develop a low temperature annealing for already-passivated a-IGZO TFTs.*

Not all flexible substrate can withstand the high temperature annealing of up to 400 ^{o}C that is typically applied to *a*-IGZO TFTs to improve its stability and electrical characteristics. Polyimide has been commonly used as flexible substrate since it can endure temperatures of up to ~300 ^{o}C. However, to use other flexible materials such as paper, lowering the temperature at the substrate layer to even RT levels (~25 ^{o}C) is needed. Furthermore, using a low temperature process on already passivated TFTs is important. Making the low temperature annealing process the last process simplifies the fabrication flow and enables it to reverse any fabrication damage. Furthermore, as stated above, a passivation layer is mandatory for *a*-IGZO TFTs. Therefore, demonstrating that a low temperature annealing process is compatible with passivated *a*-IGZO TFTs is necessary.

Achieving these objectives will greatly aid in the development of transparent, printed, and flexible applications for *a*-IGZO.

In this thesis, the first few chapters deals with the stability issues of *a*-IGZO and how it can be addressed with the utilization of an excellent passivation layer. In chapter 2, a comparison between conventional inorganic passivation and emerging solution processed organic passivation layers is presented. Bias and humidity stress is performed on *a*-IGZO TFTs passivated with an organic-inorganic hybrid passivation material based on polysilsesquioxane (PSQ) fabricated by solution process. Performance of the non-photosensitive PSQ (NP-PSQ) passivation is compared with unpassivated *a*-IGZO TFTs. Secondary Ion Mass Spectrometry (SIMS) and X-ray Photoelectron Spectroscopy (XPS) are performed to aid in the analysis of the degradation and reliability improvement mechanism. SIMS and XPS analysis were crucial in understanding the role of H and C in *a*-IGZO.

Chapter 3 starts with the discussion and analysis on how process and etching damage can affect the properties of *a*-IGZO. A new class of PSQ passivation layers is introduced which is the photosensitive PSQ (P-PSQ) passivation layer designed to no longer need any dry etching. Bias and humidity stress results of P-PSQ are compared with unpassivated TFT, and NP-PSQ passivated TFTs. Together with the SIMS analysis and the reliability tests, the stability improvement mechanisms are examined and the role of F in improving the stability and properties of *a*-IGZO are discussed.

The latter part of the thesis focuses on the efforts to lower the annealing temperature especially at the substrate layer. The start of chapter 4 gives an overview of the different conventional annealing and low temperature annealing methods performed on *a*-IGZO. Two types of excimer laser annealing (ELA): XeCl ELA and KrF ELA are introduced and their effects on *a*-IGZO are studied. 2D heat transfer simulation was performed by COMSOL Multiphysics simulation to analyze the temperature induced by the laser at

different interfaces. This simulation also helps determine if the temperature induced at the substrate layer is low. XPS, SIMS, X-ray Diffraction (XRD) and X-ray Reflectometry (XRR) analysis are performed to investigate the effect of ELA on the elemental composition, chemical bonding, and structure of *a*-IGZO.

The results and conclusion of the thesis are summarized in chapter 5. Future outlook and suggestions for further developments are also given in this chapter. The results and analysis in this thesis are important especially in developing highly reliable, printed, transparent, and flexible *a*-IGZO devices.

References

[1] J. E. Lilienfield, U.S. Patent (1930) 1745175.

[2] J. E. Lilienfield, U.S. Patent (1933) 1900018.

[3] O. Heil, Brit. Patent (1935) BP439457.

[4] W. E. Howard, Thin-Film Transistors ed. C. R. Kagan and P. Andry, (2003) 1.

[5] P. K. Weimer, Proc. of the Inst. of Radio Eng. **50**, (1962) 1462.

[6] T. P. Brody, J. A. Asars, G. D. Dixon, IEEE Transact. on Elect. Dev., **20**, (1973) 995.

[7] B. J. Lechner, F. J. Marlowe, E. O. Nester, and J. Tults, Proc. IEEE, **59**, (1971) 1566.

[8] T. P. Brody, C. L. Fang, Z. P. Szepesi, D. H. Davies, IEEE Transact. on Elect. Dev., **22**, (1975) 739.

[9] W. E. Spear, P. G. Le Comber, Solid State Commun., **17**, (1975) , 1193.

[10] W. E. Spear, P. G. Le Comber, Philos. Mag., **33** (1976) 935.

[11] P. G. LeComber, W. E. Spear, and A. Ghaith, Electron. Lett., **15**, (1979) 179.

[12] T. Sameshima, S. Usui, and M. Sekiya, IEEE Elect. Dev. Lett., **7,** (1986) 276.

[13] T. Serikawa, S. Shirai, A. Okamoto, and S. Suyama, IEEE Transact. on Elect. Dev., **36**, (1989) 1929.

[14] K. Shimizu, O. Sugiura, and M. Matsumura, IEEE Transact. on Elect. Dev., **40**, (1993) 112.

[15] H. Kuriyama, S. Kiyama, S. Noguchi, T. Kuwahara, S. Ishida, T. Nohda, K. Sano, H. Iwata, H. Kawata, M. Osumi, S. Tsuda, S. Nakano, and Y. Kuwano Jpn. J. Appl. Phys., **30**, (1991) 3700.

[16] S.-W. Lee and S.-K. Joo, IEEE Elect. Dev. Lett., **17,** (1996) 160.

[17] T. Matsuyama, M. Tanaka, S. Tsuda, S. Nakano, and Y. Kuwano, Jpn. J. Appl. Phys. **32**, (1993) 3720.

[18] F. Ebisawa, T. Kurokawa, and S. Nara, J. Appl. Phys., **54**, (1983) 3255.

[19] K. Kudo, M. Yamashina, T. Moriizumi, Jpn. J. Appl. Phys., **23**, (1984) 130.

[20] A. Tsumura, H. Koezuka, T. Ando, Appl. Phys. Lett., **49**, (1986) 1210.

[21] Y.-Y. Lin, D. J. Gundlach, S. Nelson, T. N. Jackson, IEEE Elect. Dev. Lett., **18**, (1997) 606.

[22] H. Klauk, U. Zschieschang, J. Pflaum, and M. Halik, Nature, **445**, (2007) 745.

[23] T. Sekitani, U. Zschieschang, H. Klauk, and T. Someya, Nature Mater., **9**, (2010) 1015.

[24] K. Fukuda, Y. Takeda, M. Mizukami, D. Kumaki, and S. Tokito, Sci. Rep., **4**, (2014) 3947.

[25] H. A. Klasens, H. Koelmans, Solid-State Electron. **7**, (1964) 701.

[26] G. F. Boesen, J. E. Jacobs , Proc. of the Inst. of Elect. and Elect. Eng., **56**, (1968) 2094.

[27] H. Hosono, N. Kikuchi, N. Ueda, and H. Kawazoe, J. Non-Cryst. Sol., **198-200**, (1996) 165.

[28] H. Hosono, M. Yasukawa, H. Kawazoe, J. Non-Cryst. Sol., **203,** (1996) 334.

[29] K. Nomura, H. Ohta, K. Ueda, T. Kamiya, M. Hirano, H. Hosono, Science, **300**, (2003) 1269.

[30] K. Nomura, H. Ohta, A. Takagi, T. Kamiya, M. Hirano, and H. Hosono, Nature, **432**, 488 (2004).

[31] H. Chen, Y. Cao, J. Zhang, and C. Zhou, Nature Commun., **5**, (2014), 4097.

[32] E. Fortunato, R. Martins, Phys. Stat. Sol. Rapid Res. Lett., **5**, 2011 336 .

[33] Z. Q. Yao, S. L. Liu, L. Zhang, B. He, A. Kumar, X. Jiang, W. J. Zhang, and G. Shao, Appl. Phys. Lett. **101**, (2012) 042114.

[34] E. Fortunato, V. Figueiredo, P. Barquinha, E. Elamurugu, R. Barros, G. Goncalves, S. H. K. Park, C. S. Hwang, R. Martins, Appl. Phys. Lett., **96**, (2010) 192102.

[35] R. L. Hoffman, B. J. Norris, and J. F. Wager, Appl. Phys. Lett., **82**, (2003) 735.

[36] S. Masuda, K. Kitamura, Y. Okumura, S. Miyatake, H. Tabata, and T. Kawai, J. Appl. Phys., **93**, (2003) 1624.

[37] P. F. Carcia, R. S. McLean, M. H. Reilly, and G. Nunes, Appl. Phys. Lett., **82**, (2003) 1119.

[38] E. M. C. Fortunato, P. M. C. Barquinha, A. C. M. B. G. Pimentel, A. M. F. Goncalves, A. J. S. Marques, L. M. N. Pereira, and R. F. P. Martins, Adv. Mater., **17**, (2005) 590.

[39] N. L. Dehuff, E. S. Kettenring, D. Hong, H. Q. Chiang, J. F. Wager, R. L. Hoffman, C. H. Park, and D. A. Keszler, J. Appl. Phys., **97**, (2005) 064505.

[40] B. Yaglioglu, H. Y. Yeom, R. Beresford, and D. C. Paine, Appl. Phys. Lett., **89**, (2006) 062103.

[41] J. I. Song, J. S. Park, H. Kim, Y. W. Heo, J. H. Lee, J. J. Kim, G. M. Kim, and B. D. Choi, Appl. Phys. Lett., **90**, (2007) 022106.

[42] E. Fortunato, P. Barquinha, A. Pimentel, L. Pereira, G. Goncalves, and R. Martins, Phys. Stat. Solidi Rapid Res. Lett., **1**, (2007) R34.

[43] A. J. Leenheer, J. D. Perkins, M. F. A. M. van Hest, J. J. Berry, R. P. O'Hayre, and D. S. Ginley, Phys. Rev. B, **77**, (2008) 115215.

[44] H. Q. Chiang, J. F. Wager, R. L. Hoffman, J. Jeong, and D. A. Keszler, Appl. Phys. Lett., **86**, (2005) 013503.

[45] P. Gorrn, P. Holzer, T. Riedl, W. Kowalsky, J. Wang, T. Weimann, P. Hinze, and S. Kipp, Appl. Phys. Lett., **90**, (2007) 063502.

[46] M. S. Grover, P. A. Hersh, H. Q. Chiang, E. S. Kettenring, J. F. Wager, and D. A. Keszler, J. Phys. D: Appl. Phys., **40**, (2007) 1335.

[47] S. Tomai , M. Nishimura , M. Itose , M. Matsuura , M. Kasami , S. Matsuzaki , H. Kawashima , F. Utsuno , and K. Yano , Jpn. J. Appl. Phys. Part 1 **51**, (2012) 03CB01.

[48] S. Urakawa, S. Tomai, Y. Ueoka, H. Yamazaki, M. Kasami, K. Yano, D. Wang, M. Furuta, M. Horita, Y. Ishikawa, and Y. Uraoka, Appl. Phys. Lett. **102**, (2013) 053506.

[49] J. H. Song, K. S. Kim, Y. G. Mo, R. Choi, and J. K. Jeong, IEEE Elect. Dev. Lett. **35**, (2014) 853.

[50] Y. Ye, R. Lim and J. M. White, J. Appl. Phys., **106**, (2009) 074512.

[51] H.-S. Kim, S. H. Jeon, J. S. Park, T. S. Kim, K. S. Son, J.-B. Seon, S.-J. Seo, S.-J. Kim, E. Lee, J. G. Chung, H. Lee, S. Han, M. Ryu, S. Y. Lee, and K. Kim, Sci. Rep. **3** (2013) 1459.

[52] E. Fortunato, P. Barquinha, and R. Martins, Adv. Mater., **24**, (2012) 2945.

[53] T. Kamiya, K. Nomura, and H. Hosono, Sci. Technol. Adv. Mater., **11**, (2010) 044305.

[54] Displaybank, Transparent Display Technolology and Market Forecast (2011).

[55] NPD DisplaySearch, TFT LCD Process Roadmap Report (2013).

[56] NPD DisplaySearch, Quarterly Advanced Global TV Shipment and Forecast Report (2013).

[57] SEMI, "Definition of Measurement Index (Semu) for Luminance Mura in FPD Image Quality Inspection," SEMI (2002) D31-1102.

[58] Y. Mori, K. Tanahashi, and S. Tsuji, Opt. Eng., **43**, (2004) 2696.

[59] T.-H. Kim, K.-S. Cho, E. K. Lee, S. J. Lee, J. Chae, J. W. Kim, D. H. Kim, J.-Y. Kwon, G. Amaratunga, S. Y. Lee, B. L. Choi, Y. Kuk, J. M. Kim & K. Kim, Nature

Photonics, **5**, (2011) 176.

[60] M. Mativenga, S. H. Ha, D. Geng, D. H. Kang, R. K. Mruthyunjaya, G. N. Heiler, T. J. Tredwell, and Jin Jang, IEEE Transact. Elect. Dev., **61**, (2014) 3199.

[61] NPD DisplaySearch, Quantum Dot Technology and Market Forecast Report (2014).

[62] M.-C. Sung, H.-N. Lee, C. N. Kim, S. K. Kang, D. Y. Kim, S.-J. Kim, S. K. Kim, S.-K. Kim, H.-G. Kim, and S.-T. Kim, Proc. 7th Int. Meeting Information Display, (2007) 9–1.

[63] S. Nakano, N. Saito, K. Miura, T. Sakano, T. Ueda, K. Sugi, H. Yamaguchi, I. Amemiya, M. Hiramatsu, and A. Ishida, J. Soc. Inf. Disp. **20**, (2012) 493.

[64] N. Saito, T. Ueda, K. Miura, S. Nakano, T. Sakano, Y. Maeda, H. Yamaguchi, and I. Amemiya, SID Symp. Dig. of Tech. Papers, **44**, (2013) 443.

[65] J.-S. Park, T.-W. Kim, D. Stryakhilev, J.-S. Lee, S.-G. An, Y.-S. Pyo, D.-B. Lee, Y. G. Mo, D.-U. Jin, and H. K. Chung, Appl. Phys. Lett., **95**, (2009) 013503.

[66] H. Yamaguchi, T. Ueda, K. Miura, N. Saito, S. Nakano, T. Sakano, K. Sugi, I. Amemiya, M. Hiramatsu, and A. Ishida, SID Symp. Dig. Tech. Papers **43**, (2012) 1002.

[67] M. Kimura, T. Hasegawa, K. Ide, K. Nomura, T. Kamiya, and H. Hosono, IEEE Elect. Dev. Lett., **33**, (2012), 384.

[68] S. Jeon, S.-E. Ahn, I. Song, C. J. Kim, U.-I. Chung, E. Lee, I. Yoo, A. Nathan, S. Lee, K. Ghaffarzadeh, J. Robertson, and K. Kim, Nature Mater., **11**, (2012) 301.

[69] H. Jeong, C. S. Kong, S. W. Chang, K. S. Park, S. G. Lee, Y. M. Ha, and J. Jang, IEEE Electron Device Lett., **34**, (2013) 1569.

[70] H. Ozaki, T. Kawamura, H. Wakana, T. Yamazoe, and H. Uchiyama, IEICE Electron. Exp. **8**, (2011) 225.

[71] A. Chasin, V. Volskiy, M. Libois, K. Myny, M. Nag, M. Rockele, G.A.E.

Vandenbosch, J. Genoe, G. Gielen, and P. Heremans, IEEE Transact. on Elect. Dev., **9**, (2014) 3289.

[72] K. Myny, B. Cobb, J.-L. van der Steen, A. K. Tripathi, J. Genoe, G. Gelinck, and P. Heremans, Proc. IEEE Solid State Circuits Conference, (2015) 1.

[73] M. Nag, A. Bhoolokam, S. Smout, M. Willegems, R. Muller, K. Myny, S. Schols, M. Ameys, J. Genoe, T. H. Ke, P. Vicca, T. Ellis, B. Cobb, A. Kumar, J. P. J. van der Steen, G. Gelinck, Y. Fukui, K. Obata, G. Groeseneken, P. Heremans, and S. Steudel, (2015), J. Soc. Inf. Disp.

[74] Y. Kataoka, H. Imai, Y. Nakata, T. Daitoh, T. Matsuo, N. Kimura, T. Nakano, Y. Mizuno, T. Oketani, M. Takahashi, M. Tsubuku, H. Miyake, T. Ishitani, Y. Hirakata, J. Koyama, S. Yamazaki, J. Koezuka, and K. Okazaki, SID Symp. Dig. Tech. Paper, **44**, (2013) 771.

[75] M. S. Kim, Y. H. Hwang, S. Kim, Z. Guo, D. I. Moon, J. M. Choi, M. L. Seol, B. S. Bae, and Y. K. Choi, Appl. Phys. Lett., **101**, (2012) 243503.

[76] M. C. Chen, T. C. Chang, C. T. Tsai, S. Y. Huang, S. C. Chen, C. W. Hu, S. M. Sze, and M. J. Tsai, Appl. Phys. Lett., **96**, (2010) 262110.

[77] C. H. Kim, Y. H. Jang, H. J. Hwang, C. H. Song, Y. S. Yang and J. H. Cho, Appl. Phys. Lett., **97**, (2010) 062109.

[78] K. Kado, M. Uenuma, K. Sharma, H. Yamazaki, S. Urakawa, Y. Ishikawa and Y. Uraoka, Appl. Phys. Lett. **105**, (2014) 123506.

[79] J. Lee, J.-S. Park, Y. S. Pyo, D. B. Lee, E. H. Kim, D. Stryakhilev, T. W. Kim, D. U. Jin, and Y.-G. Mo, Appl. Phys. Lett. **95**, (2009) 123502.

[80] R. B. M. Cross and M. M. De Souza, Appl. Phys. Lett., **89**, (2006) 263513.

[81] J. S. Jung, K. S. Son, K. H. Lee, J. S. Park, T. S. Kim, J. Y. Kwon, K. B. Chung, J. S.

Park, B. Koo, and S. Lee, Appl. Phys. Lett., **96**, (2010) 193506.

[82] A. Hino, S. Morita, S. Yasuno, T. Kishi, K. Hayashi, and T. Kugimiya, J. Appl. Phys., **112**, (2012) 114515.

[83] J. M. Lee, I. T. Cho, J. H. Lee, W. S. Cheong, C. S. Hwang, and H. I. Kwon, Appl. Phys. Lett., **94**, (2009) 222112.

[84] H. Yamazaki, Y. Ishikawa, M. Fujii, Y. Ueoka, M. Fujiwara, E. Takahashi, Y. Andoh, N. Maejima, H. Matsui, F. Matsui, H. Daimon, and Y. Uraoka, ECS J. Solid Stat. Sci. Technol. **3**, (2014) Q20.

[85] K. Nomura, T. Kamiya, H. Ohta, M. Hirano and H. Hosono, Appl. Phys. Lett., **93** (2008) 192107.

[86] H. Oh, S. Yoon, M. K. Ryu, C. Hwang, S. Yang, and S. K. Park, Appl. Phys. Lett., **97**, (2010) 183502.

[87] M. D. H. Chowdhury, P. Migliorato, and J. Jang, Appl. Phys. Lett., **97,** (2010) 173506.

[88] B. Ryu, H.-K. Noh, E.-A. Choi, and K. J. Chang, Appl. Phys. Lett., **97,** (2010) 022108.

[89] D. Kang, H. Lim, C. Kim, I. Song, J. Park, Y. Park and J. Chung, Appl. Phys. Lett., **90** (2007) 192101.

[90] K.-H. Lee, J. S. Jung, K. S. Son, J. S. Park, T. S. Kim, R. Choi, J. K. Jeong, J.-Y. Kwon, B. Koo, and S. Lee, Appl. Phys. Lett., **95**, (2009) 232106.

[91] J.-S. Park, J. K. Jeong, H.-J. Chung, Y.-G. Mo, and H. D. Kim, Appl. Phys. Lett., **92**, (2008) 072104.

[92] J. K. Jeong, H. W. Yang, Jong Han Jeong, Yeon-Gon Mo, and Hye Dong Kim, Appl. Phys. Lett. **93**, (2008) 123508.

[93] S. Yang, D.-H. Cho, M. K. Ryu, S.-H. K. Park, C.-S. Hwang, J. Jang, and J. K. Jeong, Appl. Phys. Lett. **96**, (2010) 213511.

[94] T.-C. Chen, T.-C. Chang, T.-Y. Hsieh, C.-T. Tsai, S.-C. Chen, C.-S. Lin, M.-C. Hung, C.-H. Tu, J.-J. Chang, and P.-L. Chen, Appl. Phys. Lett. **97**, (2010) 192103.

Chapter 2
Analysis of Non-Photosensitive Organic-Inorganic Hybrid Polysilsesquioxane Passivation Layer and its effect on *a*-IGZO.

2.1 Introduction

Subjecting TFTs to bias stress is one of the most important and effective methods to test the stability of TFTs. Furthermore, since it involves the direct current-voltage measurement of the TFT, bias stress is a simple and fast technique to check for degradation in the electrical characteristics. Degradation of most common types of thin-film transistors such as *a*-Si [1], poly-Si [2,3], and organic TFTs [4-7] after bias stress has been previously shown. The harsh effect of bias stress is also present in *a*-IGZO TFTs especially if left unpassivated [8-12]. Passivated *a*-IGZO TFTs tend to fare better when subjected to bias stress [13]. Therefore, understanding both the degradation mechanism and the role of the passivation in inhibiting degradation is important if more stable TFTs need to be developed. Moreover, the role of many elements such as H and C which are usually introduced into *a*-IGZO during fabrication is not very clear. This chapter aims to discuss the stability of non-photosensitive polysilsesquioxane (NP-PSQ) passivated *a*-IGZO TFTs by subjecting them to different types of stress. In addition, the role of hydrogen and carbon introduced from the passivation into *a*-IGZO is discussed.

Section 2.2 presents the different passivation materials that are commonly used in *a*-IGZO. There are two common types of passivation: inorganic and organic passivation materials. The advantages and disadvantages of each type will also be discussed in this

section. A third type of passivation material: hybrid passivation materials are introduced in Section 2.3. In particular, the use of a hybrid passivation material based on polysilsesquioxane (PSQ) is demonstrated. Material properties of PSQ are identified and its effect on the *a*-IGZO is studied. Section 2.3 also presents the effect of NP-PSQ on the electrical characteristics and reliability of *a*-IGZO TFTs.

Section 2.4 details the effect of hydrogen and carbon on *a*-IGZO. Being a hybrid organic-inorganic passivation material, C and H are abundant in PSQ. Therefore, large incorporation of C and H from the passivation into the *a*-IGZO should be naturally expected. In fact, elemental analysis shows this result and thus, it is important to analyze its implications and effects on *a*-IGZO. This section presents the mechanisms on how the H and C introduced from the PSQ affected the stability of *a*-IGZO.

2.2 Passivation layers

2.2.1 Inorganic passivation layers

Sensitivity of the *a*-IGZO backchannel to several ambient effects is well documented [9-12]. Depositing a passivation layer or an encapsulation is the natural recourse to protect the backchannel. Inorganic passivation layers such as SiO_x [12, 14-18], AlO_x [19-22], TiO_x [23-24], and SiN_x [25] are popular. These are popular because they are usually effective barriers in preventing many ambient effects. However, the fabrication of these passivation layers usually involve more complicated vacuum processes such as PECVD, ALD, and RF and DC Sputtering. These processes can induce some process damage that generates interface trap states [17]. This usually affects the uniformity of the electrical characteristics of multiple TFTs and can lower the quality of

the *a*-IGZO. An example of this is plasma damage incurred when depositing SiO_x or SiN_x passivation by PECVD. In addition, low deposition rate of ALD means that deposition time of thicker passivation layers will take a very long time. Furthermore, both ALD and RF sputtering have some limitations when it comes to large area applications because of their difficult deposition at this scale and size [20]. Equipment and tools used for vacuum deposition are also, in general, expensive.

2.2.2 Organic passivation layers

In most semiconductor applications, developing or adopting a technology that can fabricate materials by solution process is a big step in the technology cycle. This is because of solution process' simplicity and scalability to larger or smaller areas. Fabrication by solution process is also an additive process which implies less waste and location selective deposition. Organic passivation layers are usually fabricated by solution process or sol-gel method. Many organic passivation layers for oxide TFTs have been used such as CYTOP [26], photoacryl [12], PDMS [27], and paraffin wax [28]. Although these are fabricated by solution process or sol-gel method, their performance is usually inferior to inorganic passivation due to having large threshold voltage (V_{th}) shifts and hump effect during bias stress and in the initial transfer characteristics [12]. Therefore, it is important to develop materials that can be fabricated by solution process and at the same time possess exceptional performance.

2.3 Polysilsesquioxane passivation layer

2.3.1 Material properties

Examples of organic-inorganic hybrid passivation layers have been used in organic TFTs [29], zinc tin oxide TFTs, [30] and *a*-Si:H TFTs [31]. The merit of these hybrid passivation layers is that these take advantage of the good qualities of both inorganic and organic passivation layers. For instance, these hybrid layers are usually deposited through solution process like most organic passivation materials. However, unlike organic passivation layers, they have much better performance and reliability which rivals that of inorganic passivation layers. The edge of hybrid passivation layers over inorganic passivation is the simplicity and scalability of their fabrication.

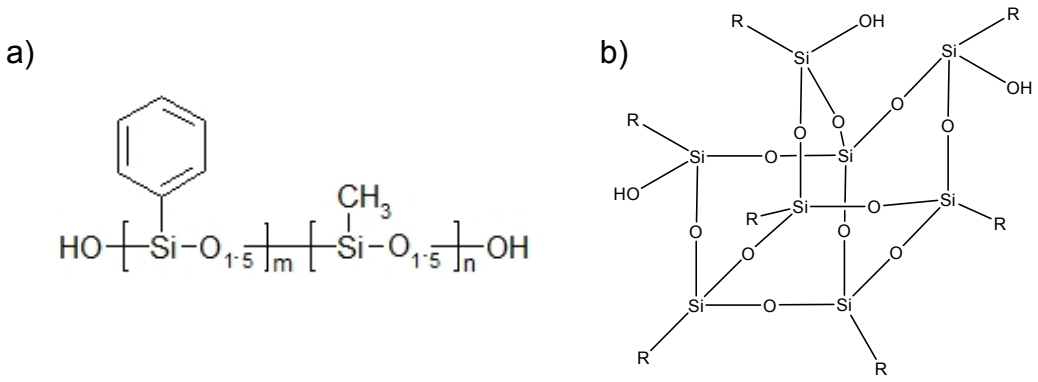

Fig. 2.1 a) PSQ structure showing Si-O backbone of PSQ with both the methyl and phenyl constituent groups and b) PSQ partial cage structure which is one of the possible configuration of PSQ after curing (adapted from [34])

Table 2.I. Summary of PSQ passivation materials used. m and n denote the mol% of the phenyl and methyl groups respectively.

Sample Name	Siloxane	Me (n)	Ph (m)
Me 100	Polymethylsilsesquioxane	100	0
Me 60/ Ph 40	Copolymer of methylsilsesquioxane and phenylsilsesquioxane	60	40

We have reported organic-inorganic hybrid passivation layers based on PSQ [32, 33]. Figure 2.1 shows the basic structure of polysilsesquioxane, while Table 2.I summarizes the differences between the two types of NP-PSQ used. Figure 2.1 illustrates the Si-O backbone (inorganic part) and the methyl and phenyl organic constituent groups of the PSQ. The two NP-PSQ variants are differentiated by the attached constituent groups. Me 100 samples were passivated by methylsilsesquioxane which only has methyl constituent groups. On the contrary, Me 60/ Ph 40 samples' PSQ passivation is a copolymer of methylsilsesquioxane and phenylsilsesquioxane with both methyl and phenyl groups (methyl/phenyl ratio of 3:2). Variation in their structures implies that these materials have differences in their properties. Methylsilsesquioxane undergoes small weight loss during pyrolysis and is chemically resistant. Although it is thermally and chemically resistant, the brittleness of methylsilsesquioxane at large thicknesses can be problematic [34]. Furthermore, initial decomposition temperature of methylsilsesquioxane is slightly lower than that of phenylsilsesquioxane [34]. On the other hand, phenylsilsesquioxane is oxidatively stable and has better mechanical properties becoming tack free at room temperature. Thermal properties are also slightly better than methylsilsesquioxane [34]. Fig 2.1b also illustrates the partial cage structure of PSQ which is just one of the possible structures that PSQ can assume. Depending on factors such as molecular mass and reaction conditions such as reaction time and temperature, PSQ can assume different structure configurations such as ladder, random, partial cage, and full cage structure [34, 35].

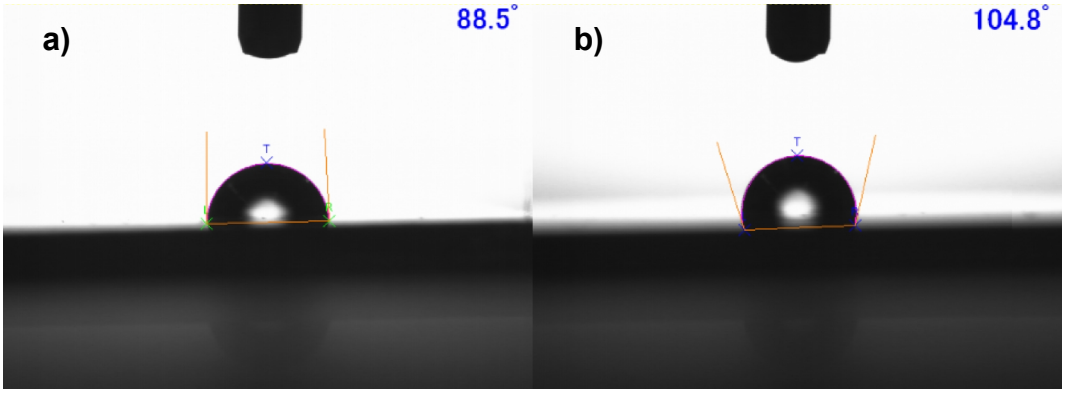

Fig. 2.2 Contact angle measurement of a 1 µL water droplet on a) Me 100 and b) Me 60/Ph 40.

Their similar structures enable them to have comparable properties. For instance, both passivation materials are hydrophobic because the phenyl and methyl constituent groups are nonpolar. Contact angle measurements also confirm the hydrophobic nature of both types of NP-PSQs. Fig. 2.2 illustrates the contact angle formed by a 1 µL water droplet on a) Me 100 and b) Me 60/ Ph 40. Using a goniometer, ten contact angle measurements were performed for each NP-PSQ type and the average is obtained. The contact angle measurements were $88.8^{o} \pm 1.0^{o}$ and $104.6^{o} \pm 0.7^{o}$ for Me 100 and Me 60/Ph40 samples, respectively. A contact angle measurement greater than or equal to 90^{o} implies hydrophobicity. The contact angle measurements show that Me 100 is barely hydrophobic while Me 60/Ph40 has greater hydrophobicity. Hydrophobicity is a very important quality especially for passivation materials. This also makes both types of NP-PSQ attractive in water-repellant applications.

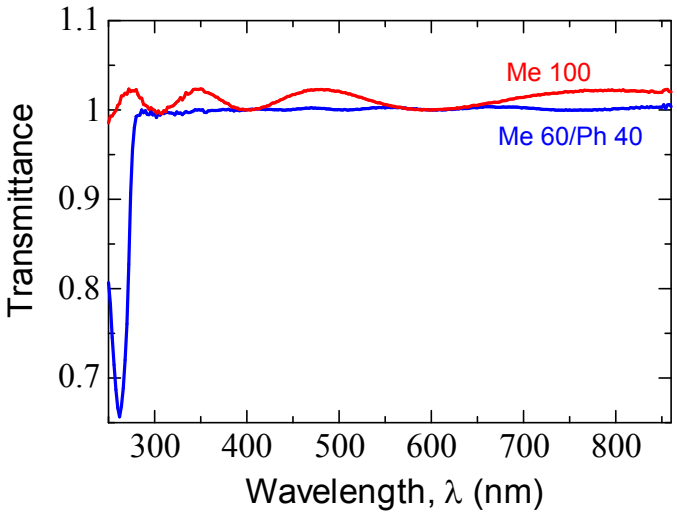

Fig. 2.3 Transmittance of Me 100 (red line) and Me 60/Ph 40 (blue line).

Aside from being hydrophobic, both materials are transparent. As seen from Fig 2.3. both types of NP-PSQ are transparent in the visible region with Me 100 having a slightly higher transmittance than Me 60/Ph 40. Note that transmittance greater than 1 means that the transmittance of the material is higher than that of the control sample (transparent glass). The spectra also show that Me 100 is even completely transparent in the UV region. This transparency makes them very attractive coating materials with *a*-IGZO which is also transparent. NP-PSQ passivation materials will have future applications in transparent integrated circuits and displays.

Copolymerization of methylsilsesquioxane and phenylsilsesquioxane is needed to combine their good properties. This is required, especially in the case of the brittle methylsilsesquioxane, to increase its toughness and prevent gelation [34, 35]. Their properties are also tunable depending on the ratio of the combination. For instance,

properties associated with methylsilsesquioxane become more pronounced as its ratio in the copolymer increases.

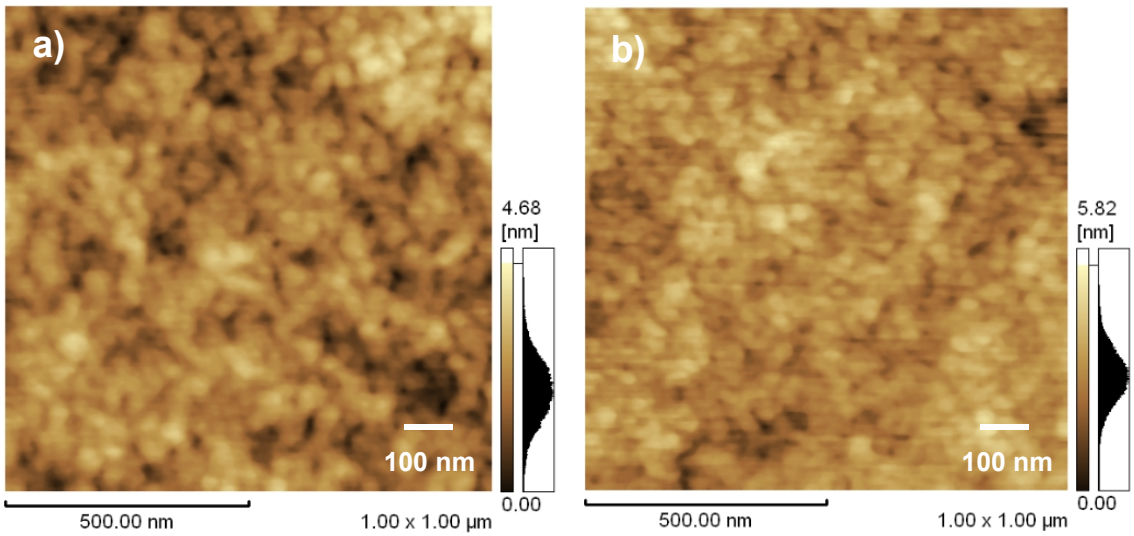

Fig. 2.4 Atomic force microscope micrograph of a) Me 100 and b) Me 60/ Ph 40 showing the surface roughness.

Atomic force microscope micrographs in Fig 2.4 shows the surface roughness and morphology of NP-PSQ passivation samples. The root mean square roughness of both Me 100 and Me 60/Ph 40 are quite good and similar with each other: 0.60 nm for Me 100 and 0.62 nm for Me 60 Ph 40. Maximum peak height of each samples, 2.17 nm for Me 100 and 2.18 nm for Me 60/Ph40 are also comparable with each other. Average surface roughness was 0.48 nm and 0.49 nm for Me 100 and Me 60 Ph 40, respectively. These surface roughness values are comparable and even better to some inorganic passivation materials such as SiO_2, Al_2O_3, Y_2O_3 and TiO_2 fabricated by vacuum process [36, 37]. These results imply that clear, transparent, and uniform films can be formed by polysilsesquioxane, thus, reducing possible pinhole defects and making them effective barriers against ambient effects.

2.3.2 Device fabrication

Heavily doped n-type Si (resistivity < 0.002 Ω·cm) with a 100 nm thermally oxidized SiO_2 was utilized as the gate and gate insulator materials, respectively. SPM cleaning was performed on the substrate prior to depositing a 70 nm thick *a*-IGZO layer by RF magnetron sputtering deposition at room temperature. Both oxygen and argon gas were used as deposition gases at an O_2/Ar ratio of 4.5%. Conventional UV photolithography and wet etching by 0.02 mol/L HCl was used to pattern and form the *a*-IGZO islands. A stack of 80 nm thick Mo and 20 nm thick Pt were deposited using RF magnetron sputtering deposition and patterned using the lift off technique. This Mo/Pt stack served as the source and drain of the TFT. A stacked structure for the electrodes is used because Mo can easily oxidize. These TFTs were annealed at a temperature of 300 ^oC for 120 min in N_2/O_2 (4:1) ambient atmosphere (AT Annealing).

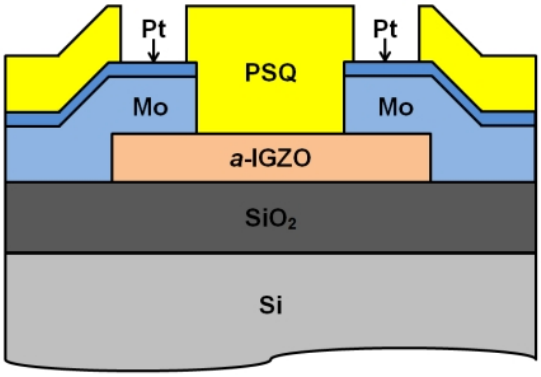

Fig. 2.5 Passivated *a*-IGZO TFT structure with contact holes.

A simple solution process was employed to coat the NP-PSQ passivation layers. The passivation was initially spin-coated on the *a*-IGZO TFT at a main spin rate of 3000 rpm for 15 s. A 2 step baking process is then performed: first, prebaking at a

temperature of 130 ^{o}C for 90 s was performed to evaporate the solvent and finally, post-baking at 300 ^{o}C for 1 hour in ambient atmosphere was done to cure the passivation material. Contact holes were formed by dry etching using inductively coupled plasma reactive ion etching (ICP-RIE) process with a $CF_4/O_2/Ar$ gas mixture. Additional post-annealing at 300 ^{o}C for 2 h under O_2 ambient atmosphere was also performed after dry etching. Depending on factors such as processing parameters and molecular weight, the passivation layer may assume several structures such as: ladder, cage, partial cage and random structure [35]. Owing to the above-mentioned factors, the partial cage structure is the most energetically favorable and most probable structure in this case. The resulting passivated *a*-IGZO TFT structure which is a bottom gate top contact structure with contact holes is shown in Fig. 2.5.

2.3.3 Electrical characteristics

The TFT electrical characteristics are usually derived from the transfer characteristics which plots the source-to-drain current (I_{ds}) against gate-to-source voltage (V_{gs}) across different drain-to-source voltages (V_{ds}), and output characteristics which is a plot of I_{ds} against V_{ds} at different V_{gs}. There are three major electrical parameters that can be evaluated to determine the quality of the TFT: mobility (μ), threshold voltage (V_{th}), and subthreshold swing (S). Other electrical characteristics that are important are: the on-current because of its significance for current-driven Organic Light Emitting Diodes (OLEDs), off-current which is important in minimizing power consumption, and the on/off ratio. Fig. 2.6 and 2.7 illustrate the typical output and transfer characteristics (with mobility curves) of unpassivated TFTs, respectively. As discussed above, one can determine the quality of the TFT by looking at the output and transfer characteristics.

Typical output characteristics of *a*-IGZO TFTs have clear distinction between linear and saturation region and no current crowding phenomenon. The saturation region is also relatively flat with little fluctuation in I_{ds}. Electrical characteristics can be derived from the transfer characteristics. For instance, μ is derived from transfer characteristics at V_{ds} = 0.1 V using equation (2.1), where C_{ox} is the capacitance of the SiO_2 gate insulator, W is the width, and L is the length of the *a*-IGZO channel.

$$I_d = \frac{W}{L}\mu C_o V_d (V_g - V_{th}) \qquad (2.1)$$

In the linear region (at low V_{ds}), μ refers to the linear or field effect μ (μ_{lin} or μ_{FE}) and can be obtained by directly measuring the transconductance (g_m), which is a function of V_{gs} and is the ratio of the change in I_{ds} to the change in V_{gs}. Thus, the μ is obtained using the following equation:

$$\mu = g_m \frac{L}{WC_o V_d} \qquad (2.2)$$

Note that eq. (2.2) is valid only at low V_{ds} and that both μ and g_m is a function of V_{gs}. In general, the maximum value over the range of V_{gs} is the μ of the TFT. Fig 2.7 shows the very good transfer characteristics and mobility curve of *a*-IGZO TFT. The transfer characteristics show a steep S and μ greater than 10 cm^2/Vs. S is defined as the V_{gs} value that is necessary to increase the I_{ds} by 10 times in the subthreshold region. Ideally, the S value should be as small as possible or the subthreshold region of the transfer characteristics should be as steep as possible to enable quicker turn-on operation of the

TFT. V_{th} can be obtained through the linear plot of the transfer characteristics and by using a linear fit on the transfer characteristics in the linear region (low V_{ds}). The value of the x-intercept of this linear fit is the V_{th}. Alternatively, V_{th} can be defined as the V_{gs} at 1 nA.

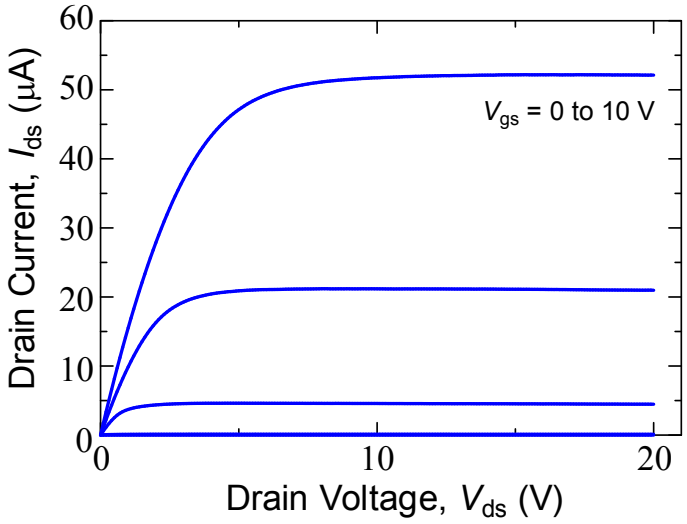

Fig. 2.6 Typical output characteristics of *a*-IGZO TFTs.

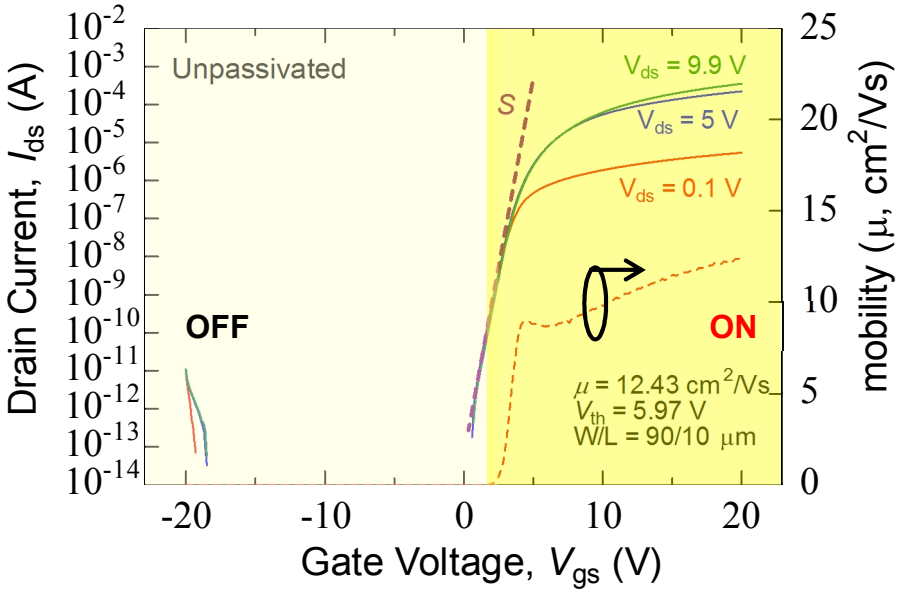

Fig. 2.7 Typical transfer characteristics and mobility curve of *a*-IGZO TFTs.

Table 2.II Summary of electrical properties of unpassivated *a*-IGZO TFT, Me 100 and Me 60/Ph 40; μ – mobility, V_{th} – threshold Voltage, S – subthreshold swing

	Unpassivated	**Me 100**	**Me 60/Ph 40**
μ (cm^2/Vs)	13.56 ± 1.57	16.10 ± 0.5	13.39 ± 2.07
V_{th} (V)	6.43 ± 0.55	5.44 ± 0.31	6.40 ± 1.70
S (V/dec)	0.18 ± 0.11	0.18 ± 0.09	0.15 ± 0.08

Table 2.II summarizes the electrical characteristics such as μ, V_{th}, and S for the unpassivated TFTs and the two types of NP-PSQ passivated TFTs. The data is the average measurement obtained by characterizing multiple TFTs at different locations on the sample. NP-PSQ especially Me 100 improved the μ and V_{th} of the unpassivated TFT. Me 60/Ph 40, on the other hand, have nearly the same electrical characteristics with unpassivated TFTs with a slightly steeper S. These results show that the NP-PSQ passivation materials did not degrade the electrical characteristics and can even enhance them.

2.3.4 Bias and humidity stress

Bias stress testing is an important tool to analyze the reliability of *a*-IGZO TFTs [8]. In general, when bias stress is applied to TFTs, degradation is manifested in the transfer characteristics as a change in μ, a change or shift in V_{th}, and hump effect or degradation in the subthreshold region [38, 39]. Humidity stress is also an important test to certify whether the passivation has excellent barrier ability against moisture. This is crucial since the major role of the passivation is to protect the sensitive backchannel and inhibit the adsorption of oxygen and water molecules on the *a*-IGZO [9-13].

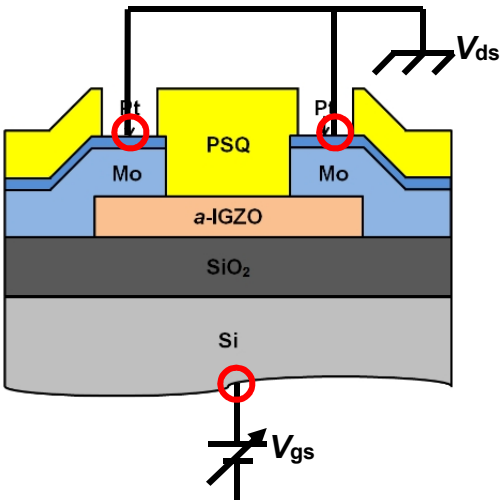

Fig 2.8 Illustration of bias stress test of *a*-IGZO TFTs. V_{ds} is set to 0 V while V_{gs} is changed according to the stress condition and applied for 10^4 s. Red circles denote the contact points.

Fig. 2.8 demonstrates how TFTs are subjected to bias stress. Stress can be applied by applying a constant voltage on the V_{gs}, V_{ds}, or both over a long period of time (~ 10^4 s). In this thesis, three types of bias stress are performed to test the effectiveness of the passivation layers: positive bias stress (PBS) by applying a V_{gs} of 20 V, negative bias stress (NBS; V_{gs} = -20 V), and negative bias illumination stress (NBIS; V_{gs} = -20 V, illumination with halogen lamp). Tested TFTs had a channel *W/L* of 90 μm and 10 μm, respectively. All stress conditions were performed for 10^4 s with no applied voltage across the source and drain electrodes (V_{ds} = 0 V). Bias stress tests were carried out with a semiconductor parameter analyzer (Agilent, 4156C) under room temperature, and air ambient atmosphere. Except for the NBIS, all tests were performed in the dark state. Transfer characteristics were measured before and after the stress at 100 s, 1000 s, and 10000 s.

Figure 2.9 illustrates the comparison of the evolution of transfer curves of Me 100, Me 60/Ph 40, and unpassivated *a*-IGZO TFTs under PBS after 10000 s. Both

NP-PSQ passivation, Me 100 and Me 60/Ph 40, showed very minimal threshold voltage shift (ΔV_{th}) of 0.49 V and 0.1 V, respectively. As expected, a large ΔV_{th} of 4.93 V is observed for the unpassivated TFTs, shown in Fig 4(c). Nevertheless, a comparison of the two passivated samples shows that the Me 60/Ph 40 samples showed not only a lesser ΔV_{th} but also lesser degradation in S. It is important to note that there is little degradation and change in S after each bias stress for both NP-PSQ passivation materials which suggests that degradation mechanism is largely due to charge trapping at the gate insulator interface and not charge injection or additional defect creation [40, 41]. Nevertheless, the NP-PSQ TFTs have better stability because other degradation mechanisms such as moisture and oxygen adsorption-desorption at the backchannel is inhibited.

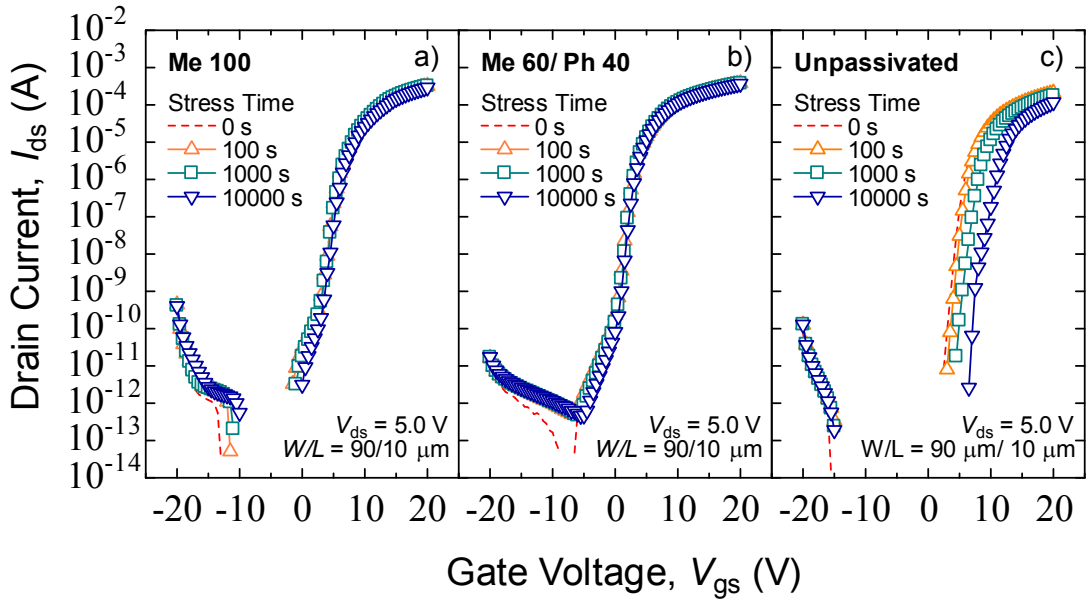

Fig 2.9 Evolution of transfer characteristics of a) Me 100, b) Me 60/ Ph 40 and c) unpassivated *a*-IGZO TFT under PBS (V_{gs} = 20 V)

Similar to the PBS results, both NP-PSQ passivated samples showed good NBS stability with a ΔV_{th} of less than -0.1 V. However, hump effect in the subthreshold region worsened after NBS. This hump effect is greater in NBS than in PBS. During PBS, the hump effect did not worsen as stress time increased but it worsened for all of the samples especially Me 60/Ph 40. Nevertheless, Me 100 was able to slightly suppress the hump effect more effectively than both unpassivated and Me 60/Ph 40. The mechanism of this hump is further discussed in section 2.4.

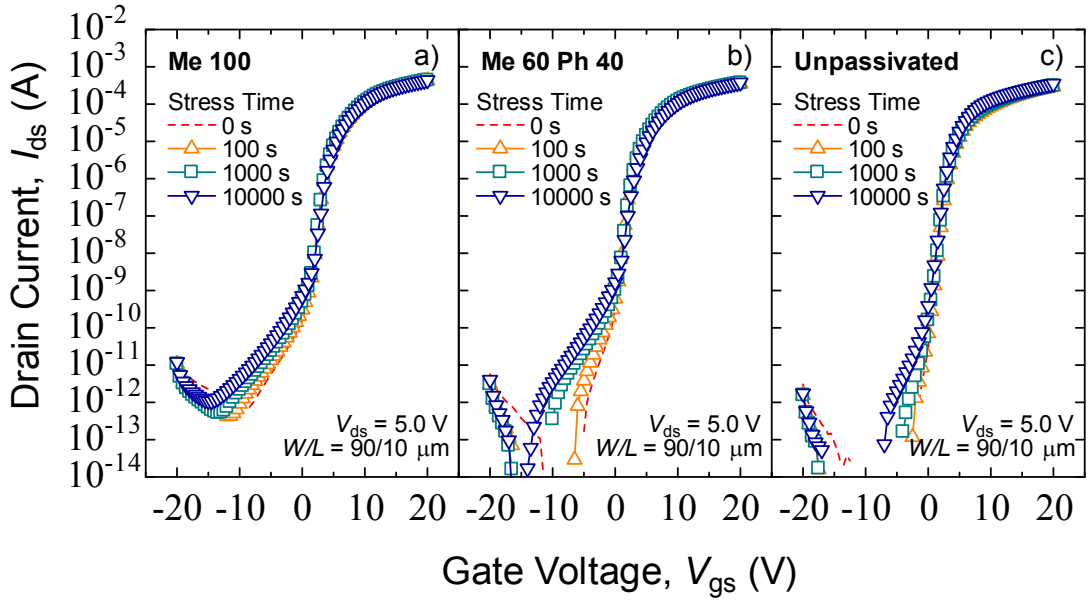

Fig 2.10 Evolution of transfer characteristics of a) Me 100, b) Me 60/ Ph 40 and c) unpassivated *a*-IGZO TFT under NBS (V_{gs} = -20 V)

Both Me 100 and Me 60/ Ph 40 had good reliability against NBIS as demonstrated in in Fig. 2.11. Fig 2.12b shows the spectra of the halogen lamp used showing the peak of the spectra near 600 nm. The power measured at 600 nm was 9.24 mW. Light intensity used was very high and measured to be 27,000 nits. Instability of unpassivated TFT under NBIS imposition is reflected in the very large ΔV_{th} of -15.85 V.

On the other hand, such large ΔV_{th} is not observed with both types of NP-PSQ which registered minimal ΔV_{th} of -2.45 V and -2.34 V for Me 100 and Me 60/ Ph 40 samples, respectively. Aside from having a smaller ΔV_{th}, Me 60/Ph 40 has a slightly lower off current. The ΔV_{th} of the two NP-PSQ passivation materials are competitive with and at times better than the ΔV_{th} observed in other inorganic passivation materials [42, 43]. Moreover, because of the simple solution process, degradation usually observed after deposition of inorganic passivation materials due to introduction of excess carriers and generation of traps [42] was not observed in TFTs passivated with NP-PSQ. Fig 2.12a summarizes the ΔV_{th} of Me 100, Me 60/Ph 40, and unpassivated TFTs as stress time increases. The figure shows how unpassivated TFTs are stable for the first few seconds (~100 s) but degrades as stress time is increased. Such a behavior is not observed for both NP-PSQ passivation materials which show barely any shift during stress. The disparity between the passivated and unpassivated samples is especially large during NBIS. These results show the effectiveness of both NP-PSQ passivation materials in suppressing ΔV_{th} especially the negative ΔV_{th} usually observed during NBIS.

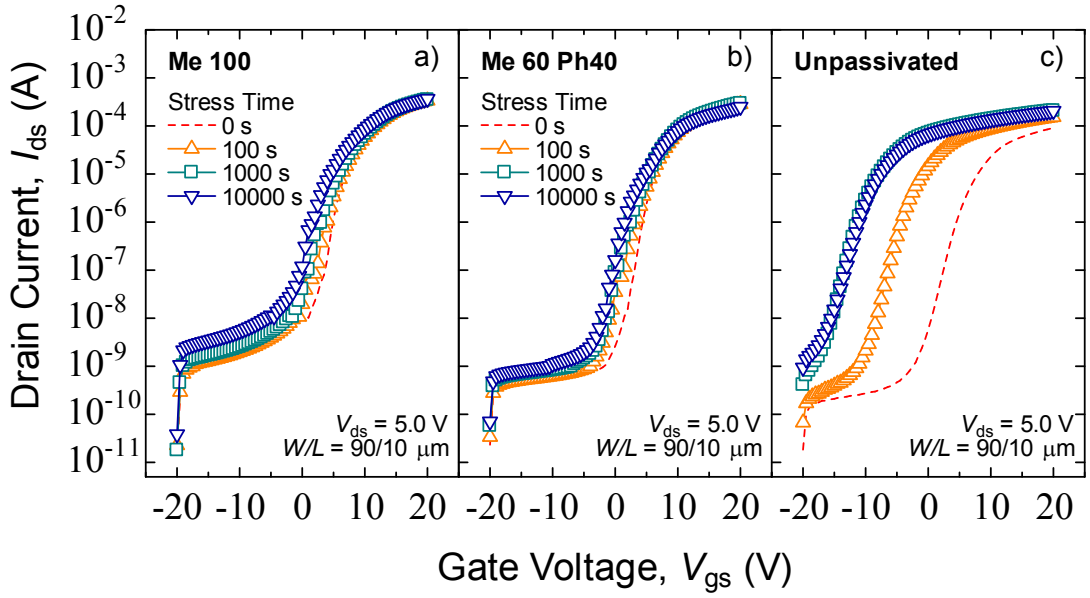

Fig 2.11 Evolution of transfer characteristics of a) Me 100, b) Me 60/ Ph 40 and c) unpassivated *a*-IGZO TFT under NBIS (V_{gs} = -20 V, illumination by halogen lamp, light intensity: 27,000 nit)

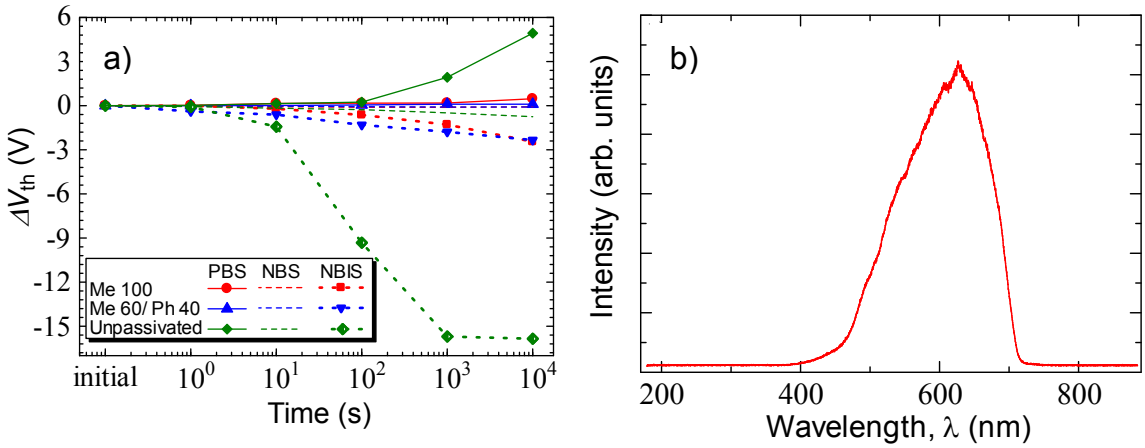

Fig 2.12 a) Summary of the variation in V_{th} of unpassivated TFTs, Me 100, Me 60/Ph 40 under PBS, NBS, and NBIS; b) Spectra of the halogen lamp used during NBIS (intensity was reduced during measurement to identify the peak)

Both unpassivated *a*-IGZO TFT and TFT passivated with Me 60/Ph 40 were subjected to humidity by placing them inside a temperature and humidity cabinet (ESPEC LH – 113). A 2 step humidity stress was performed: the temperature was first raised to 50 ^{o}C and relative humidity (rh) was set to 80% rh for 5 minutes and finally, the temperature was reduced to 25 ^{o}C and humidity was 95% rh for 2 hours. Transfer characteristics were measured before and right after the humidity stress test.

Fig 2.13 compares the transfer characteristics at different V_{ds} (linear to saturation region) of both MP 60/Ph 40 and unpassivated TFTs before and after the humidity stress. Me 60/Ph 40 did not show any shift in the V_{th} at different V_{ds}. In fact, the transfer characteristics look identical with each other with the exception of the slightly smaller hump at higher V_{ds} after the humidity stress. On the contrary, unpassivated TFT's V_{th} at different V_{ds} shifted heavily after humidity stress. This is naturally expected due to the adsorption of moisture (electron donor) and oxygen (electron acceptor) which can shift the V_{th} negative and positive direction, respectively. Nevertheless, this confirms that NP-PSQ passivation is an excellent barrier against ambient effects especially moisture.

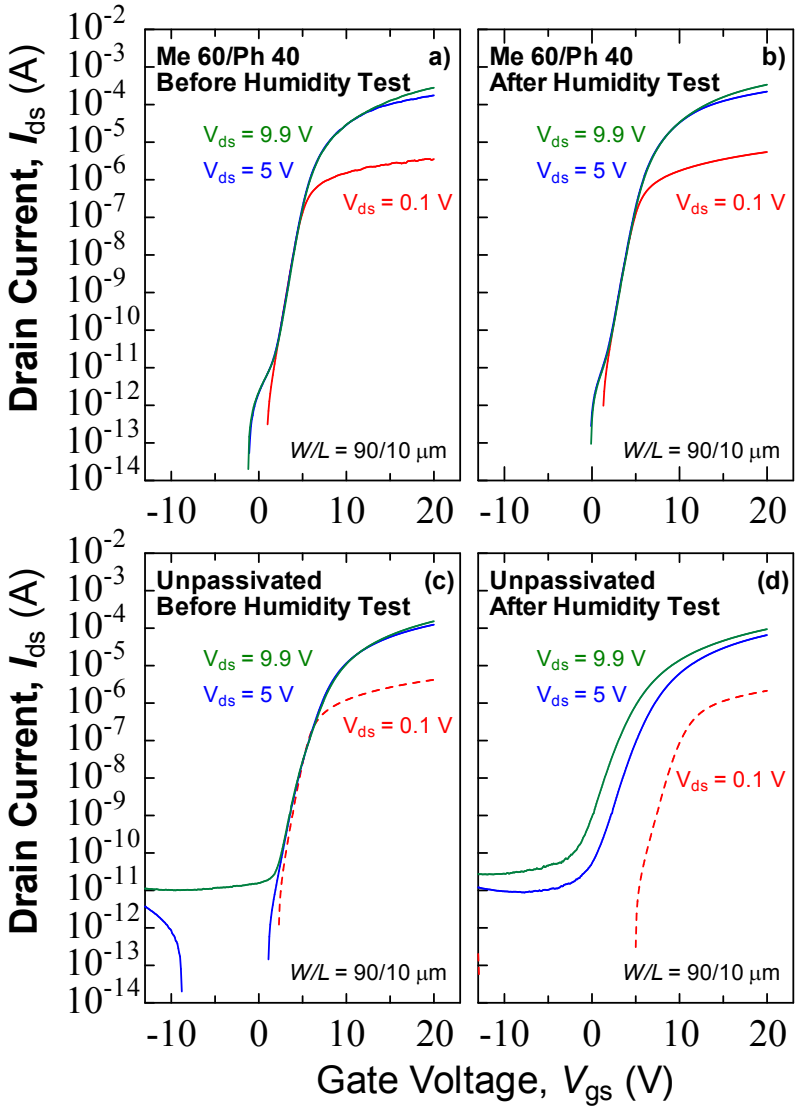

Fig 2.13 a) Evolution of transfer characteristics of Me 60/ Ph 40 (top row) a) before and b) after humidity test. Evolution of transfer characteristics of unpassivated *a*-IGZO TFT (bottom row) c) before and d) after humidity test. Humidity stress condition: 2 steps: 1st step: 50 ºC, 85% rh for 5 minutes; 2nd step: 25 ºC, 95% rh for 2 hours

2.4 Hydrogen and carbon in *a*-IGZO

Secondary Mass Ion Spectrometry (SIMS, ADEPT-1000, ULVAC-PHI) was performed to gain a clearer understanding of the mechanisms that enabled reliability improvement. Large amount of hydrogen and carbon was found in the *a*-IGZO layers of

both Me 100 and Me 60/Ph 40 as illustrated in Figs. 2.14 and 2.15. Both passivated samples had higher C and H in the *a*-IGZO layer especially near the *a*-IGZO/passivation interface compared to the unpassivated samples. The H and C diffused into the *a*-IGZO layer from the passivation layer during the post-bake process and the O_2 post-annealing process. This is apparent due to the increased H and C in both NP-PSQ passivation materials especially after O_2 post annealing. Me 60/ Ph 40 samples, especially those that were O_2 post annealed, had the highest H and C content. Incidentally, O_2 post annealed Me 60/ Ph 40 samples had the best reliability.

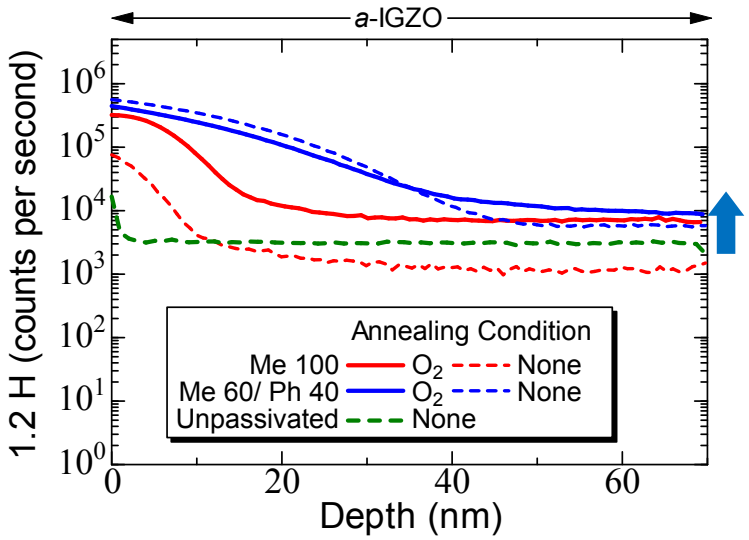

Fig 2.14 Hydrogen elemental profile in the *a*-IGZO layer of unpassivated and NP-PSQ TFTs. The 0 nm depth is the IGZO-passivation interface. Red, blue and green represent Me 100, Me 60/Ph 40, and unpassivated samples, respectively. Solid lines are O_2 annealed samples while dashed lines are unannealed samples

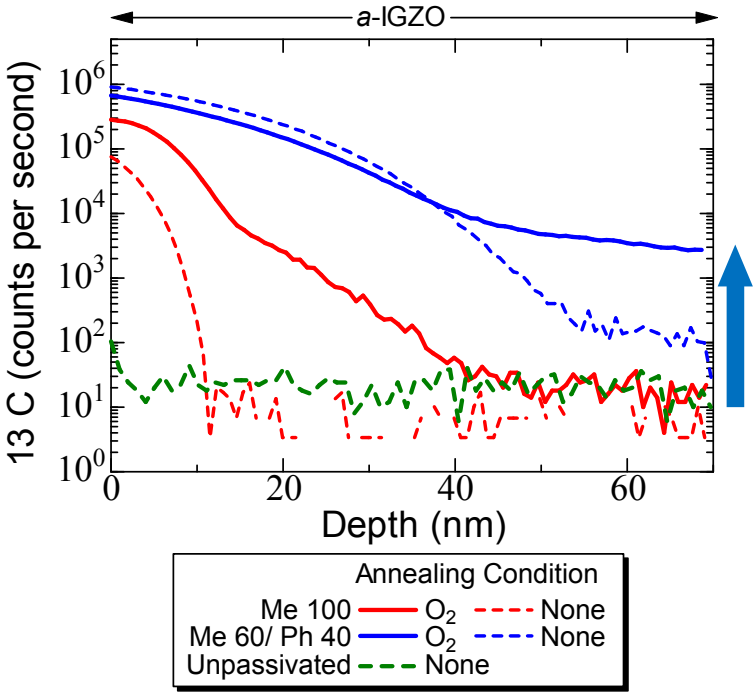

Fig 2.15 Carbon elemental profile in *a*-IGZO of unpassivated and NP-PSQ TFTs.

Considering that both unpassivated and passivated samples used the same gate insulator and processing conditions, reliability improvement in PBS and NBS can be explained by the excellent barrier ability of the passivation against moisture, adsorbed oxygen and in inhibiting other ambient effects. Nonetheless, having an excellent barrier will not completely remove NBIS instability unless the barrier is opaque or acts as a light shield. However, having an opaque passivation defeats the purpose of using *a*-IGZO for its transparency and limits its applications.

There are three major mechanisms for NBIS. The first mechanism is the photodesorption of oxygen-related molecules that were initially adsorbed on the backchannel [44]. This mechanism usually applies to unpassivated TFTs since oxygen can easily adsorb in the backchannel. In this mechanism, the adsorbed oxygen initially captures electrons from the channel when light is illuminated on the *a*-IGZO, oxygen will

be desorbed releasing additional electrons into the channel which shifts the V_{th} negatively. Since NP-PSQ is an excellent barrier and passivation, this degradation mechanism is unlikely to occur for NP-PSQ TFTs. The second cause of NBIS instability is the generation of photo-excited electron and hole pairs [45-47]. Electrons are photo-excited from the sub-gap states into the conduction band while holes are trapped near the channel-gate insulator or into the gate insulator itself. Because of the additional application of negative bias during NBIS, the additional electric field causes the holes to drift towards the gate insulator interface causing hole trapping. In addition, the photo-generated electrons can likewise accumulate in the backchannel. In this case, the photo-excitation of electron-hole pairs and the subsequent hole trapping in the front channel and electron trapping in the backchannel causes the large negative V_{th} shift.

Lastly, instability during NBIS is also largely attributed to oxygen vacancies (V_O) [48, 49]. Likewise, reducing the V_O amount or the sub gap states related to it can reduce the large negative ΔV_{th} observed during NBIS [50, 51]. Therefore, the change in bonding states of O 1s of the *a*-IGZO layer was analyzed by X-ray photoelectron spectroscopy (XPS, Kratos AXIS-165) to determine whether there is a reduction in V_O after passivation. The NP-PSQ passivation was etched away to expose the top *a*-IGZO layer prior to the XPS measurement.

The O 1s XPS profiles of Me 60/Ph 40 samples' *a*-IGZO layer are shown in Figs. 2.16(b-c) while those of unpassivated samples are shown in Fig. 2.16(a). Deconvolution of the O 1s spectra resulted in sub-peaks at ~529.9 eV (O_{III}), 531.3 eV (O_{II}), and 532 eV (O_I), which can be attributed to oxygen in oxide lattice, oxygen in an oxygen deficient region which roughly corresponds to V_O amount, and with hydroxides (OH), respectively [52-54]. The area ratio of O_{II} with respect to the total peak area (O_{all}) represents the

relative amount of V_O. The O_{II} area ratio (O_{II}/O_{all}) decreased from 43% to 38% for the O_2 post annealed Me 60/Ph 40 compared to its non post-annealed case. A similar and more pronounced trend is observed for Me 100 wherein O_{II}/O_{all} decreased from 41% to 30% for the O_2 annealed case compared to its unannealed case as shown in Fig. 2.17. Comparing the Vo quantity with the unpassivated samples shows that the O_{II} area ratio of both O_2 annealed NP-PSQ (30% for Me 100 and 38% for Me 60/Ph 40) are lower than the 45% value observed in unpassivated samples. These results suggest that there is a reduction in V_O after the passivation and O_2 post annealing. This V_O reduction is also reflected in the ΔV_{th} reduction for both O_2 annealed NP-PSQ samples especially during NBIS. The V_O reduction can be mainly attributed to the higher amount of H in both NP-PSQ samples. H can occupy the V_O site to form H at V_O site (H_O). Thus, H can passivate the electrical activity and degradation caused by V_O by lowering its amount [32, 55, 56].

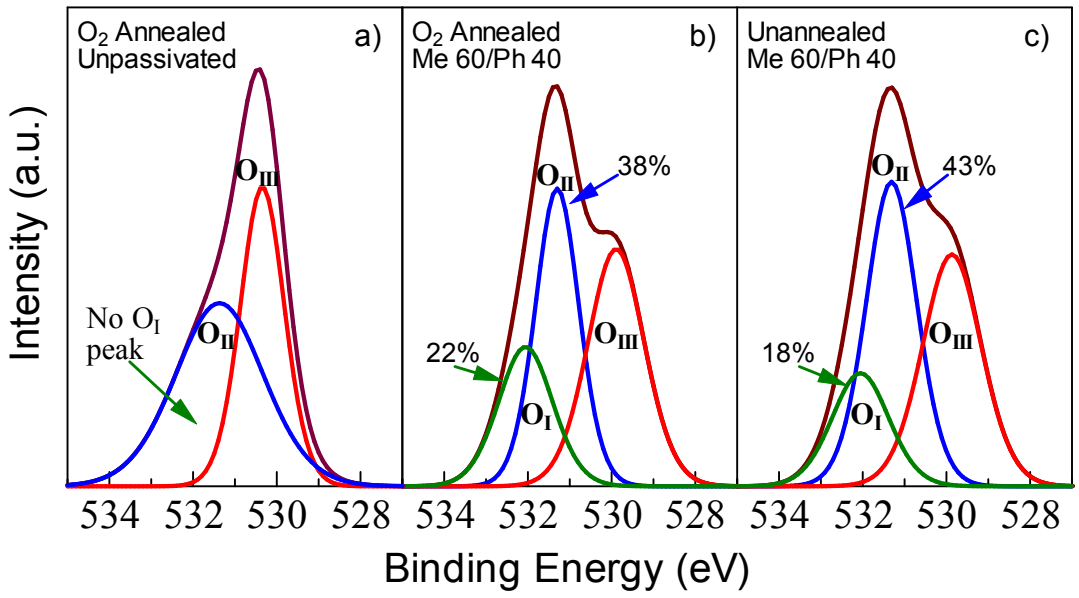

Fig. 2.16 O1s XPS spectra in the *a*-IGZO layer of a) O_2 post-annealed unpassivated sample b) O_2 annealed Me 60/ Ph 40 c) Non post-annealed Me 60/ Ph 40.

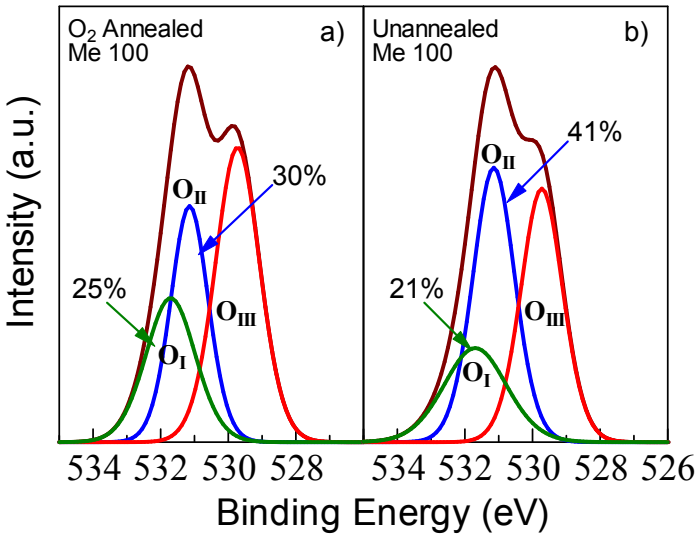

Fig. 2.17 O1s XPS spectra in the *a*-IGZO layer of a) O_2 post-annealed Me 100 and b) Non post-annealed Me 100.

Fig 2.18 shows how H behaves in *a*-IGZO. H can either occupy the V_O site to form H_O or form a bond with oxygen, especially excess oxygen, to form OH. The O1s XPS profiles also reflect this with the O_{II} area ratio decrease for passivated samples and the emergence of O_I bonding state which corresponds with OH bonds. A large amount of OH bonds will be problematic since it can instigate hump effect in the subthreshold region in the *a*-IGZO TFTs. The increase in OH amount is why a slight hump is observed in the initial characteristics and in the PBS and NBS results of NP-PSQ (see Fig 2.9, 2.10, and 2.13). The detailed mechanism of OH and its suppression is further discussed in section 3.4. Control of the amount and bonding type of H is therefore necessary. Nevertheless, as seen from the reliability results, H can enhance the reliability of *a*-IGZO TFTs.

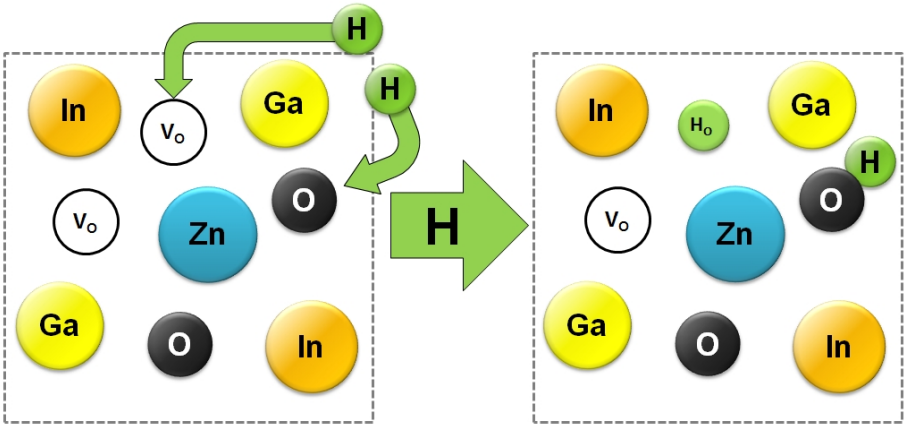

Fig. 2.18 Mechanism of hydrogen incorporation in *a*-IGZO showing how H can occupy the V_O to form H_O and how H can form bonds with O to form OH.

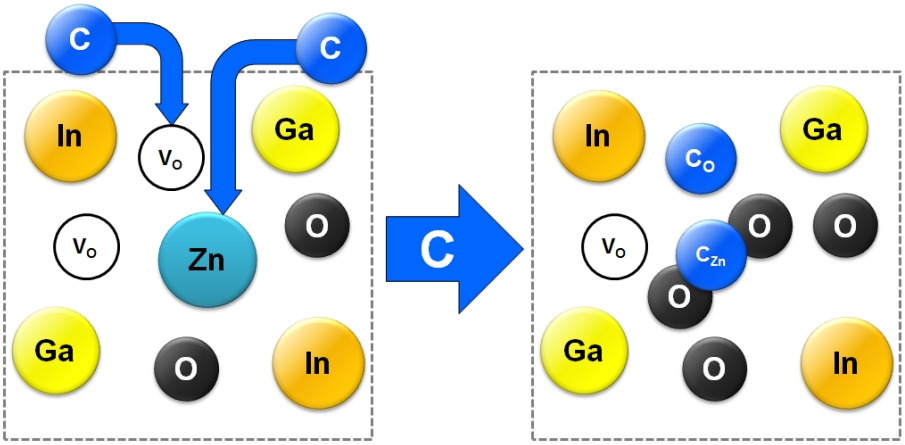

Fig. 2.19 Mechanism of carbon incorporation in *a*-IGZO showing how C can occupy the V_O to form C_O and how it can substitute the Zn site to form $C_{Zn} + 2O_i$.

Fig 2.19 illustrates how carbon behaves in *a*-IGZO TFT. Carbon like H can occupy the V_O site in ZnO. This C at the V_O site (C_O) is an acceptor [57, 58]. The similarity in the sizes of O and C also implies that C can easily occupy the V_O. However, other forms of C such as C at Zn site (C_{Zn}; donor) and C_{Zn} bonded with two interstitial oxygen ($C_{Zn} + 2O_i$), which is also an acceptor, has lower formation energy especially in O-rich conditions [58, 59]. Therefore, this suggests that it is unlikely that C_O has a large contribution in the V_O reduction because of its higher formation energy. Nevertheless, C still has a large role in

the reliability improvement because of its high concentration in *a*-IGZO especially in O_2 annealed Me 60/Ph 40 TFTs – the most reliable TFTs. The location of the Fermi level dictates the formation energies of C_{zn} and $C_{zn} + 2O_i$ in O-rich conditions. The formation energy of $C_{zn} + 2O_i$ is lower than C_{Zn} at Fermi levels greater than ~1 eV when measured from the top of the valence band [58]. Since the *a*-IGZO band gap is ~3.2 eV [13] and the Fermi level is located 0.16 eV below the conduction band in the unstressed state and moves further toward the conduction band during NBIS [60], the likelihood of C in the form of $C_{zn} + 2O_i$, which is an acceptor, is increased. Having more acceptors can help in alleviating the negative ΔV_{th} during NBIS. Furthermore, since C is largely concentrated near the *a*-IGZO-passivation interface, it is possible that the increased acceptors ($C_{Zn} + 2O_i$) can capture some of the photo-generated electrons during NBIS. The excess O from the $C_{Zn} + 2O_i$ can also effectively neutralize, through charge compensation, some OH that act as electron donor or form hump effect [61].

The presence of the O_I peak in the O 1s XPS profiles of NP-PSQ samples, which is not present in the unpassivated samples, can also be attributed to C bonding with O_i [59]. There is an increase in the O_I area ratio with respect to O_{all} from 18% in the unannealed Me 60/ Ph 40 to 22% in the O_2 annealed case. A similar increase from 21% to 25% is observed in the case of Me 100. This result is consistent with the marked increase in both C and H concentration in the *a*-IGZO layer of O_2 annealed NP-PSQ samples compared with both the unannealed NP-PSQ and unpassivated samples. Nonetheless, the assertions and mechanisms of C in are largely based on similar oxides such as ZnO. Conflicting reports have been presented on how C behaves in *a*-IGZO and other similar oxides such as ZnO. C from printed silver electrode precursor solutions has been shown to degrade the properties *a*-IGZO [62]. On the other hand, other reports have shown that C can be

used as a carrier suppressor and strong oxygen binder to improve the electrical characteristics and stability [63, 64]. The strong Lewis acid strength and bonding strength between C and oxygen contributed to the electrical characteristics and stability enhancements [63, 64]. Moreover, the doping level and bonding of C in oxide semiconductors are still unclear. Previous studies have focused on ZnO and have varying opinions whether C is an acceptor [58, 59] or a donor [65]. Nevertheless, C is expected to preferentially occupy the cation site in oxides that are present in IGZO such as ZnO, Ga_2O_3, In_2O_3, which implies that C will not be a source of carrier trapping in these oxide semiconductors [65]. Furthermore, as seen from the O1s XPS profiles, good *a*-IGZO stability, non-degradation of electrical characteristics, and the presented arguments, it is expected that C in *a*-IGZO is not a source of carrier trapping and should enhance the stability of *a*-IGZO.

2.5 Summary

The importance of passivation layers are discussed in this chapter. Two types of passivation materials: inorganic and organic are introduced and their advantages and disadvantages were discussed. Two novel organic-inorganic hybrid passivation materials based on PSQ: Me 100 and Me 60/Ph 40 are introduced and their properties are discussed. These NP-PSQ passivation materials have small weight loss during pyrolysis and are chemically resistant. Contact angle measurements also show that these NP-PSQ passivation materials are hydrophobic making them attractive passivation materials. AFM measurements show that the surface roughness of these passivation materials are quite smooth and are comparable to inorganic passivation materials. Both Me 100 and Me 60/Ph 40 have similar structures which explains why they have similar properties such as

excellent thermal properties, good film quality, and hydrophobicity. However, the difference in their constituent groups causes them to also have different properties. For instance, compared to the brittle Me 100, Me 60/Ph 40 have better mechanical properties such as a larger cracking threshold because of the addition of phenyl constituent groups.

Large improvement in reliability of *a*-IGZO TFT passivated with Me 100 and Me 60/Ph 40 is observed. Bias stress testing (PBS, NBS, and NBIS) reveal the excellent reliability of *a*-IGZO TFTs passivated with NP-PSQ. Humidity stress is also performed and confirmed the excellent barrier ability of NP-PSQ. Even though NP-PSQ are fabricated using a simple solution process, results show that their performance is comparable to inorganic passivation materials fabricated with more complicated vacuum processes.

Reliability mechanisms are discussed in section 2.4. SIMS measurements show a high concentration of C and H in the *a*-IGZO channel after passivation and especially after O_2 annealing. Degradation mechanisms related to NBIS are also discussed in section 2.4. Analysis of O 1s XPS profiles suggests that there is V_O reduction after passivation and after O_2 post annealing. H is shown to occupy the V_O thus reducing their amount. H can also form OH bonds that generated a slight hump effect in the initial characteristics, and during PBS and NBS. It is therefore suggested that strategies for controlling the OH amount or suppressing its activity should be sought after. The C behavior in *a*-IGZO is also discussed. Although C can sometimes be detrimental to the electrical performance of devices, a controlled amount located in the channel and not in the interface can contribute to the reliability. Analysis of formation energies and XPS profiles show that C assumed the form of $C_{Zn} + 2O_i$ in *a*-IGZO which is an acceptor. These acceptors reduced the negative V_{th} shift during NBIS and also captured some of the photo-generated electrons.

Excess oxygen from C_{Zn} + $2O_i$ also neutralized OH to some extent. In conclusion, we show that NP-PSQ passivation materials are excellent passivation materials and explain how H and C can enhance reliability.

References

[1] K. S. Karim, A. Nathan, M. Hack, W. Milne, IEEE Elect. Dev. Lett. **25,** (2004), 188.

[2] D. N. Kouvatsos and D. Davazoglou, Thin Solid Films, **426**, (2003) 250.

[3] S. Inoue, H. Ohshima, and T. Shimoda, IEDM Tech. Dig., (1997) 527.

[4] M. Matters, D.M. De Leeuw, P.T. Herwig, A.R. Brown, Synthetic metals **102**, (1999) 998.

[5] S. J. Zilker, C. Detcheverry, E. Cantatore and D. M. de Leeuw Appl. Phys. Lett. **79**, (2001) 1124.

[6] A. Salleo and R. A. Street, Phys. Rev. B, **70**, (2004) 235324.

[7] H. L. Gomes, P. Stallinga, F. Dinelli, M. Murgia, F. Biscarini, D. M. de Leeuw, T. Muck, J. Geurts, L. W. Molenkamp, and V. Wagner, Appl. Phys. Lett., **84**, (2004) 3184.

[8] A. Suresh and J. F. Muth, Appl. Phys. Lett., **92**, (2008) 033502.

[9] S.-Y. Sung, J. H. Choi, U. B. Han, K. C. Lee, J.-H. Lee, J.-J. Kim, W. Lim, S. J. Pearton, D. P. Norton and Y.-W. Heo, Appl. Phys. Lett. **96**, (2010) 102107.

[10] D. Kang, H. Lim, C. Kim, I. Song, J. Park, Y. Park, and J Chung, Appl. Phys. Lett., **90** (2007) 192101.

[11] J.-S. Park, J. K. Jeong, H.-J. Chung, Y.-G. Mo and H. D. Kim Appl. Phys. Lett., **92** (2008) 072104.

[12] J. K. Jeong, H. W. Yang, J. H. Jeong, Y.-G. Mo, and H. D. Kim, Appl. Phys. Lett., **93**, (2008) 123508.

[13] T. Kamiya, K. Nomura, and H. Hosono, Sci. Technol. Adv. Mater., **11**, (2010) 044305.

[14] B.-S. Jeong, C.-M. Park, M.-G. Kim, H.-J. Chung, T.-K. Ahn, S.-K. Heo, J.-H. Jeong, M.-K. Kim, H.-H. Park, J.-M. Huh, Y.-G. Mo, H.-D. Kim, and S. S. Kim, 2009 Digest of

Int. Meeting on Information Display (2009) 1040.

[15] A. Sato, K. Abe, R. Hayashi, H. Kumomi, K. Nomura, T. Kamiya, M. Hirano and H. Hosono, Appl. Phys. Lett. **94** (2009) 133502

[16] S.-H. Choi, and M.-K. Han, IEEE Electron Device Lett., **33,** (2012) 396.

[17] T.-C. Chen, T.-C. Chang, T.-Y. Hsieh, C.-T. Tsai, S.-C. Chen, C.-S. Lin, M.-C. Hung, C.-H. Tu, J.-J. Chang, and P.-L. Chen, Appl. Phys. Lett. **97**, (2010) 192103.

[18] J. Li, F. Zhou, H.-P. Lin, W.-Q. Zhu, J.-H. Zhang, X.-Y. Jiang, Z.-L. Zhang, Vacuum, **86,** (2012) 1840.

[19] M. K. Ryu et. al. 2009 Digest of Int. Meeting on Information Display (2009) 330.

[20] T. Arai, N. Morosawa, K. Tokunaga, Y. Terai, E. Fukumoto, T. Fujimori, T. Nakayama, T. Yamaguchi and T. Sasaoka, SID Symposium Digest of Tech. Papers, **41**, (2010) 1033.

[21] Y. Ko, S. Bang, S. Lee, S. Park, J. Park, and H. Jeon, Phys. Status Solidi RRL, **5,** (2011) 403.

[22] C. H. Ahn, K. Senthil, H. K. Cho, S. Y. Lee, Nature Sci. Rep., **3**, (2013) 2737.

[23] M.-C. Hung, W.-T. Lin, J. J. Chang, P.-L. Chen, C.-Y. Wu, C.-J. Lin, H.-L. Chiu, C.-Y. Huang, and Y.-C. Kao, 2010 Int. Workshop on Transparent Amorphous Oxide Semiconductors (2010).

[24] H.-S. Seo, J.-U. Bae, D.-H. Kim, Y. Park, C.-D. Kim, I. B. Kang, I.-J. Chung, J.-H. Choi, and J.-M. Myoung, Electrochem. Solid State Lett. **12** (2009) H348

[25] D. H. Kang, I. Kang, S. H. Ryu, Y. S. Ahn, J. Jang, J. of Display Technol., **9**, (2013) 699.

[26] S.-H. Choi , J.-H. Jang, Kim, J.-Joo, M.-K. Han, IEEE Elect. Dev. Lett. **33**, (2012) 381.

[27] X. Xu, L. Feng, S. He, Y. Jin, X. Guo, IEEE Elect. Dev. Lett. **33**, (2012) 1420.

[28] G.-W. Chang, T.-C. Chang, Y.-E. Syu, T.-M. Tsai, K.-C. Chang, C.-H. Tu, F.-Y. Jian, Y.-C. Hung, Y.-H. Tai, Thin Solid Films, **520**, (2011) 1608.

[29] W. J. Kim, C. S. Kim, S. J. Jo, H. S. Hwang, S. Y. Ryu, and H. K. Baik, Semiconductor Science and Technology **23**, (2008) 075034.

[30] S.-J. Seo, S. C. Yang, J.-H. ko, and B.-S. Bae, Electrochemical and Solid State and Letters, **14**, (2011) H375.

[31] T.-S. Chang, T.-C. Chang, P.-T. Liu, S.-W. Tsao, F.-S. Yeh, Thin Solid Films **516** (2007) 374 – 377.

[32] J. P. Bermundo, Y. Ishikawa, H. Yamazaki, T. Nonaka, and Y. Uraoka, ECS J. Solid State Sci. and Technol., **3**(2), (2014) Q16-Q19.

[33] J. P. Bermundo, Y. Ishikawa, H. Yamazaki, T. Nonaka, and Y. Uraoka, Mat. Res. Soc. Symp. Proc. **1633**, (2014) 118.

[34] R. H. Barney, M. Itoh, A. Sakakibara, and T. Suzuki, Chem. Rev., **95**, (1995) 1409.

[35] H. W. Ro, E. S. Park, C. L. Soles, and D. Y. Yoon, Chem. Mater., **22**, (2010) 1330.

[36] Y.-J. Cho, J.-H. Shin, S. M. Bobade, Y.-B. Kim, D.-K. Choi, Thin Solid Films, **517** (2009) 4115.

[37] J. Wu, Y. Chen, D. Zhou, Z. Hu, H. Xie, C. Dong, Materials Science in Semiconductor Processing, **29** (2015) 277.

[38] D. Kawakami, Y. Yasutake, H. Nisshizawa, and Y. Majima, Jpn. J. Appl. Phys., Part 2 **45**, (2006) L1127.

[39] C.-Y. Huang, J.-W. Tsai, T.-H. Teng, C.-J. Yang, and H.-C. Cheng, Jpn. J. Appl. Phys., Part 1 **39**, (200) 5763 2000.

[40] K. Nomura, T. Kamiya, H. Hirono, and H. Hosono, Appl. Phys. Lett. **95**, (2009)

013502.

[41] Jeong-Min Lee, In-Tak Cho, Jong-Ho Lee, and Hyuck-In Kwon, Appl. Phys. Lett. **93**, (2008) 093504.

[42] K. Nomura, T. Kamiya, and H. Hosono, Thin Solid Films, **520,** (2012) 3778.

[43] J. Li, F. Zhou, W.-Q. Zhu, J.–H. Zhang, X.-Y. Jiang, Z.-L. Zhang, Vacuum, **86,** (2012) 1840.

[44] S. Yang, D.-H. Cho, M. K. Ryu, S.-H. K. Park, C.-S. Hwang, J. Jang, and J. K. Jeong, Appl. Phys. Lett. **96**, (2010) 213511.

[45] K.-H. Lee, J. S. Jung, K. S. Son, J. S. Park, T. S. Kim, R. Choi, J. K. Jeong, J.-Y. Kwon, B. Koo, and S. Lee, Appl. Phys. Lett. **95** (2009) 232106.

[46] J. S. Park, W.-J. Maeng, H.-S. Kim, and J.-S. Park, Thin Solid Films **520** (2012) 1679.

[47] Y. Ueoka, Y. Ishikawa, J. P. Bermundo, H. Yamazaki, S. Urakawa, M. Fujii, M. Horita and Y. Uraoka, ECS J. of Solid Stat. Sci. and Technol. **3** (2014) Q3001.

[48] M. D. H. Chowdhury, P. Migliorato, and J. Jang, Appl. Phys. Lett., **97,** (2010) 173506.

[49] B. Ryu, H.-K. Noh, E.-A. Choi, and K. J. Chang, Appl. Phys. Lett., **97,** (2010) 022108.

[50] K. H. Ji, J.-I. Kim, H. Y. Jung, S. Y. Park, R. Choi, U. K. Kim, C. S. Hwang, D. Lee, H. Hwang, and J. K. Jeong, Appl. Phys. Lett., **98,** (2011) 103509.

[51] K.-S. Son, J. S. Park, T. S. Kim, H.-S. Kim, S.-J. Seo, S.-J. Kim, J. B. Seon, K. H. Ji, J. K. Jeong, M. K. Ryu, and S. Lee, Appl. Phys. Lett., **102,** (2013) 122108.

[52] S. Jeong, Y.-G. Ha, J. Moon, A. Facchetti, and T. J. Marks, Adv. Mater., **22** (2010) 1346.

[53] P. Liu, T. P. Chen, X. D. Li, Z. Liu, J. I.Wong, Y. Liu, and K. C. Leong, ECS Solid State Lett., **2,** (2013) Q21.

[54] K.K. Banger, Y. Yamashita, K. Mori, R.L. Peterson, T. Leedham, J. Rickard, and H. Sirringhaus, Nature Mater., **10**, (2011) 45.

[55] H. Noh, J.-S. Park, and K. J. Chang, J. Appl. Phys., **113,** (2013) 063712.

[56] Y. Hanyu, K. Domen, K. Nomura, H. Hiramatsu, H. Kumomi, H. Hosono and T. Kamiya, Appl. Phys. Lett., **103**, (2013) 202114.

[57] H. Pan, J. B. Yi, L. Shen, R. Q. Wu, J. H. Yang, J. Y. Lin, Y. P. Feng, J. Ding, L. H. Van and J. H. Yin, Phys. Rev. Lett., **99,** (2007) 127201.

[58] S. K. Nayak, M. E. Gruner, S. Sakong, S. Sil, P. Kratzer, S. N. Behera, and P. Entel, Phys. Rev. B, **86,** (2012) 054441.

[59] S. T. Tan, and X. W. Sun, Appl. Phys. Lett., **91,** (2007) 072101.

[60] J. G. Um, M. Mativenga, P. Migliorati, and J. Jang, Appl. Phys. Lett., **101,** (2012) 113504.

[61] K. Nomura, T. Kamiya, and H. Hosono, ECS J. Solid Stat. Sci. Technol., **2** (1) (2013) P5.

[62] Y. Ueoka, T. Nishibayashi, Y. Ishikawa, H. Yamazaki, Y. Osada, M. Horita, and Y. Uraoka, Jpn. J. Appl. Phys. **53**, (2014) 04EB03.

[63] S. Parthiban, S.-H. Kim, and J.-Y. Kwon, IEEE Elect. Dev. Lett., **35**, (2014) 1028.

[64] S. Parthiban, K. Park, H.-J. Kim, S. Yang, and J.-Y. Kwon, J. Elect. Mater., **43**, (2014) 4224.

[65] J. L. Lyons, D. Steiauf, A. Janotti, C. G. Van de Walle, Phys. Rev. Applied, **2**, (2014) 064005.

Chapter 3
Analysis of Photosensitive Organic-Inorganic Hybrid Polysilsesquioxane Passivation Layer and its Effect on *a*-IGZO.

3.1 Introduction

Aside from ambient effects, the backchannel of *a*-IGZO TFT is very sensitive to process damage. Stability and electrical characteristics of *a*-IGZO are heavily affected (usually becoming too conductive) by etching and plasma damage that occur during passivation and patterning processes [1-6]. To avoid this problem, other researchers have resorted to utilizing shadow masks [7, 8], lift-off process [9, 10], etch stop structure [11,12], and double layer channel structures [13] to prevent damage during fabrication. Passivation layers such as PSQ that are fabricated by non vacuum processes that do not involve plasma can also be used. Nevertheless, dry etching of the passivation during formation of contact holes can still cause damage. Therefore, development of a passivation that does not require etching is essential.

Section 3.2 discusses the different process damage that can be induced on *a*-IGZO during fabrication. It specifically examines the effect of dry etching of contact holes on the electrical characteristics of NP-PSQ passivated TFTs. The section describes how dry etching affects the electrical and initial transfer characteristics of the *a*-IGZO TFT. A method to reverse the damage caused by dry etching such as post-annealing is examined.

Photosensitive PSQ (P-PSQ) passivation layer is introduced in section 3.3. Because it is photosensitive, dry etching is not required in order to form the contact holes.

The advantage of its simpler fabrication compared to NP-PSQ is discussed. Furthermore, the effect of P-PSQ on the electrical properties and stability of *a*-IGZO TFTs are analyzed. Like NP-PSQ, the P-PSQ was subjected to bias and humidity stress to test its stability. More importantly, the electrical performance and stability of P-PSQ is compared with NP-PSQ and other passivation layers.

SIMS elemental analysis is also performed on P-PSQ passivated samples to study the elemental profile in the *a*-IGZO channel after P-PSQ passivation. Because P-PSQ is a hybrid material similar to NP-PSQ, it is expected that it will have a high amount of H and C in the *a*-IGZO channel after passivation. As stated in the previous chapter, it is interesting to analyze how different are the implications and effects of these elements especially H in P-PSQ compared to NP-PSQ. In addition, SIMS analysis shows a high amount of fluorine is present in the *a*-IGZO after P-PSQ passivation. F is a component of the photo-acid generator in the P-PSQ solution which aids in the photosensitive action of P-PSQ. Therefore, like in the case of H and C, it is important to analyze and understand the influence of fluorine on the stability and electrical properties of *a*-IGZO TFTs.

3.2 Process damage in *a*-IGZO TFT fabrication

The backchannel's sensitivity is not just limited to moisture and adsorbed oxygen. Chemicals, hard to remove resists, plasma, and process damage can contribute in its degradation. A passivation or an etch-stopper can be coated over the backchannel to address this but these passivated samples are also susceptible to the same problems present in unpassivated TFTs. For instance, etching of passivation to form the contact holes can damage the passivation, electrodes or both.

Fig 3.1 illustrates how RIE and post-annealing affects the electrical characteristics

and initial transfer curves of TFTs passivated with NP-PSQ. After NP-PSQ passivation (before RIE), the TFTs showed clear switching, small V_{th}, small S and good mobility. Nevertheless, RIE is needed to from contact holes so that measurement of the transfer characteristics. Although even without RIE, transfer characteristics can still be measured using the crude method of scratching off or mechanically removing a portion of the NP-PSQ passivation layer. Before etching, additional photoresist was spin-coated and patterned on the NP-PSQ TFTs to replicate the contact hole pattern. The following source gases are used to perform the RIE: CF_4 – 40 sccm/ O_2 – 10 sccm/ Ar – 100 sccm. Total gas flow rate is 150 sccm. The RIE was performed at room temperature at low chamber pressure (less than 10^{-3} Pa). ICP and bias power were set to 500 W and 200 W, respectively. Etch times for each NP-PSQ passivation layer are slightly different. Me 100 was completely etched after 30 s while Me 60/Ph 40 was etched after 35 s. Resist stripping was then performed. Transfer characteristics after RIE show a large negative V_{th} shift and significant increase in μ. Aside from this, there is a noticeable increase in the on-current and some degradation and increase in S. A very negative V_{th} and large S are not good because it increases the voltage required to operate and turn on the device. The RIE induced some damage on the PSQ which then affected its interface with the *a*-IGZO channel. Reports have shown that hydrogensilsesquioxane, which is a hybrid material similar to PSQ and has H constituent groups instead of methyl or phenyl, is damaged by O_2 plasma treatment [14]. Additional annealing treatment was shown to be effective in reversing the damage to the film [14]. In this case, both NP-PSQ TFTs (Me 100 and Me 60/Ph 40) were subjected to additional post-annealing treatment at 300 ^oC in O_2 for 2 h as an attempt to recover the initial characteristics. Comparison of transfer characteristics in fig. 3.1 shows that transfer characteristics are partially recovered after the extra annealing.

On-current decreased back close to the original value and V_{th} also partially recovered. Degradation in the subthreshold region was also suppressed after the annealing. Tables 3.I and 3.II list the changes in electrical characteristics before RIE, after RIE, and after post-annealing. Data shows that uniformity of electrical characteristics are very good for both Me 100 and Me 60/Ph 40 after passivation (before RIE). The uniformity worsens after the RIE process and slightly improves after the O_2 post-annealing, although it is not on par with the very good uniformity observed before RIE. These results suggest that RIE has a severe effect on *a*-IGZO and that the damage it causes cannot be easily reversed. Therefore, it is important to avoid subjecting *a*-IGZO TFTs to RIE or dry etching.

Table 3.I. Summary of electrical properties of Me 100 before RIE, after RIE, and after O_2 post annealing; μ – mobility, V_{th} – threshold voltage, S – subthreshold swing

	Before RIE	**After RIE**	**After O_2 post-anneal**
μ (cm^2/Vs)	12.44 ± 0.19	80.77 ± 4.03	16.10 ± 0.50
V_{th} (V)	7.72 ± 0.14	-1.92 ± 1.00	5.44 ± 0.31
S (V/dec)	0.19 ± 0.07	0.27 ± 0.11	0.18 ± 0.09

Table 3.II. Summary of electrical properties of Me 60/Ph40 before RIE, after RIE, and after O_2 post annealing; μ – mobility, V_{th} – threshold voltage, S – subthreshold swing

	Before RIE	**After RIE**	**After O_2 post-anneal**
μ (cm^2/Vs)	13.99 ± 0.31	68.75 ± 2.49	13.39 ± 2.07
V_{th} (V)	6.87 ± 0.13	-10.42 ± 1.27	6.40 ± 1.70
S (V/dec)	0.16 ± 0.03	0.91 ± 0.15	0.15 ± 0.08

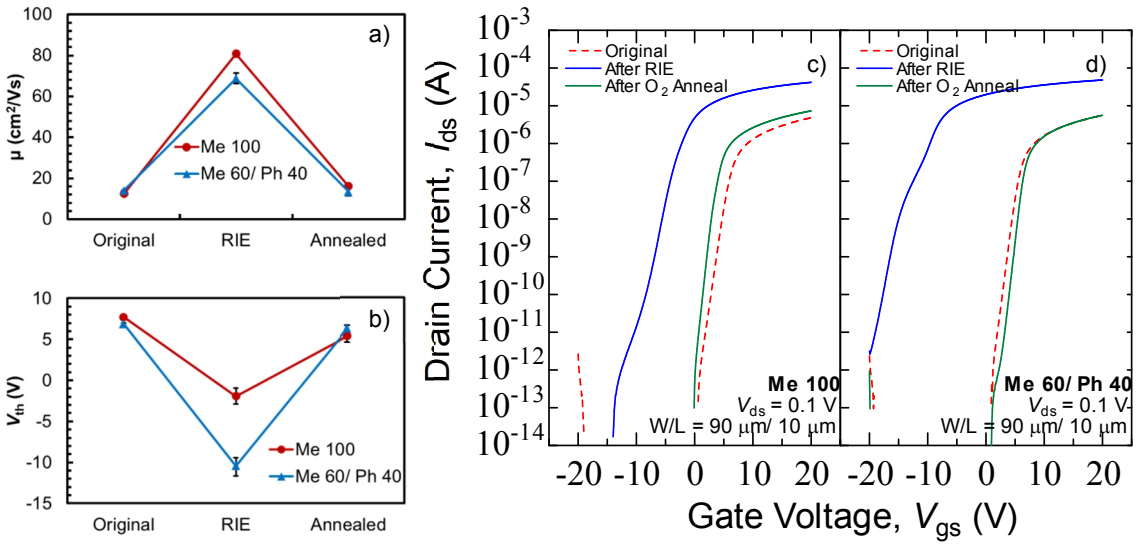

Fig 3.1 a) Evolution of electrical characteristics such as a) μ and b) V_{th} before RIE, after RIE, and after the O_2 post annealing process. Evolution of transfer characteristics of c) Me 100 and d) Me 60/Ph 40 before RIE, after RIE, and after O_2 post annealing

3.3 Photosensitive polysilsesquioxane passivation layer

The development of photosensitive passivation can prove very useful in circumventing the adverse effect of RIE. If a photosensitive material is used, contact hole formation can be done through standard lithography processes without the need for any dry etching. Other researchers have reported photosensitive organic materials such as photosensitive polyimide films [15] and photosensitive passivation layers in *a*-Si TFT [16]. Nevertheless, there has been no report yet of a reliable photosensitive organic-inorganic hybrid passivation layer compatible with *a*-IGZO TFTs. In section 3.2.1, the material properties of PSQ were discussed and it was shown that the properties of PSQ can be tuned by modifying or adding functional groups or by altering the ratio of the copolymers. Other groups have successfully modified PSQ in order to change its surface property [17], permittivity [18], resistivity [19], and electrical performance [20]. Photo-curable PSQ has also been developed [19, 21]. However, the focus of these works

and most PSQ research applied in TFTs are in developing gate insulators for organic TFTs [20-24] or as passivation for Si-based TFTs [19]. In this work, a photosensitive organic-inorganic hybrid passivation layer based on PSQ is fabricated by solution process. The photosensitivity of the P-PSQ passivation ensures that no plasma or dry etching damage will be incurred in *a*-IGZO TFTs. Furthermore, its photosensitivity further simplifies the fabrication of passivation layers. Aside from the simpler fabrication, this P-PSQ passivation retains the excellent stability and barrier ability observed in NP-PSQ. TFTs passivated by P-PSQ also showed enhancement in their electrical characteristics and suppressed hump effect.

3.3.1 Device fabrication

Fabrication of the unpassivated *a*-IGZO TFT in P-PSQ TFTs is the same with the fabrication process employed for the unpassivated *a*-IGZO TFT in NP-PSQ *a*-IGZO TFTs. The fabricated TFT had a bottom gate top contact structure. The channel used is a 70 nm thick *a*-IGZO deposited on heavily doped n-type Si (resistivity < 0.002 Ω·cm) with 100 nm thick thermal silicon oxide. The Si and SiO_2 were used as the gate and gate insulator, respectively. The *a*-IGZO islands were formed by patterning the *a*-IGZO by conventional photolithography and wet etched by an HCl (0.02% mol/L) solution. A stack of 80 nm Mo and 20 nm Pt deposited using RF magnetron sputtering deposition and patterned via lift off technique was used as source/drain electrodes. Note that no dry etching is performed even in the fabrication of the unpassivated *a*-IGZO TFTs. TFTs were then annealed at 300 ^{o}C for 2 h under N_2/O_2 ambient atmosphere (AT anneal). Similar to NP-PSQ, a simple solution process was used to coat P-PSQ on the *a*-IGZO TFT. The P-PSQ passivation precursor was first spin coated at a main spin of 1200 rpm for 20 s.

Prebaking at 100 ºC for 90 s was then done to evaporate the solution. Because it is photosensitive, formation of contact holes was performed in P-PSQ by first patterning and curing via UV photolithography. Post cure N_2 annealing was then performed at 250 ºC for 2 h, followed by additional O_2 annealing for 2 h. Comparison of the P-PSQ process with the NP-PSQ process in fabricating the same structure (passivated *a*-IGZO TFT with contact holes) is shown in Fig. 3.2. The P-PSQ fabrication process further simplifies the already straightforward fabrication process employed by NP-PSQ. By removing the processes related to etching, the steps in the process flow are reduced by more than half. Omitting these parts related to etching in the P-PSQ process such as dry etching and photoresist stripping is significant because these are sources of process damage. As discussed earlier, etching can damage the passivation and can induce damage at the interface of the passivation and the backchannel. Resist stripping is also problematic since complete removal of resist can sometimes be a problem. Resist stripping also increases the chance of exposing the TFT to possible contaminants because of the additional processing and solutions that are used. By using P-PSQ, fabrication of passivated *a*-IGZO TFT does not require any dry etching. The inset of Fig. 3.2 illustrates the P-PSQ chemical structure. The P-PSQ structure is a modified NP-PSQ (Me 60/Ph40) with an added siloxane polymer block. Furthermore, fluorine containing photo-acid generator is added in order to facilitate the photosensitive action of P-PSQ. Corresponding passivated and unpassivated film samples were also fabricated by coating P-PSQ and *a*-IGZO film on Si/SiO_2 substrate for passivated samples and only coating *a*-IGZO film on Si/SiO_2 substrate for unpassivated samples.

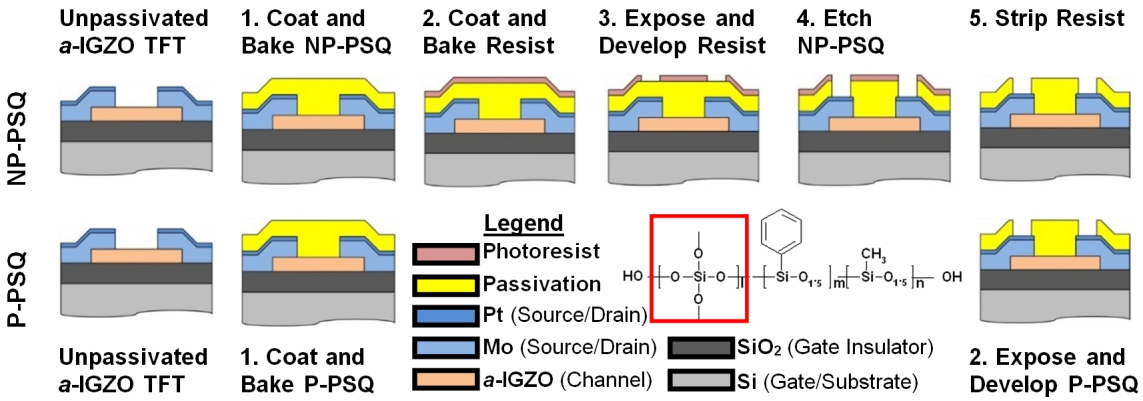

Fig. 3.2 Comparison of process flow between non-photosensitive PSQ (NP-PSQ) and photosensitive PSQ (P-PSQ) in depositing a passivation layer and forming passivated *a*-IGZO TFTs with contact holes. Inset is the P-PSQ structure showing the additional siloxane block (enclosed in red rectangle) compared with NP-PSQ.

3.3.2 Electrical characteristics

Since P-PSQ is similar to NP-PSQ, we also expect that its effect on the electrical characteristics of *a*-IGZO TFT is similar. Table 3.III summarizes the electrical characteristics such as μ, V_{th}, and S before and after passivation of P-PSQ on *a*-IGZO TFTs. The data is the average measurement of multiple TFTs evaluated at different locations on the sample/substrate. TFTs that were characterized have a W/L of 90/10 μm. The data reveals that P-PSQ enhanced the electrical characteristics of *a*-IGZO TFTs. The μ extracted from the transfer characteristics increased by 21% from an average of 14.10 cm^2/Vs to 17.07 cm^2/Vs. Compared with NP-PSQ, the mobility enhancement observed in P-PSQ is much greater especially compared with Me 60/Ph 40. A slight decrease in V_{th} from 3.68 V to 2.5 V is also observed. The S value of P-PSQ TFTs is also very uniform and no hump effect or degradation in the subthreshold region is observed. This is unlike NP-PSQ where some samples would exhibit a hump in their initial characteristics.

Table 3.III. Summary of electrical properties before passivation (unpassivated *a*-IGZO TFT) and after passivation (P-PSQ *a*-IGZO TFT); μ – mobility, V_{th} – threshold Voltage (V_{gs} at 1 nA), S – subthreshold swing

	Unpassivated	**P-PSQ**
μ (cm^2/Vs)	14.10 ± 1.00	17.07 ± 1.72
V_{th} (V)	3.68 ± 0.65	2.50 ± 0.49
S (V/dec)	0.20 ± 0.06	0.19 ± 0.01

3.3.3 Bias and humidity Stress

P-PSQ TFTs were also subjected to the same types of stress applied to NP-PSQ such as: PBS (V_{gs} = 20 V), NBS (V_{gs} = -20 V), and NBIS (V_{gs} = -20 V and illumination with halogen lamp). During all stress tests, voltage was not applied across the source and drain regions (V_{ds} = 0 V). Except for NBIS, all stress tests and characterizations were performed in dark conditions. The transfer characteristics were measured after 100 s, 1000 s, and 10000 s at V_{ds} = 5 V after 100 s, 1000 s, and 10000 s of stress application to monitor the variation of V_{th} and check for degradation. Characterized TFTs had a channel *W/L* of 90/10 μm.

Fig. 3.3 compares the variation of transfer curves between P-PSQ passivated TFT (a-c) and unpassivated TFT (d-f) after PBS, NBS, and NBIS. As expected, P-PSQ passivated TFTs had excellent stability to bias stress compared with unpassivated TFTs. There was barely any ΔV_{th} during PBS and NBS for P-PSQ after 10000 s of stress. The observed ΔV_{th} was quite small, only 0.5 V for both PBS and NBS. On the other hand, a large ΔV_{th} of 5 V is seen after PBS of 10000 s for the unpassivated case. Moreover, there is a slight degradation in the subthreshold region can be observed after 10000 s of PBS for the unpassivated TFT indicating additional creation of defect and trap states. This degradation and large ΔV_{th} is not observed for P-PSQ TFTs. Moreover, although the

unpassivated TFT is quite stable after NBS with a ΔV_{th} of only -0.5 V, hump effect is clearly observed. This hump effect worsens as the bias stress time is increased. No hump effect is observed at all for the P-PSQ TFTs. The performance of the P-PSQ passivation layer under PBS and NBS is comparable to several inorganic passivation layers [27] and better than most organic passivation layers [28-31]. The excellent stability of P-PSQ is also evident in its superb NBIS performance where the ΔV_{th} is only -2.5 V compared to the very large ΔV_{th} of -15.6 V for unpassivated TFTs. The power of the halogen lamp used is 9.24 mW at 600 nm (near the peak of the spectrum). 27,000 nits was the measured light intensity). It is also important to note that P-PSQ is transparent just like NP-PSQ, so its excellent performance to NBIS is not due to P-PSQ blocking the light away from *a*-IGZO. Fig 3.4 shows a summary of the ΔV_{th} of unpassivated TFTs, Me 60/ Ph 40, and P-PSQ TFTs. The comparison shows how both Me 60/ Ph 40, which has the better stability among the two types of NP-PSQ, and P-PSQ have similar performance. Although Me 60/Ph 40 has a slightly lower ΔV_{th} than P-PSQ after PBS, a slight hump effect is observed in its transfer characteristics during PBS. As discussed in section 2.3.4, this hump effect is especially worse during NBS. On the other hand, this hump effect is suppressed in both PBS and NBS for the P-PSQ TFTs. Comparable NBIS performance is also observed in both P-PSQ and NP-PSQ where the ΔV_{th} of the NP-PSQ is also ~ -2.5V. However, P-PSQ TFT has a lower off current during NBIS compared to both the NP-PSQ and unpassivated cases. To the best of our knowledge, these bias stress results are the best results for oxide TFTs passivated by an organic-inorganic hybrid passivation material.

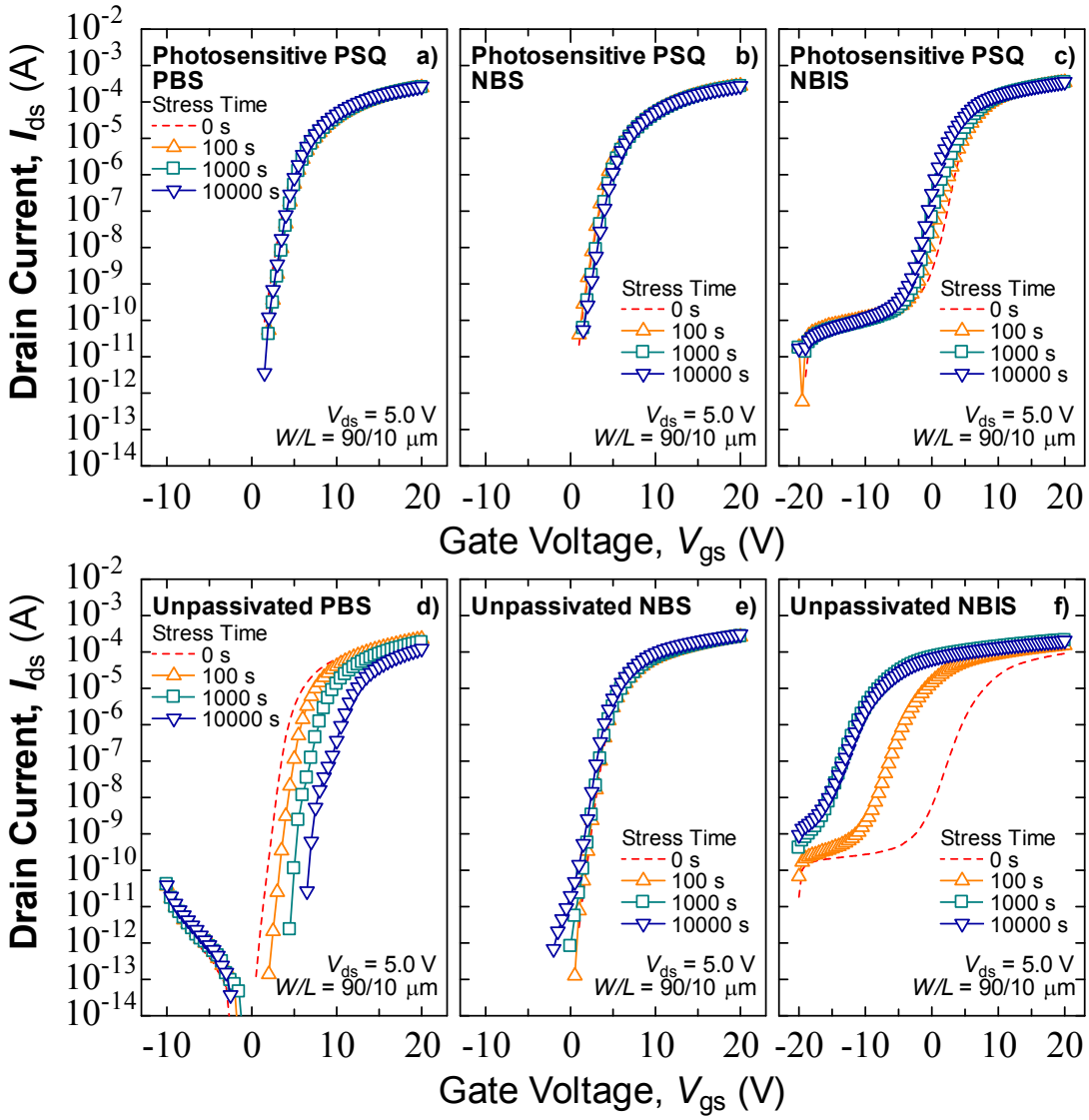

Fig. 3.3. Evolution of transfer characteristics of photosensitive PSQ *a*-IGZO TFT (top row) under a) PBS, b) NBS, and c) NBIS. Evolution of transfer characteristics for unpassivated *a*-IGZO TFT (bottom row) after d) PBS, e) NBS, and f) NBIS. Stress conditions: PBS (V_{gs} = 20 V); NBS (V_{gs} = -20 V); and NBIS (V_{gs} = -20 V, illumination by halogen lamp, light intensity: ~ 27,000 nit).

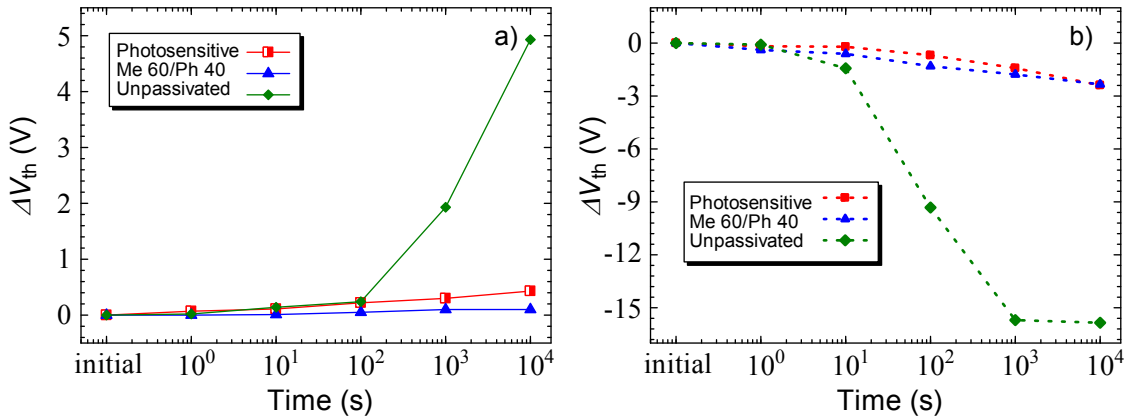

Fig 3.4 Summary of the variation in V_{th} of unpassivated TFTs, Me 60/Ph 40, and P-PSQ under a) PBS and b) NBIS

The good PBS and NBS performance of P-PSQ TFT can be explained by the excellent barrier ability of P-PSQ to inhibit ambient effects such as adsorption of moisture and excess oxygen. Like NP-PSQ, P-PSQ TFTs were subjected to humidity testing to further test its effectiveness as a barrier especially against moisture. Figure 3.5 compares the transfer curves of both P-PSQ TFTs and unpassivated TFTs at different V_{ds} before and after the humidity stress. Similar to NP-PSQ, the transfer curves of P-PSQ did not shift at different V_{ds} both before and after humidity stress. However, there is a slight increase in the off-current especially at high V_{ds} which is probably due to de-trapping or activation of some holes after the humidity stress. Nevertheless, hump effect did not develop in the P-PSQ TFTs even after humidity stress. Again, the hydrophobicity of P-PSQ due to the non-polar methyl and phenyl constituents helped in reducing the effect of moisture [17]. Therefore, its hydrophobicity makes P-PSQ a good candidate material in water-repellant applications.

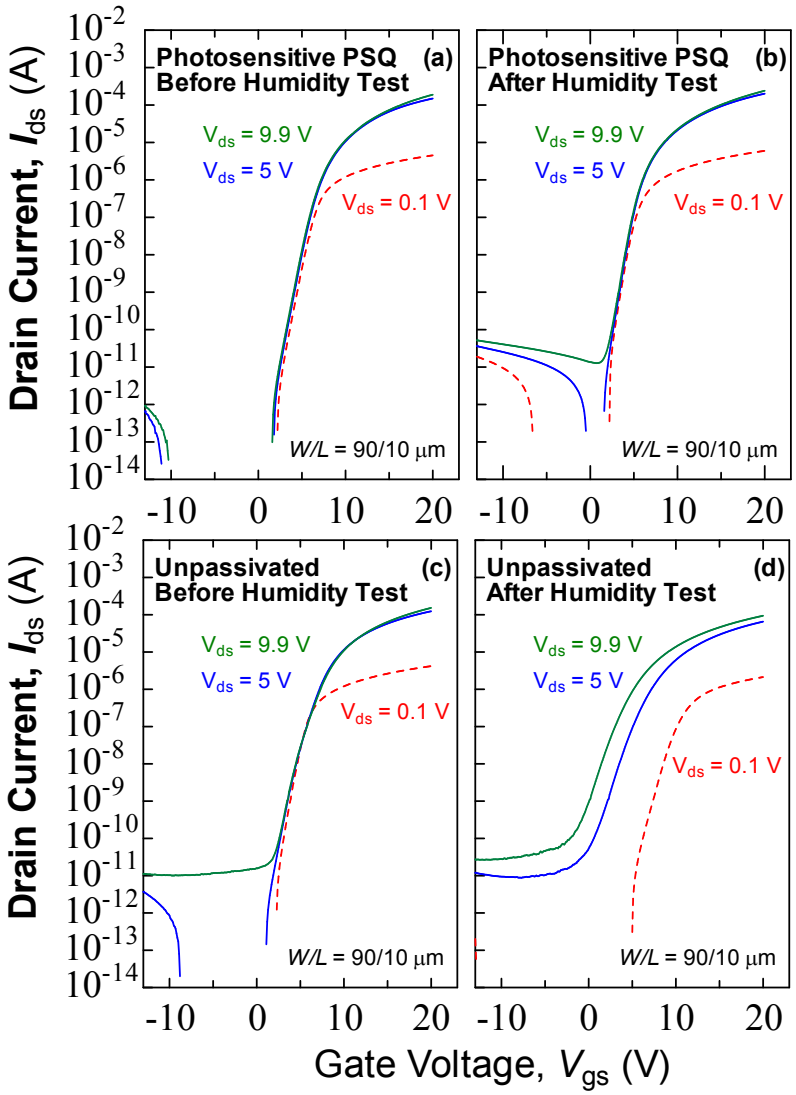

Fig. 3.5. Evolution of transfer characteristics of photosensitive PSQ a-IGZO TFT (top row) a) before and b) after humidity test. Evolution of transfer characteristics of unpassivated *a*-IGZO TFT (bottom row) c) before and d) after humidity test. Stress conditions: 2 steps: 1st step: 50ºC, 85% rh for 5 minutes; 2nd step: 25ºC, 95% rh for 2 hours.

3.4 Fluorine in *a*-IGZO

SIMS analysis (ADEPT-1010, ULVAC-PHI) is once again performed to analyze the effect of P-PSQ on the *a*-IGZO. Figs 3.6 and 3.7 compare the hydrogen and fluorine profiles, respectively, in Me 60/Ph 40 and P-PSQ TFTs. Even higher H concentrations

were found in the *a*-IGZO layer of P-PSQ compared to Me 60/Ph 40. In addition, a relatively high amount of fluorine and/or OH is observed in the P-PSQ compared to Me 60/Ph 40. More importantly, figs 3.6 and 3.7 show that there is barely any change in the H and F elemental profiles before and after exposure to humidity for P-PSQ while a slight increase is observed for Me 60/Ph40. These results suggest that, indeed, the P-PSQ is effective in acting as a barrier and shows that it is stable against humidity. Fig. 3.8 shows the SIMS profile in the *a*-IGZO layer of the P-PSQ and unpassivated samples. A much higher C, H, and F in the *a*-IGZO layer is again observed for P-PSQ compared to unpassivated sample. Just like NP-PSQ, the fact that P-PSQ is an organic-inorganic hybrid passivation explains the high C and H concentrations which were introduced during the passivation and annealing processes. It is also important to note that the 19 element count is shared between 19F and 18O + 1H or 19OH. Furthermore, F is part of the P-PSQ passivation solution and both the unpassivated and NP-PSQ TFTs are not fluorinated. This explains the almost 2 orders of magnitude increase in the 19F count of P-PSQ compared to both the unpassivated and NP-PSQ cases. This also implies two things: firstly, the 19 element count in both the unpassivated and NP-PSQ case is mostly for 18O + 1H (not F) and secondly, the 19 element count is mostly F for the P-PSQ.

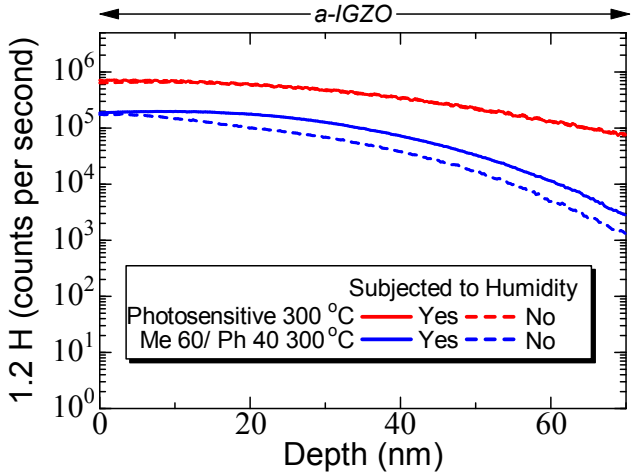

Fig 3.6 Hydrogen elemental profile in the *a*-IGZO layer of Me60/Ph 40 and P-PSQ TFTs. The 0 nm depth is the IGZO-passivation interface. Blue and red lines represent Me 60/Ph 40, and P-PSQ samples, respectively. Solid and dashed lines are samples subjected to humidity and not subjected to humidity, respectively.

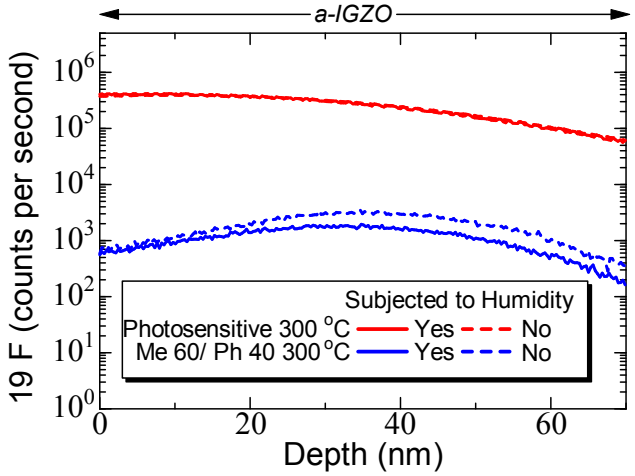

Fig 3.7 Fluorine elemental profile in the *a*-IGZO layer of Me60/Ph 40 and P-PSQ TFTs.

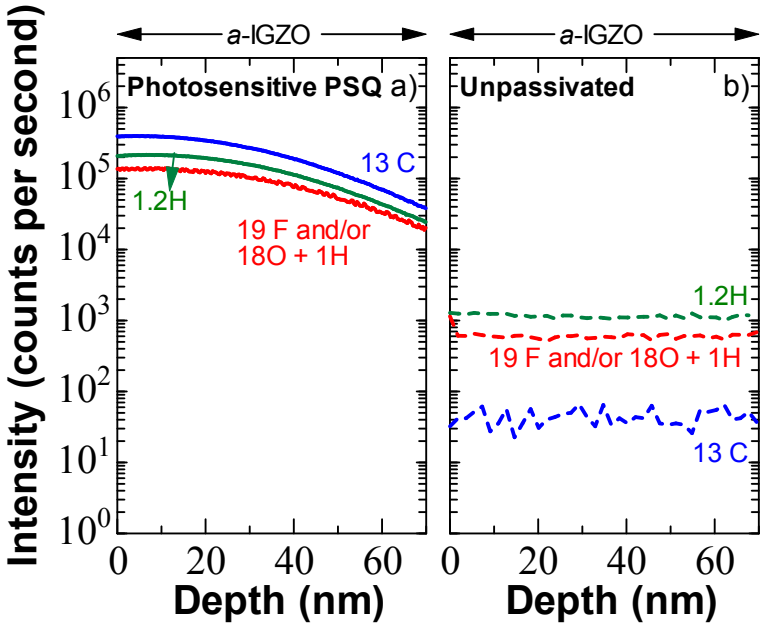

Fig 3.8 Comparison of elemental profile in the *a*-IGZO layer of P-PSQ and unpassivated TFTs. Blue, green, and red lines represent 13C, 1.2H, and 19F and/or 18O + 1H respectively. Solid and dashed lines are P-PSQ and unpassivated samples, respectively.

The high amount of H, C, and F concentration are keys to the improved stability of the P-PSQ especially during NBIS. As discussed previously, PBS, NBS, and humidity stress are largely affected by the barrier ability of the passivation to inhibit ambient effects which is why P-PSQ had excellent stability against these types of stress. Nevertheless, for NBIS, having an excellent barrier ability is not sufficient since ambient effects are not the main cause of instability. In NBIS, controlling the amount of V_O is crucial since it plays a major role in the degradation phenomenon during NBIS [33, 34]. As explained previously, H can occupy the V_O site to form H_O and thus reduce the V_O concentration leading to better NBIS stability. This mechanism is explained in section 2.4. However, a large amount of H would also lead to formation of weak OH bonds that are detrimental to the reliability. This is because during stress, especially during NBS, H can dissociate from the weak OH bonds and drift towards the source/drain-*a*-IGZO interface

[35]. Mobile H ions and other positive charges that accumulate near the source/drain-channel interface and backchannel-passivation interface is the major cause of hump effect during stress [36]. The location of these mobile H ions and other positive charges (which is near to the edge side; source/drain region) enables the quicker activation of these parasitic transistors compared with the main transistor leading to the observed hump effect [35,36].

To reduce this hump effect, it is necessary to either control the amount of OH in *a*-IGZO or to stabilize the weak OH bond so that the H ion cannot easily dissociate especially during stress. Controlling the OH amount can be accomplished by developing conditions such that H_O formation is more preferred energetically compared to OH formation. Furthermore, developing a passivation with lesser amount of OH functional groups is also desirable. This is why most of the attached functional groups in both NP-PSQ and P-PSQ are methyl and phenyl, and not OH-based. The substantial increase in F in *a*-IGZO can address the hump effect due to OH and is an important factor in the stability of P-PSQ passivated TFTs. Previous reports have shown that F can improve both the electrical properties and stability of oxide TFTs [37-40]. Fig 3.9 illustrates the mechanism of F in the *a*-IGZO layer. Because of the similarity in ionic radii of F and O, F can readily substitute weakly bonded oxygen or easily occupy V_O as shown in eq. (3.1) and (3.2).

$$O_O^{\,x} + F^- \rightarrow F_O^{\cdot} + e^- \qquad (3.1)$$

$$V_O^{\cdot\cdot} + 2e^- + F^- \rightarrow F_O^{\cdot} + e^- \qquad (3.2)$$

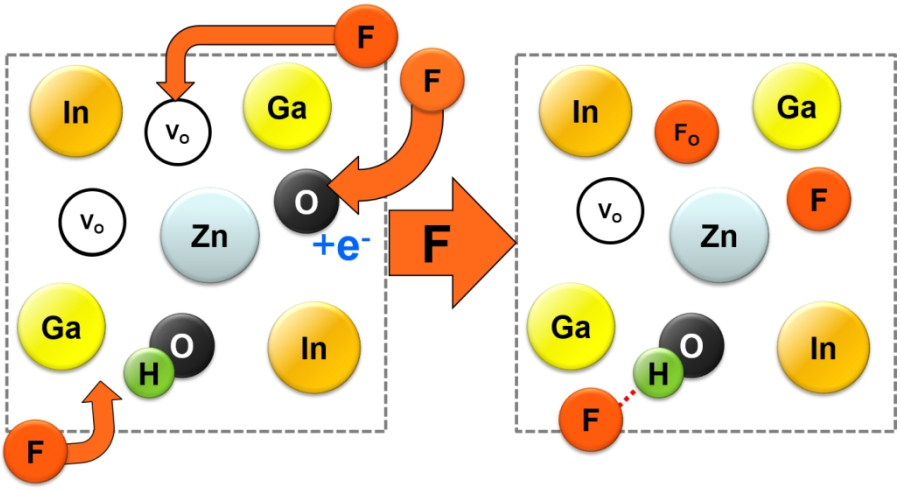

Fig. 3.9 Mechanism of fluorine incorporation in *a*-IGZO showing how F can occupy the V_O to form F_O, substitute the O site, and form strong secondary bonds with H to neutralize the OH.

Aside from the two mechanisms described in eqs. (3.1) and (3.2), F can form a strong hydrogen bond with OH to further passivate this trap site [37]. Furthermore, because of the strong hydrogen bond between the F and OH, the OH is stabilized so that the H ion cannot easily dissociate during stress. This is why P-PSQ passivated TFTs which contained F did not exhibit hump effect while both NP-PSQ and unpassivated TFTs which did not contain F exhibited hump effect during stress, especially NBS. Furthermore, F has preferential bonding with Zn compared with other metals in *a*-IGZO to form a more stable Zn-F bond [37]. From eq. (3.1), the F substitution in the O site stabilizes the weakly bonded oxygen leading to better stability. This is because weakly bonded oxygen is also a source of V_O since the weakly bonded oxygen can dissociate and form a V_O. In addition, because of the difference in electronegativity between O and F, an extra electron is generated during this substitution process. This increases the electron concentration leading to mobility enhancement and V_{th} reduction in P-PSQ TFTs as

shown in table 3.III. However, a very high amount of F can lead to a very substantial increase in electron concentration which can degrade the performance of *a*-IGZO TFTs [40]. Therefore, like in the case of H, it is also important to control the amount of F in *a*-IGZO. Reaction (3.2) shows that like H, F can occupy the V_O site. Naturally, the decrease in V_O which are trap sites further improves the reliability of the P-PSQ TFT. This is reflected in the impressive stability of P-PSQ against stress as shown in Fig 3.3. Comparing eq. (3.1) and (3.2), it can be deduced that the two reactions are competing mechanisms with regard to electron concentration. The substitution of O by F (reaction 1) generates more electrons while occupation of V_O by F (reaction 2) reduces the electron concentration. From table 3.III, there was an increase in mobility from 14.10 cm^2/Vs to 17.07 cm^2/Vs and decrease in V_{th} from 3.68 V to 2.5 V after P-PSQ passivation which suggests that reaction (3.1) is a more dominant mechanism. However, since V_{th} reduction is not very drastic, reaction (3.1) is only slightly more dominant than reaction (3.2). Nevertheless, the enhancement of electrical properties, excellent stability, and suppressed hump effect show that all three F mechanisms are present in the case of P-PSQ TFT.

3.5 Summary

The need for the development of techniques to prevent process damage in *a*-IGZO is discussed in this chapter. The effects of processes that can damage *a*-IGZO (such as dry etching) are explained. NP-PSQ TFTs are shown to be affected by RIE during the formation of contact holes. Transfer curves after RIE showed a large negative V_{th} shift, worse *S*, degradation in the subthreshold region, and worse uniformity, while showing an enhanced mobility. A post-annealing process in O_2 is shown to be effective in partially recovering the initial characteristics of the TFT.

P-PSQ passivation is introduced as an alternative to NP-PSQ and other passivation layers that require etching. Aside from further simplifying the simple fabrication of NP-PSQ, the P-PSQ fabrication process also ensures that processes that are sources of process damage such as dry etching and resist stripping are not omitted. Aside from the simple fabrication, large improvement in electrical characteristics of P-PSQ passivated *a*-IGZO TFTs is observed. Bias stress testing (PBS, NBS, and NBIS) also highlights the reveal the excellent reliability of P-PSQ *a*-IGZO TFTs similar to NP-PSQ. Humidity stress also confirms the excellent barrier ability of P-PSQ. Furthermore, P-PSQ did not show hump effect during PBS and NBS unlike in the case of NP-PSQ.

Reliability mechanisms and the problem of hump effect are discussed in section 3.4. SIMS measurements show a high concentration of C and H in the *a*-IGZO channel after passivation. SIMS also shows that humidity has minimal effect on the elemental composition of P-PSQ TFTs further supporting the excellent barrier ability of P-PSQ. In addition, SIMS analysis shows a high amount of F in the *a*-IGZO layer of P-PSQ. F is shown to behave similar to H wherein it occupies the V_O leading to reduction of trap sites. Furthermore, F is shown to stabilize the weakly bonded oxygen by substituting the weak O and forming a stronger Zn-F bond. The mechanism of hump effect is explained and it was shown to be due to the dissociation of H ions from the weak OH bonds. These mobile hydrogen ions and other positive charges can drift towards the source/drain-backchannel interface and case an early turn-on of the TFT because of their relatively near location to the drain. F is shown to stabilize these weak OH bonds by forming strong secondary bonds with OH, thus preventing H from easily dissociating during stress. These results show the great promise of P-PSQ in enhancing the electrical characteristics and stability of *a*-IGZO TFTs for application in more advanced purposes.

References

[1], S. Kim, C.Kim, S.Kim, I.Song, H.Yin, K.K Kim, S. Lee, K. Hong, J. Lee, J. Jung, E. Lee, K.-W. Kwon and Y. Park, Appl. Phys. Lett. **93**, (2008) 053505.

[2] J. Park, I. Song, S. Kim, S. Kim, C. Kim, J. Lee, H. Lee, E. Lee, H. Yin, K.-K. Kim, K.-W. Kwon and Y. Park, Appl. Phys. Lett. **93**, (2008) 053501.

[3] T. Kamiya, K. Nomura, and H. Hosono, Sci. Technol. Adv. Mater., **11**, (2010) 044305.

[4] R. Zhan, C. Dong, P.-T. Liu, H.-P. Shieh, Microelectronics Reliability, **53**, (2013) 1879.

[5] T. Matsuda, D. Nishimoto, K. Takahashi, and M. Kimura, Jpn J. Appl. Phys. **53**, (2014) 03BCB03.

[6] J. Y. Kwon, D.-J. Lee, and K.-B Kim, Electronic Materials Lett., **7**, (2011) 1.

[7] R. L. Hoffman, B. J. Norris, and J. F. Wager, Appl. Phys. Lett. **82**, 733 (2003).

[8] H. Q. Chiang, J. F. Wager, R. L. Hoffman, J. Jeong, and D. A. Keszler, Appl. Phys. Lett. **86**, 013503 (2005).

[9] J. I. Song, J. S. Park, H. Kim, Y. W. Heo, G. M. Kim, and B. D. Choi, Appl. Phys. Lett. **90**, (2007) 022106.

[10] E. M. C. Fortunato, P. M. C. Barquinha, A. C. M. B. G. Pimental, A. M. F. Goncalves, A. J. S. Marques, L. M. N. Pereira, and R. F. P. Martins, Adv. Mater. (Weinheim, Ger.) **17**, (2005) 590.

[11] M.Kim, J. H. Jeong, H. J. Lee, T. K. Ahn, H. S. Shin, J. S. Park, J. K. Jeong, Y. G. Mo, and H. D. Kim, Appl. Phys. Lett., **90**, (2007) 212114.

[12] M. Mativenga, J. W. Choi, J. H. Hur, H. J. Kim, and J. Jang, J. Inf. Disp., **12**, (2011) 47.

[13] R. Zhan, C. Dong, B.-R, Yang, and H.-P. Shieh, Jpn J. Appl. Phys. **52,** (2013) 090205

[14] Q. Yuan, G. Yin, and N. Zhaoyuan, Plasma Sci. and Technol. **15** (2013) 86.

[15] W. Flack, G. Flores, L. Christensen, and G. Newman, Proc. SPIE, **2726**, Optical Microlithography IX, (1996) 169.

[16] A. Tanabe, M. Hanmura, T. Katoh, H. Oomori, A. Honma, and T. Suzuki, IEICI Trans. Electron., **E95-C**, (2012) 1737.

[17] T. Hamada, T. Nagase, T. Kobayashi, K. Matsukawa, and H. Naito, Thin Solid Films, **517**, (2008), 1335.

[18] T. Hamada, S. Yamazaki, T. Nagase, K. Tomatsu, Y. Ueda, M. Watanabe, S. Watase, T. Tamai, T. Kobayashi, S. Murakami, H. Naito, and K. Matsukawa, Proc. of the 15th International Display Workshops, (2008), 1665.

[19] Y. Kusaka, S. Nakamura, K. Azuma, T. Sasaki, T. Unate, Y. Nakatani, A. Nakasuga, K. Matsukawa, N. Watanabe, H. Naito, and H. Kaji, Jpn. J. Appl. Phys., **47**, (2008) 1377.

[20] S. Jeong, D. Kim, S. Lee, B. K. Park, and J. Moon, Nanotechnology, **18**, (2007) 025204.

[21] T. Hamada, T. Nagase, M. Watanabe, S. Watase, H. Naito, and K. Matsukawa, J. Photopolym. Sci. Technol., **21**, (2008) 319.

[22] Z. Bao, V. Kuck, J. A. Rogers, and m. A. Paczkowski, Adv. Func. Mater., **12**, (2002) 526.

[23] J. Wang, X. Yan, Y. Xu, J. Zhang, and. D. Yan, Appl. Phys. Lett., **85**, (2004), 5424.

[24] P. Liu, Y. Wu, Y. Li, B. S. Ong, and S. Zhu, J. Am. Chem. Soc., **128**, (2006), 4554.

[25] Y. Wu, P. Lin, and B. S. Ong, Appl. Phys. Lett., vol. 89, no. 1, Article ID 013505, 2006.

[26] M. Watanabe, K. Muro, T. Hamada, T. Tamai, A. Masuyama, H. Naito, K. Matsukawa., Chem. Lett., **38**, (2009) 34.

[27] K. Nomura, T. Kamiya, and H. Hosono, Thin Solid Films, **520**, (2012) 3778.

[28] S.-H. Choi, J.-H. Jang, K. Jang-Joo, and M.-K. Han, IEEE Elect. Dev. Lett., **33**, (2012) 381.

[29] G.-W. Chang, T.-C. Chang, Y.-E. Syu, T.-M. Tsai, K.-C. Chang, C.-H. Tu, F.-Y. Jian, Y.-C. Hung, Y.-H. Tai, Thin Solid Films, **520**, (2011) 1608.

[30] W. J. Kim, C. S. Kim, S. J. Jo, H. S. Hwang, S. Y. Ryu, and H. K. Baik, Semicon. Sci. and Tech. **23**, (2008) 075034.

[31] S.-J. Seo, S. C. Yang, J.-H. ko, and B.-S. Bae, Electrochem. and Solid Stat. and Lett., **14**, (2011) H375.

[32] R. H. Barney, M. Itoh, A. Sakakibara, and T. Suzuki, Chem. Rev., **95**, (1995) 1409.

[33] B. Ryu, H.-K. Noh, E.-A. Choi, and K. J. Chang, Appl. Phys. Lett., **97**, (2010) 022108.

[34] M. D. H. Chowdhury, P. Migliorato, and J. Jang, Appl. Phys. Lett., **97**, (2010) 173506.

[35] K.-H. Liu, T.-C. Chang, K.-C. Chang, T.-M. Tsai, T.-Y. Hsieh, M.-C. Chen, B.-L. Yeh and W.-C. Chou, Appl. Phys. Lett. **104**, (2014) 103501.

[36] M. Mativenga, M. Seok and J. Jang, Appl. Phys. Lett. **99**, (2011) 122107.

[37] J.-S. Seo, J.-H. Jeon, Y. H. Hwang, H. Park, M. Ryu, S.-H. K. Park, and B.-S. Bae, Sci. Rep. **3**, (2013) 2085.

[38] H. Yamazaki, Y. Ishikawa, M. Fujii, Y. Ueoka, M. Fujiwara, E. Takahashi, Y. Andoh, N. Maejima, H. Matsui, F. Matsui, H. Daimon, and Y. Uraoka, ECS J. Solid Stat. Sci. Technol. **3**, (2014) Q20.

[39] J. Jiang, T. Toda, M. P. Hung, D. Wang, and M. Furuta, App. Phys. Exp. 7, (2014) 114103.

[40] L. X. Qian, W. M. Tang and P. T. Lai, ECS Solid State Lett., **3**, (2014) P87.

Chapter 4

Analysis of Low Temperature Excimer Laser Annealing of *a*-IGZO TFT for flexible displays

4.1 Introduction

One desired feature of *a*-IGZO and other oxide semiconductors is its low temperature processability since these can be usually deposited at room temperature. Combined with its transparency, both features open the door for more advanced applications in transparent flexible displays and electronics [1-4]. Flexible electronics and circuits based on *a*-IGZO have already been demonstrated [5-7] paving the way for future ubiquitous and wearable applications. Nevertheless, annealing up to 400 ^{o}C is often required after deposition because un-annealed *a*-IGZO have inferior electrical characteristics and poor stability [8-11]. This high temperature annealing is not compatible with most flexible substrates and thus developing an annealing method with a lower temperature or a method that ensures localization of heating far from the substrate is required.

The reasons why annealing are necessary are discussed in section 4.2. Currently, there are many conventional annealing methods available and these are enumerated in this section. The effects and influence of these conventional annealing methods on *a*-IGZO are also examined. In addition, the arguments for the necessity of lowering the process temperature are also given. Emerging alternative low temperature annealing methods are presented and their advantages and disadvantages over conventional annealing methods are discussed.

In section 4.3, excimer laser annealing (ELA) is introduced as an alternative annealing process which induces no thermal damage to the substrate and its advantages over other annealing methods are discussed. Two types of ELA are presented: XeCl ELA in section 4.4 and the shorter wavelength KrF ELA in section 4.5. Heat transfer analysis by COMSOL Multiphysics simulation (2D heat transfer simulation) is performed to analyze the temperature induced by the laser. This is also to verify whether the local temperature at the substrate layer is low. Furthermore, 2D heat simulation enables identification of critical and susceptible areas where potential degradation may occur during ELA. SIMS analysis, XPS, X-ray diffraction (XRD), and X-ray reflectometry (XRR) are performed to analyze the effects of ELA on *a*-IGZO such as changes in chemical composition, chemical bonding and structure. These results are discussed in section 4.6. Understanding the effects of ELA on the electrical characteristics and properties of *a*-IGZO is crucial in developing low temperature processed *a*-IGZO with superb performance for flexible applications. Furthermore, capitalizing on the selective nature of ELA will enable fabrication of more advanced high speed devices such as self-aligned *a*-IGZO TFTs.

4.2 Why annealing is necessary

4.2.1 Conventional annealing methods

Annealing is an essential method in the fabrication of *a*-IGZO TFTs to ensure superior electrical properties and stability. Annealing reduces the trap density in *a*-IGZO leading to better stability [12]. Stability enhancement in annealed *a*-IGZO is also observed because annealing oxidizes *a*-IGZO – reducing native donor defects and

removing weak chemical bonds such as Zn-O [8]. As previously explained, these weak chemical bonds are especially problematic since they can cause hump effect (in the case of weak OH) and generate V_O (in the case of weak oxygen bonds from Zn-O).

Fabricating oxide TFTs by solution process is also important in the realization of large area flexible electronics especially in the advancement of printed electronics. Many researchers have introduced various methods such as spin-coating and spray pyrolysis to deposit oxide semiconductors by solution process [13-16]. However, annealing up to 400 ^oC is especially crucial for solution processed oxide TFTs since elevated temperatures are required to evaporate/decompose the precursor solution and complete the reaction to form a more uniform oxide film [3, 17].

Numerous annealing methods have been developed to efficiently carry out the temperature treatment. Conventional methods are based on furnace annealing or straightforward heating on a hotplate. These methods are effective in annealing oxide semiconductors and are much preferred because of their simplicity and ease of use. In addition, especially in the case of furnace annealing, it is very easy to control the ambient conditions such as gas ratio, pressure, and temperature ramp, during annealing. However, the disadvantage of these methods is that heating is not selective. In this case, whatever temperature is set will be applied to all layers in the samples. This is not ideal since in most cases, the substrate and the insulator do not need high temperature annealing. It also limits the type of substrates that can be used.

Other annealing methods also exist usually as a variation of furnace annealing by changing the ambient conditions. These methods are high pressure oxygen annealing [18], high pressure vapor annealing [19], and wet O_2 annealing [8]. High pressure oxygen annealing can reduce the amount of V_O and also reduce the free electron carrier density

[18]. Reducing the V_O amount will naturally improve the stability, especially during NBIS, since photo-induced electron concentration will also be reduced. High pressure water vapor (HPV) annealing increases the μ of the TFT because of the H and O related species that are introduced during the annealing [19]. However, hump effect is observed in some cases of HPV and the paper attributed this to the increased roughness at the backchannel due to the high pressure [19]. Wet O_2 annealing has also been shown to be more effective than dry O_2 annealing in improving the performance of *a*-IGZO TFTs [8]. Wet O_2 annealing effectively reduces electron traps because of the stronger oxidation power of H_2O related species leading to more stable bonds and homogenized *a*-IGZO TFTs. Nevertheless, while effective, these previous methods are still carried out at high temperatures of up to 400 ^oC and more importantly, in a non-selective manner.

4.2.2 Low temperature annealing alternatives

Much research has been devoted to reduce the annealing temperature of *a*-IGZO TFTs. For solution processed *a*-IGZO TFTs which typically needs annealing upwards of 400 ^oC, researchers have been able to reduce the annealing temperature to a lower temperature of 300 ^oC by spray-combustion [20]. Note that in solution process, 300 ^oC is already considered a low temperature process. With this process, solution process *a*-IGZO TFTs were fabricated with μ reaching 10 cm^2/Vs which is comparable to most *a*-IGZO TFTs fabricated by vacuum process [20]. At temperatures of 300 ^oC, choices for flexible substrates are still limited. Flexible substrates that are applicable to *a*-IGZO based devices for flexible electronics are: Polyimide (PI, process temperature up to 350 ^oC), Polyetheretherketone (PEEK, 143 – 260 ^oC), Polyethylene naphtalate (PEN, 120 -200 ^oC), and Polyethylene terephthalate (PET, 78 – 150 ^oC) [21]. PI on

Polydimethylsiloxane (PDMS) has also been used as a flexible substrate even at a process temperature of 300 ºC [7]. Fabrication of *a*-IGZO on paper has also been demonstrated [3, 22], although process temperature should be as low as possible. As seen from the previous lists, more materials for flexible applications become available as the process temperature is decreased.

Methods to lower temperature have been presented by other researchers. This usually involves using special precursors that can be processed at lower temperatures. For instance, solution process oxide TFTs were processed with temperatures as low as 230 ºC by employing a sol-gel hydrolysis approach on metal alkoxide precursors [23]. Combustion processing/synthesis have also been introduced to lower temperature by optimizing the metal oxide precursors such that they generate heat during reaction because of their exothermic nature [24, 25]. In this way, there is no need for an external source of energy since the precursors will be their own energy source and thus, the heating is localized [24]. Other methods have also been used to dramatically reduce the processing temperature to 150 ºC [26-28]. By tuning the metal precursors and employing additives and solvents that can be decomposed by deep ultraviolet irradiation (DUV), high performance oxide devices were fabricated by simple photochemical activation through DUV [27]. The use of a XeCl UV lamp irradiation or solid state laser has also been shown to limit the process temperature at 150 ºC [28]. Microwave annealing has also been shown to be effective in lowering the temperature to as low as ~87 ºC and localizing heat away from the substrate [29, 30]. Although reported μ were lower than 10 cm^2/Vs [29, 30].

4.3 Excimer laser annealing

Laser annealing has been demonstrated as an annealing alternative to thermal annealing [31]. Laser annealing is strictly not a low temperature process because it induces high temperatures at the site of impact depending on the laser fluence and laser source used. However, this high temperature can be localized and confined at a specific area far from the substrate by tuning the fluence energy, using appropriate laser sources and utilizing proper materials and thicknesses. ELA is a popular annealing method and is regarded as a low temperature annealing alternative because the local temperature at the substrate can be very low. The application of ELA on poly-Si TFTs is prevalent [32-34]. It is also used in hydrogenated amorphous silicon (*a*-Si:H) [35]. The most important function of ELA is in the crystallization of *a*-Si or the enlargement of the grain size [34]. Of particular interest are the several growth mechanisms during ELA in Si. Several groups have already studied this by analyzing the lateral grain growth of poly-Si during ELA [36] and analyzing the phase transformation mechanism [37]. The compatibility of ELA for flexible substrates has also been demonstrated by successfully using ELA to crystallize and dope Si on plastic substrates [38].

ELA has also been successfully used in oxide semiconductors such as *a*-IZO TFT [39], sol-gel ZnO [40], solution processed *a*-IGZO [41], and *a*-IGZO TFTs [42-46]. By utilizing ELA, a temperature of up to 1500 ^{o}C can be induced in *a*-IGZO at typical fluence energies (such as 150 mJ/cm^2), while maintaining very low temperatures at the flexible substrates well below 50 ^{o}C [43]. This is due to the much lower absorption coefficient of typical flexible substrates compared to *a*-IGZO. Moreover, SiO_2 with a thickness of ~100nm can act as a buffer layer to suppress thermal damage on the substrate [43]. Another advantage of ELA in oxide TFTs compared to when applied to Si-based

TFTs is that penetration depth in oxides is deeper compared to Si. A laser penetration depth of 70 nm is possible for *a*-IGZO while only 6 nm is possible for Si [45]. This implies that *a*-IGZO will be more uniformly annealed so that it will have a more uniform structure compared to Si which will have a layered structure after annealing. Another feature of ELA is location control. By capitalizing on this feature, more advanced applications of ELA can be realized on *a*-IGZO TFTs such as in developing self-aligned TFTs. This is because the amount of V_O in *a*-IGZO can be controlled by excimer laser irradiation. Thus, by selectively applying ELA on a section of *a*-IGZO film, the conductivity of the section exposed to ELA will have higher conductivity (more V_O) compared to the unexposed regions. This technology has been demonstrated by backside excimer laser irradiation of bottom-gate *a*-IGZO to obtain self-aligned *a*-IGZO with less parasitic capacitance because the higher conductivity *a*-IGZO is overlapped with the source and drain regions [46]. Therefore, high-speed devices can be fabricated through the ELA self-align process.

Nevertheless, previous reports of ELA on oxide TFTs are largely unpassivated. As shown before, a passivation is mandatory to protect the sensitive backchannel of *a*-IGZO. In this study, *a*-IGZO TFTs were passivated with NP-PSQ passivation layers and were subjected to ELA by either XeCl ELA or KrF ELA. These two types of ELA were used because of their excellent penetration depth in *a*-IGZO. Testing multiple laser wavelengths also allows more variation in the fluence energy and heating that can be induced on *a*-IGZO. The effects of both types of ELA on the properties and electrical characteristics were examined and analyzed. Simulation was also performed to analyze the heating localization, identify possible degradation regions and check if substrate temperature is low.

4.4 XeCl ELA

4.4.1 Device fabrication

The fabricated TFTs are similar to the TFTs fabricated in chapter 2. SPM-cleaned heavily doped n-type Si (resistivity < 0.002 Ω·cm) with a 100 nm thermally oxidized SiO_2 was utilized as the gate and gate insulator materials, respectively. A 70 nm thick *a*-IGZO layer is deposited by RF magnetron sputtering deposition at room temperature with an oxygen and argon gas ratio of 4.5%. The 70 nm thickness is especially important since this is the penetration depth of ELA in *a*-IGZO. The *a*-IGZO were then patterned by UV photolithography and etched by 0.02 mol/L HCl to form the *a*-IGZO islands. A stack of 80 nm thick Mo and 20 nm thick Pt were used as the source and drain by using RF magnetron sputtering deposition and patterning using the lift off technique. Unlike in chapter 2, the TFTs were not subjected to 300 ^oC AT annealing.

For *a*-IGZO TFTs that will be subjected to XeCl ELA, Me 100 was used as the passivation material. Me 100 was first spin-coated on the *a*-IGZO TFT at a main spin rate of 3000 rpm for 15 s. A 2 step heat treatment was then performed on a hot plate to complete the passivation process: first, prebaking at a temperature of 130 ^oC for 90 s was performed to evaporate the solvent and finally, post-baking at 300 ^oC for 1 hour in ambient atmosphere was done to cure the passivation material. RIE with a CF_4/O_2/Ar gas mixture was also performed to form the contact holes. Again, unlike the process in chapter 2, the TFTs that were subjected to dry etching and which will be irradiated by XeCl ELA were not subjected to the customary 300 ^oC O_2 annealing.

The fabricated Me 100 passivated *a*-IGZO TFTs were then subjected to ELA by irradiating these with one shot of XeCl ELA under N_2 ambient atmosphere at room

temperature. The wavelength and pulse width at full width half max (FWHM) were 308 nm and 25 ns, respectively. The samples were irradiated at a set fluence energy per shot by scanning the substrate with the XeCl laser ensuring that only a single shot hits the TFT. The beam size *W/L* is 0.1/0.1 cm ensuring that the beam size is much larger than a single TFT (TFT dimensions are at maximum only ~100 microns). Fig 4.1 is a schematic showing the ELA irradiation of a-IGZO TFT passivated by PSQ. Note that Me 100 is completely transparent at 308 nm (see Fig. 2.3) so that ELA is expected to pass through it and completely irradiate and anneal the *a*-IGZO.

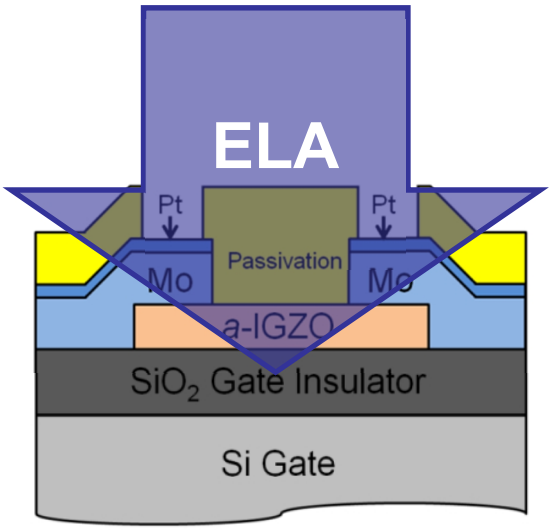

Fig 4.1 Schematic of ELA irradiation on *a*-IGZO TFT already passivated by PSQ.

4.4.2 Electrical characteristics

The effects of XeCl ELA on the electrical characteristics of *a*-IGZO were analyzed. Electrical characteristics were measured before XeCl ELA (After passivation and etching) and after XeCl ELA. Measured TFTs had a *W/L* of 90/10 μm. Fig. 4.2 shows a comparison of the transfer characteristics of Me 100 passivated *a*-IGZO TFTs before and after XeCl ELA with fluence energies of 90 and 110 mJ/cm^2. Before XeCl ELA, the

transfer characteristics show degradation in the subthreshold region and very high off current. This is despite the fact that *a*-IGZO was already subjected to 300 ^{o}C for 1h because of the heat treatment on the hot plate needed to fabricate the Me 100 passivation layer. Subjecting the passivated TFTs to XeCl ELA from 90 to 110 mJ/cm^2 dramatically improved the electrical characteristics. There is no longer any degradation in the subthreshold region and the off current is severely reduced. The measured saturation μ is ~ 12.5 cm^2/Vs and V_{th} is ~ 3V. The V_{gs} at 1 nA is also close to 0 V. These electrical characteristics are very much comparable to the electrical characteristics observed in furnace annealed samples. XeCl ELA also shows a wide window that can be considered as a good process condition, although the subthreshold is less steep at higher fluence energy. Note that the TFTs subjected to XeCl ELA were not subjected to AT annealing after *a*-IGZO and source/drain deposition and O_2 annealing after dry etching. This implies that XeCl ELA was able to replace these two annealing steps, further simplifying the process. ELA performed contact annealing of the *a*-IGZO film and the source/drain electrodes (typically performed by AT annealing) and reversed any damage caused by dry etching (typically performed by O_2 annealing). Nevertheless, slight degradation is observed in the saturation region due to the possible formation of Molybdenum oxide because of the very high temperature during ELA at this interface (see section 4.4.3). This oxide formation possibly caused a higher contact resistance between the *a*-IGZO and electrode.

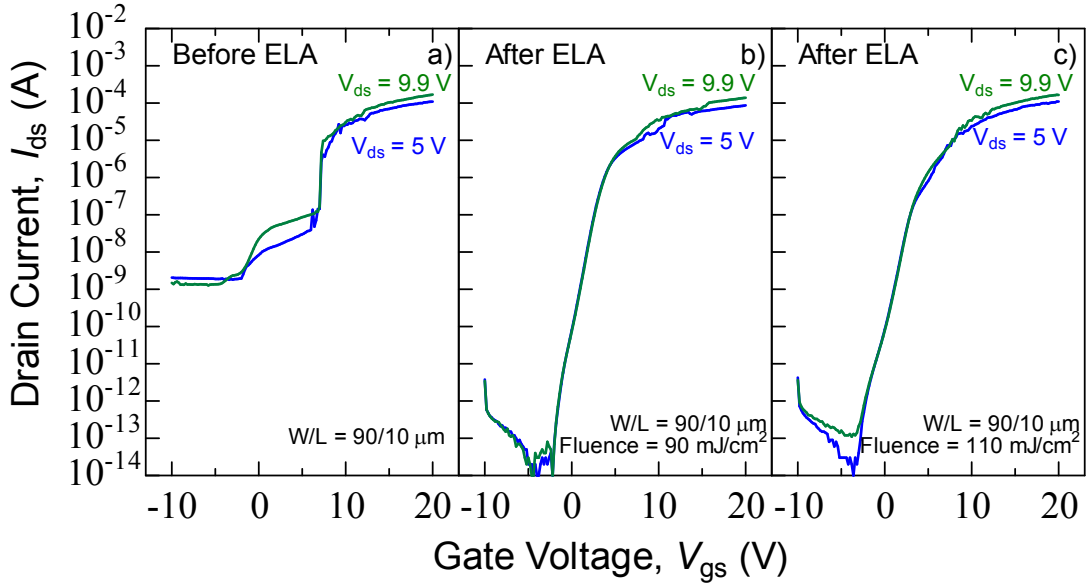

Fig 4.2 Comparison of transfer characteristics of Me 100 passivated *a*-IGZO TFT a) before ELA, b) XeCl ELA at 90 mJ/cm^2, and c) XeCl ELA at 110 mJ/cm^2. TFTs had a *W/L* = 90/10 μm.

The dependency of ELA on the TFT dimensions is also examined. Fig. 4.3 compares the transfer curves of Me 100 *a*-IGZO TFTs irradiated by XeCl ELA at 90 mJ/cm^2 with varying *L* while Fig 4.4 are the variation in transfer curves of Me 100 *a*-IGZO TFTs irradiated by XeCl ELA at 110 mJ/cm^2 with varying *W*. Clear transistor switching operation is observed in all cases. In addition, no hump effect is observed for all the transfer curves, although slight degradation is again observed in the saturation region. Varying the length up to a small channel length of 5 μm does not greatly degrade the TFT. In fact, even at a small channel length of 5 μm, clear transistor operation is achieved although the off-current slightly increased and the subthreshold became less steep. A different scenario is observed when varying the width. Significantly decreasing the width from 90 to 10 μm has little on effect the switching property of the TFT, although there is a slight decrease in the on-current and slight increase in the off-current. However, reducing

the width even further by 50% from 10 to 5 μm leads to severe deterioration of the electrical characteristics. Both the off current and on current deteriorated, the off-current increased significantly while the on-current decreased. Degradation in the subthreshold is also observed at smaller widths. The cause of this degradation is due to the very small dimensions of both the *W/L* leading to a higher heating temperature at the source/drain-channel interface. The 2D heat simulation in the next section will explain this mechanism in more detail.

Fig 4.5 summarizes the changes in on/off ratio as the *W* and *L*. There is only little change in the on/off ratio from ~ 6.75 x 10^9 to 5.86 x 10^8 when the *L* is decreased from 15 to 5 μm. An on/off ratio in the order of 10^8 is still considered impressive. On the other hand, decreasing the *W* from 90 to 5 μm lead to substantial degradation of the on/off ratio from ~1.10 x 10^{10} to 4.41 x 10^3 – a decrease in almost 7 orders of magnitude. The on/off ratio decreased only by 2 orders of magnitude to ~ 1.11 x 10^8 when the *W* was reduced to 10 μm from 90 μm. Again, this on/off ratio is still very good and is observed in many oxide TFTs. These results show that ELA can be applied to TFTs at even small dimensions, but different ELA conditions are needed once the dimensions of the TFTs become very small.

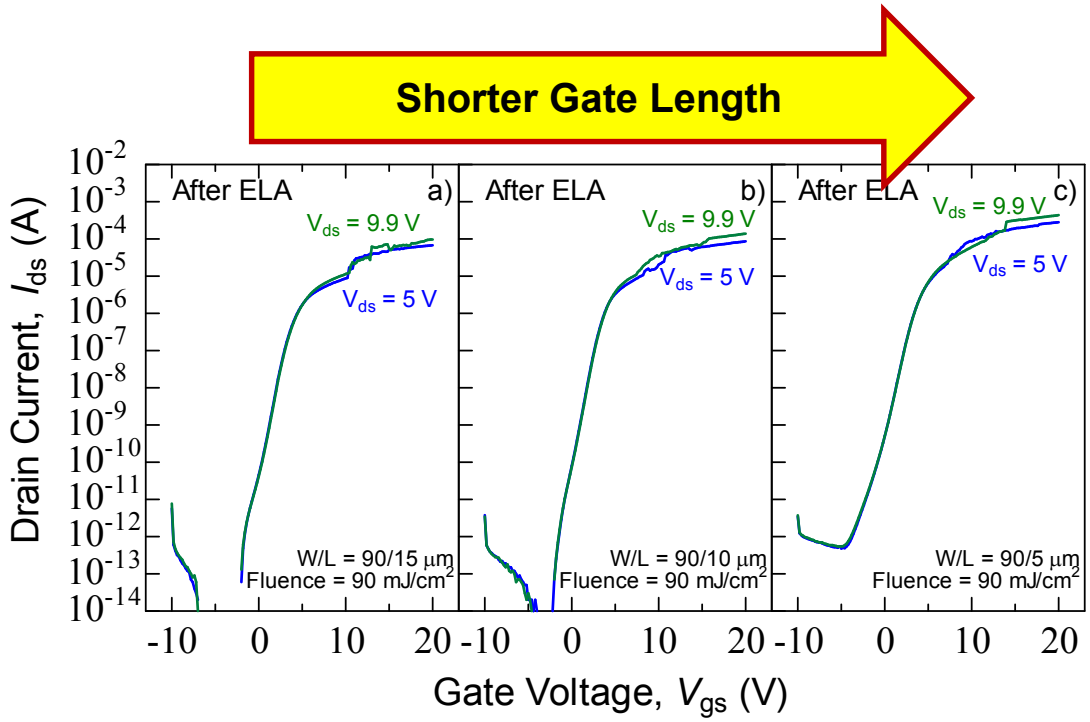

Fig 4.3 Comparison of transfer characteristics of Me 100 passivated *a*-IGZO TFT subjected to XeCl ELA at 90 mJ/cm^2 at varying *L* of a) 15 μm b) 10 μm, and c) 5 μm. TFTs had a constant *W* of 90 μm.

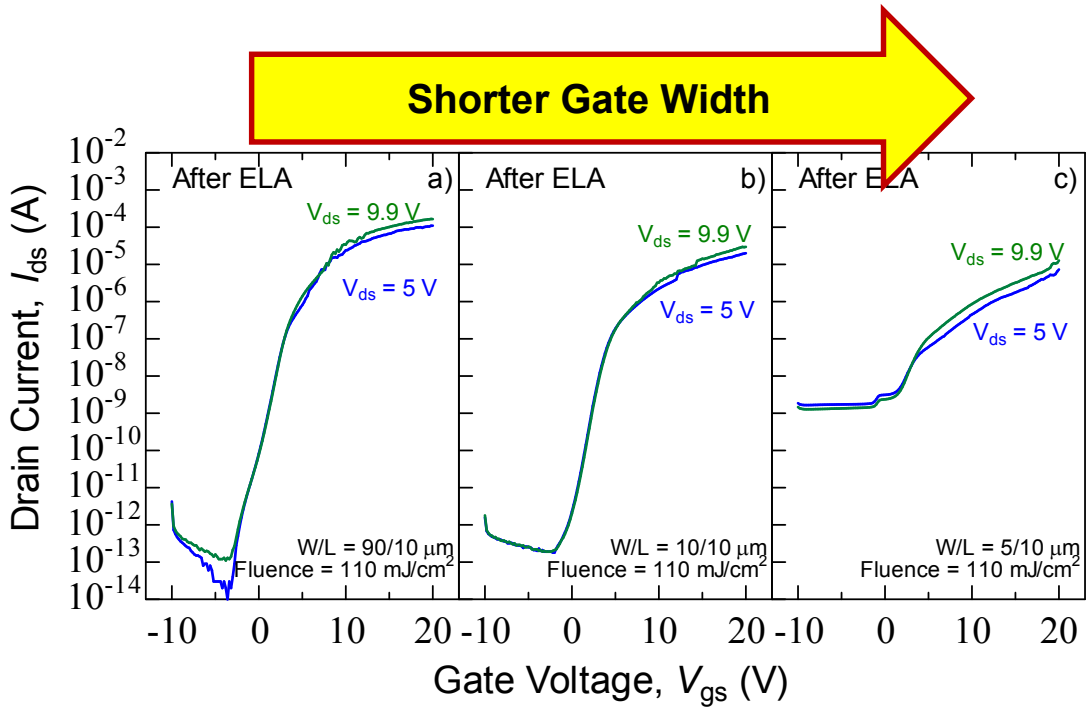

Fig 4.4 Comparison of transfer characteristics of Me 100 passivated *a*-IGZO TFT subjected to XeCl ELA at 110 mJ/cm^2 at varying *W* of a) 90 μm b) 10 μm, and c) 5 μm. TFTs had a constant *L* of 10 μm.

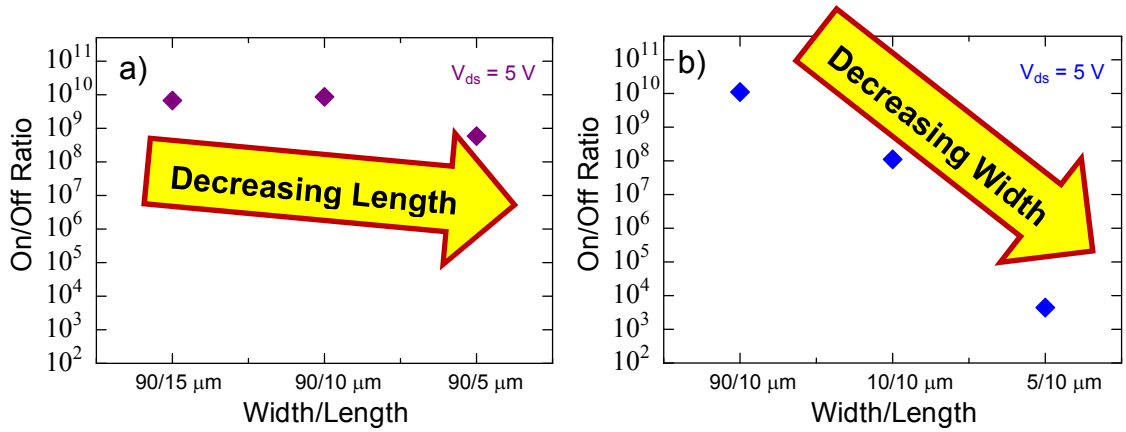

Fig 4.5 Summary of the variation of on/off current of Me 100 passivated *a*-IGZO TFT subjected to XeCl ELA with varying a) *L* and b) *W*.

4.4.3 COMSOL Multiphysics simulation

The degradation phenomena related to the dimension of the TFT that was observed in the earlier section can be more clearly understood if 2D heat simulation is performed. Similar to other laser heating simulation performed on Si [47], COMSOL Multiphysics is used to perform this simulation. The simulation is based on the time-dependent heat equation as shown in equation (4.1).

$$\rho C_p \frac{\partial}{\partial} + \rho C_p \mathbf{u} \cdot \nabla \quad = \nabla \cdot (k \nabla T) + Q \qquad (4.1)$$

In this equation, ρ is the density, C_p is the specific heat capacity at constant pressure, T is absolute temperature, t is time, $\mathbf{u}$ is the velocity vector of heat flow, k is the thermal conductivity, and Q are the other heat sources, in this case, it is the laser heat source. Since the Me 100 passivation is completely transparent at 308 nm, it is expected that the laser will penetrate through Me 100 and irradiate the Pt and *a*-IGZO. The light that passes through the Me 100 can be determined by equation (4.2), which is

the equation for reflectivity, R.

$$R = \left[\frac{n_2 - n_1}{n_2 + n_1}\right]^2 \qquad (4.2)$$

Reflectivity is dependent on the refractive index of the material, in this case, Me 100 and the first surface which is air. The refractive index of Me 100 is 1.35 which means that around 95.6% of the laser eventually propagates through Me100 and into the top surfaces such as *a*-IGZO and Pt. Note that the laser is reflected twice: first at the air-Me 100 interface and finally at the Me 100-Pt or Me 100-*a*-IGZO interface depending on location. It is also important to note that the laser dimension is much larger than the size of the TFT so that the TFT is fully irradiated by the laser at a uniform fluence.

In the 2D heat transfer simulation, Pt and *a*-IGZO are considered as heat sources since they are directly irradiated by the laser. From equation (4.1), the heat equation includes Q which is the heat due to the laser source and this is a function of time. Note that for the other layers in the TFT, Q = 0 since they are not directly irradiated by the laser and the temperature increase is primarily due to heat transfer from the top layers. Equation (4.3) shows the equation for the heat from the laser source, Q(t) .

$$Q(t) = E(1 - R)(p(t))(\alpha e^{\alpha}) \qquad (4.3)$$

E is the fluence energy of the laser, R is the reflectivity of the material, $p(t)$ is the laser pulse as a function of time, α is the absorption coefficient (at 308 nm), and x is the position/depth. Ellipsometry (Woollam M2000 Ellipsometer) was used to measure the optical constants of *a*-IGZO at 308 nm. The measured α of *a*-IGZO at 308 nm is 1.128 x

10^5 1/cm. R of *a*-IGZO is 0.098 while R of Pt is 0.47. The α of Pt is 9.138 x 10^5 1/cm. Other parameters and the laser pulse, p(t), are shown in the appendix section.

Fig 4.6 shows the results of the 2D laser heat simulation. From the inset figure of the TFT, it is evident that there is spatial variation of temperature in the *a*-IGZO channel layer. The highest temperatures are located near the source/drain-channel interface. This explains why at very small TFT dimensions, there is higher degradation in the electrical characteristics. Having smaller *W/L* dimensions implies higher heating temperature concentrations at this interface. Therefore, selecting appropriate fluence energies when annealing TFTs with smaller dimensions can be easily done if one performs 2D heat simulations. Furthermore, selecting appropriate electrodes is important because of higher temperatures up to ~1600 ºC at this interface. For instance, the choice of Mo and Pt as electrodes is good because of their high melting points of ~2600 ºC and ~1750 ºC, respectively. On the contrary, Au as electrode (melting point: ~ 1050 ºC) is a poor choice. The similarity in the coefficient of thermal expansion of Mo and *a*-IGZO which is both ~ 5 x 10^{-6}/K means that large distortions or delamination during heating will be avoided or minimized. If an electrode with a significantly different coefficient of thermal expansion was instead used, there will be mechanical damage and distortion at the channel and electrode interface since the rate of expansion during laser heating will be different leading to possible delamination.

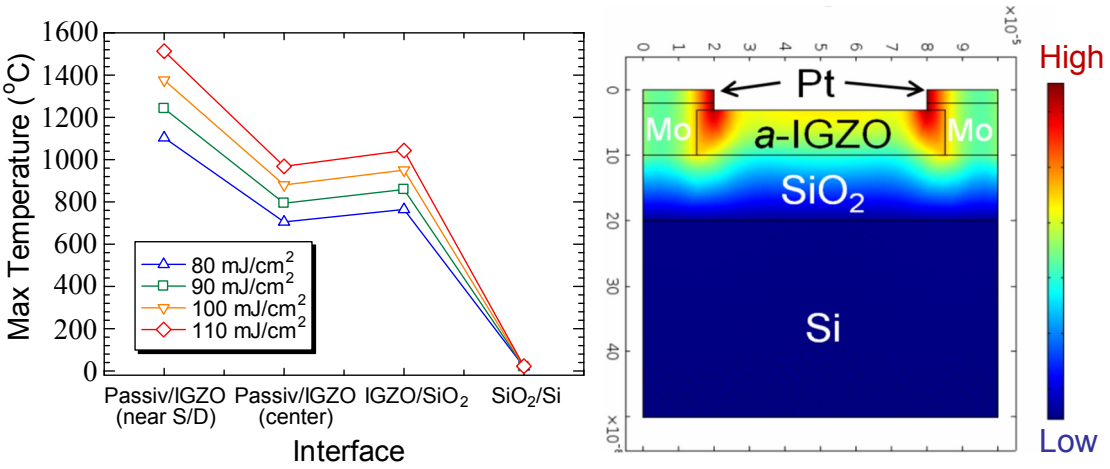

Fig 4.6 COMSOL Multiphysics Simulation of laser heating (2D heat transfer) of Me 100 showing the maximum temperature during the whole laser heating duration at different interfaces. Also shown is an image of laser heating at t = 2.7 x 10^{-8} s illustrating the localization of laser heating in the *a*-IGZO TFT (only TFT region is shown).

As previously shown, the temperature at the center of the passivation-*a*-IGZO interface is much lower than the same interface near the source/drain. Near the source/drain region, the temperature of this interface varies from 1103.57 °C at 80 mJ/cm^2 up to 1513.38 °C at 110 mJ/cm^2. Meanwhile, the temperature at the center of passivation-*a*-IGZO interface is 705.33 °C at 80 mJ/cm^2 and it increases to 968.14 °C at 110 mJ/cm^2. These temperatures are similar to the previously reported simulated maximum temperature of roughly 1500 °C at 150 mJ/cm^2 for *a*-IGZO TFTs irradiated by ELA [43]. Nevertheless, the previously reported simulations did not take into account the heat transfer/dissipation contributions from other layers in the TFT such as the source/drain and were largely 1D simulations. In this case, the 2D simulation is helpful in identifying any spatial variation and possible degradation sites – things that are not possible with 1D simulation. Furthermore, the 2D simulations approximate the results of the 3D simulations wherein the 2D simulation result is just the cross-section of the 3D heat simulation. This is also considering that the cross section is symmetric across the

third axis/dimension (the depth direction, into or out of the page of Fig 4.6). Naturally, a 3D simulation will be more precise but would take a longer time and more processing power, but considering the symmetry and materials used, the 2D simulation is quite sufficient.

More importantly, Fig 4.6 illustrates how the laser heating is localized in the upper layers of the TFT. The simulation also demonstrates how heating induced by ELA penetrates throughout the 70 nm thickness of *a*-IGZO ensuring that the whole *a*-IGZO and not just the top layers are annealed. Here, the 100 nm thick SiO_2 acts as a buffer layer that effectively suppress the further propagation of heat into the substrate. This prevents any thermal damage or degradation at the substrate layer. Compared to the observed high temperatures in the upper layers, the maximum temperature at the SiO_2-Si interface, which corresponds to the substrate top surface, varied from a very low temperature of 20 ^oC to 22.78 ^oC when fluence energy is increased from 80 mJ/cm^2 and 110 mJ/cm^2, respectively. In effect, any flexible material can be used as the substrate, even paper – as long as the appropriate fluence energies, gate insulator materials and thicknesses are used. From this analysis, ELA is a very attractive annealing alternative that ensures low temperature at the substrate. Furthermore, analysis of 2D heat simulations is crucial in optimizing ELA conditions and material selection during *a*-IGZO TFT fabrication for flexible applications.

4.5 KrF ELA

4.5.1 Device fabrication

A lower wavelength, higher energy excimer laser, KrF ELA, was also used to anneal already-passivated *a*-IGZO TFTs. The fabrication of the unpassivated TFT is the

same as in section 4.4.1. TFTs were again not subjected to 300 ºC furnace annealing in AT atmosphere. Me 60/Ph 40 passivation layer is spin coated as passivation material on the *a*-IGZO TFT at a main spin rate of 3000 rpm for 15 s. To evaporate the precursor and cure the passivation, a 2 step heat treatment was then performed on a hot plate by first, prebaking at a temperature of 130 ºC for 90 s and finally, post-baking at 300 ºC for 1 hour in ambient atmosphere. Dry etching was performed by RIE with a CF_4/O_2/Ar gas mixture to form the contact holes. The Me 60/Ph 40 TFTs subjected to dry etching and which will be irradiated by KrF ELA were not subjected to the customary 300 ºC O_2 post-annealing process.

Similar to the process in XeCl ELA, KrF ELA was used to anneal the passivated *a*-IGZO TFT by irradiating each TFT with only one shot under ambient atmosphere at room temperature. The ambient atmosphere was selected instead of N_2 ambient because KrF ELA has higher energy compared to XeCl and annealing in N_2 would lead to higher conductive *a*-IGZO films. The wavelength of the laser source used was 248 nm. A beam *W/L* of 690/262 μm was used. Again, this beam size is much larger than the size of a single *a*-IGZO TFT. Me 60/Ph 40 is almost completely transparent at 248 nm with a transmittance of 84% (see Fig 2.3). Therefore, it is expected that the majority of the laser will penetrate the passivation and completely anneal the *a*-IGZO channel.

4.5.2 Electrical characteristics

The electrical characteristics before KrF ELA (after passivation and etching) and after the KrF ELA process were measured. Fig 4.7 shows the comparison of the transfer characteristics before and after KrF ELA irradiation. Similar to the results shown in the XeCl ELA discussion section, the passivated TFTs that were not annealed have a high

off-current and severe degradation in the transfer curves. After irradiation with KrF ELA at 80 mJ/cm^2, the electrical characteristics were vastly improved. Clear switching operation is achieved with a high saturation mobility 13 cm^2/Vs and a small V_{th} of 0.5 V. These electrical characteristics are again competitive with furnace annealed samples and greater than the μ reported by other low temperature annealing processes. In addition, unlike the XeCl case, no degradation is observed in the saturation region after KrF ELA suggesting good interface between the channel and the metal electrodes and possible formation of molybdenum oxide was suppressed. This was probably because of the lower heating induced at the metal-channel interface or a smoother temperature gradient at that region since the Me 60/Ph 40 can absorb some of the laser energy unlike Me 100. However, hump effect is observed after KrF ELA irradiation even at a low fluence energy of 80 mJ/cm^2. The hump effect shows that optimization of fluence energy is still needed to also improve the stability of ELA irradiated samples. This is because, currently, the ELA fluence energy is optimized to enhance the electrical properties of passivated *a*-IGZO TFTs. Nevertheless, the P-PSQ ensures the temporal stability of the TFT. Increasing the fluence energy further to 100 mJ/cm^2 causes the off-current to increase substantially which implies a higher conductivity for *a*-IGZO. This shows that the appropriate window for good process conditions for the higher energy KrF ELA is narrower compared to XeCl ELA.

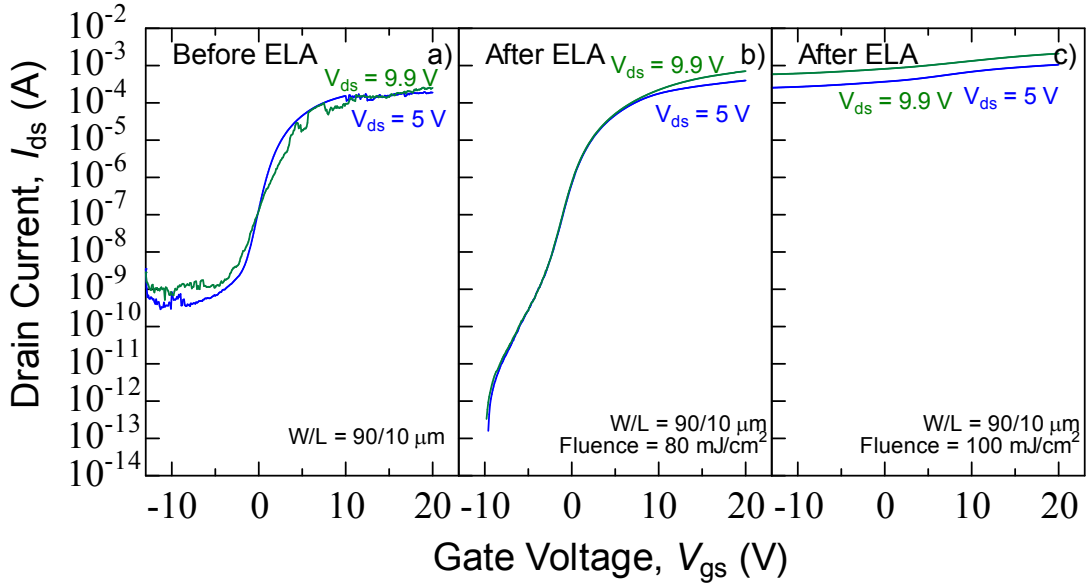

Fig 4.7 Comparison of transfer characteristics of Me 60/Ph 40 passivated *a*-IGZO TFT a) before ELA, b) KrF ELA at 80 mJ/cm^2, and c) KrF ELA at 100 mJ/cm^2. TFTs had a *W/L* = 90/10 μm.

4.6 Effect of ELA on *a*-IGZO TFTs

SIMS analysis was again performed to understand what happens to the elemental composition in the *a*-IGZO during ELA. The hydrogen and carbon elemental composition of *a*-IGZO layer of unpassivated *a*-IGZO (green line), furnace annealed Me 60/Ph 40 passivated *a*-IGZO (blue line), and Me 60/Ph 40 passivated *a*-IGZO (light purple dashed line) were compared in Fig 4.8 and Fig 4.9, respectively. Both samples passivated by Me 60/Ph 40 (either furnace annealed or irradiated by KrF ELA) had a much higher H and C concentration compared to unpassivated sample. This trend has been established in chapter 2 that NP-PSQ passivation increases the H and C content in the *a*-IGZO layer. However, furnace annealed Me 60/Ph 40 or those that were O_2 post-annealed in the furnace has a higher H and C compared to the samples only irradiated by KrF ELA. Nevertheless, the conclusion that can be derived from this SIMS

profile is that the KrF ELA process, despite inducing very low local temperature in the substrate and only applied at a very short time (~100 ns), was able to approximate the annealing performed by the much longer (2h) and non-selective furnace annealing process. KrF ELA, because of the high temperature, also introduced a high amount of H and C into the *a*-IGZO layer. The high thermal stability of the Me 60/Ph 40 is also very helpful in this ELA process because even though the induced temperature in the upper layers is high, no damage was observed in the passivation layer.

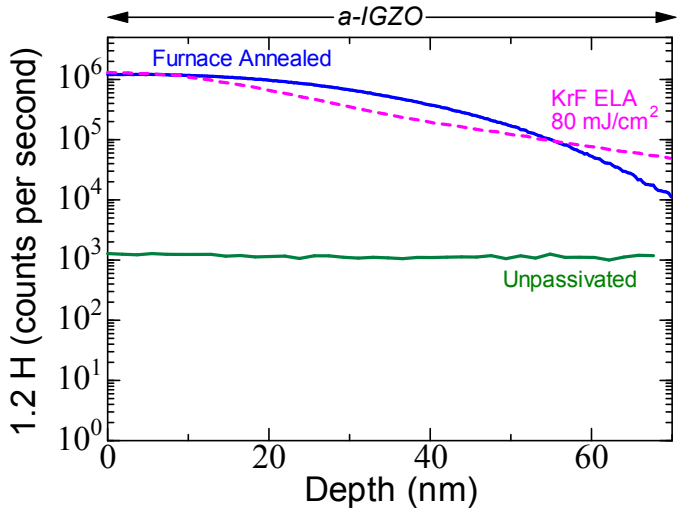

Fig 4.8 Comparison of the hydrogen elemental profile in the *a*-IGZO layer of furnace annealed Me60/Ph 40 (blue solid line), Me 60 Ph 40 subjected to KrF ELA at 80 mJ/cm^2 (light purple dashed line) and unpassivated sample. The 0 nm depth is the IGZO-passivation interface.

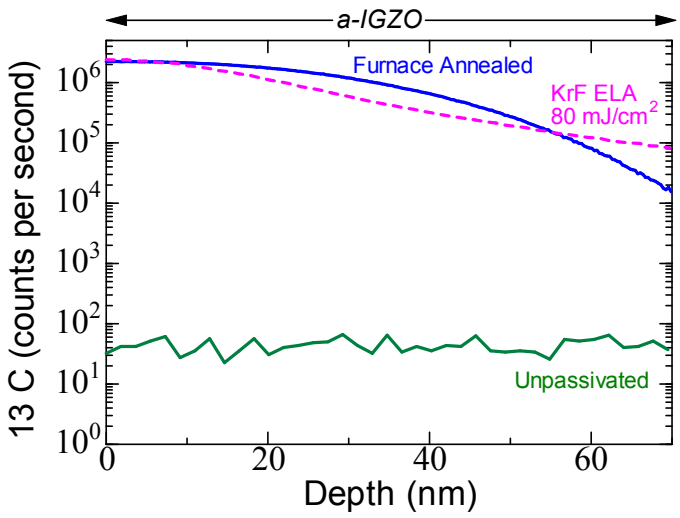

Fig 4.9 Comparison of the carbon elemental profile in the *a*-IGZO layer of furnace annealed Me60/Ph 40 (blue solid line), Me 60 Ph 40 subjected to KrF ELA at 80 mJ/cm^2 (light purple dashed line) and unpassivated sample (green line).

Fig 4.10 illustrates the O1s XPS spectra in the *a*-IGZO layer bulk of O_2 annealed unpassivated *a*-IGZO (green line), furnace annealed Me 60/Ph 40 passivated *a*-IGZO (blue line) and Me 60 Ph 40 passivated *a*-IGZO subjected to KrF ELA at 80 mJ/cm^2 (light purple dashed line). The O1s XPS profiles mimic the comparison of elemental composition in figs 4.8 and 4.9. Both the furnace annealed and KrF ELA Me 60/Ph 40 have higher binding energy shifts compared to the O_2 annealed unpassivated samples. Since higher binding energy in O1s are related to hydroxide/carbon related bonds (as discussed in Chapter 2). This shows that both passivated samples (furnace annealed or KrF ELA irradiated) had more H and C in the *a*-IGZO layer. Comparison between the furnace annealed and KrF ELA irradiated sample shows that furnace annealed case had a higher binding energy shift which again confirms that it has more H and C related bonds, as shown in the earlier SIMS profiles (Figs 4.8 and 4.9).

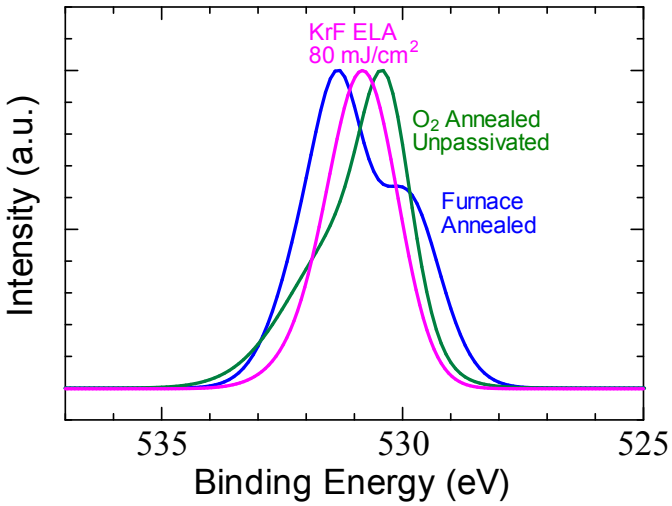

Fig. 4.10 Comparison of O1s XPS spectra in the *a*-IGZO layer of furnace annealed Me60/Ph 40 (blue solid line), Me 60 Ph 40 subjected to KrF ELA at 80 mJ/cm^2 (light purple dashed line) and unpassivated sample (green line).

Fig 4.11a is the depth profile analysis the O1s XPS profile of Me 60/Ph 40 *a*-IGZO irradiated by KrF ELA at 80 mJ/cm^2. Fig 4.11b compares the XPS profiles in fig 4.11a (minus the XPS profile at the passivation surface) with the *a*-IGZO bulk of the O_2 annealed unpassivated sample. The interface and bulk was determined by monitoring the Zn 2p, In 3d, Ga 2p, and Si 2p signal intensities. The interface is determined by the decrease in Si 2p signal and the simultaneous increase of the three In 3d, Ga 2p, and Zn 2p XPS signals. At the bulk, very minimal Si 2p can be found and In, Ga, and Zn intensities are very high. From Fig 4.11, it appears that the shift to higher binding energy is more pronounced at the interface *a*-IGZO shares with the passivation compared to the *a*-IGZO bulk. Since the O1s XPS spectra of the passivation surface is at a much higher binding energy (corresponding to mostly Si-O_x bonding at binding energies from 532.5-533 eV), the higher binding energy shift for the XPS profile at the interface can be attributed to the increased H and C related bonds at a binding energy of 532 eV. This result implies that

most of the C and H introduced by ELA into the a-IGZO are concentrated at the interface and the upper few nanometers of *a*-IGZO (~20 nm). Nevertheless, in fig. 4.11b the binding energy peak of the *a*-IGZO bulk of KrF ELA irradiated Me 60/Ph 40 is higher than that of the unpassivated sample.

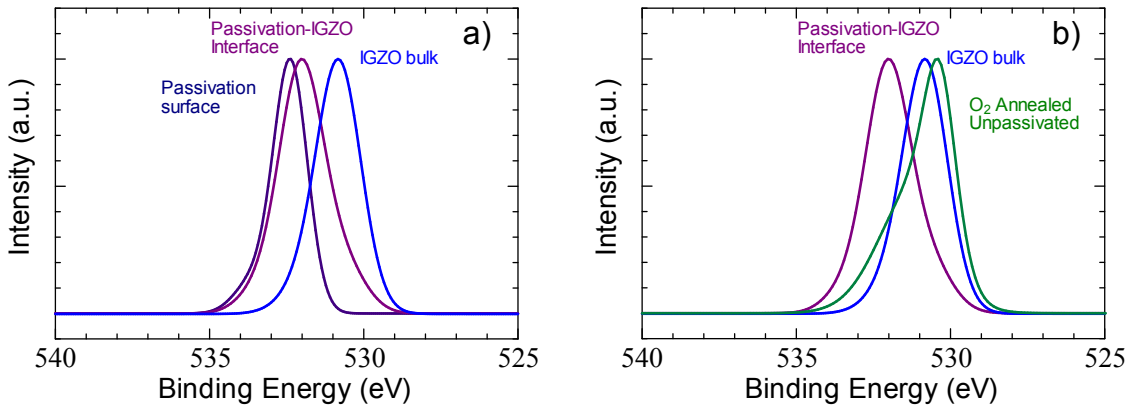

Fig. 4.11 a) Depth profile analysis of O1s spectra in the passivation (violet line), passivation-*a*-IGZO interface (dark purple line) and *a*-IGZO bulk (blue line) of Me 60/Ph 40 subjected to KrF ELA at 80 mJ/cm^2; b) Comparison with the O1s spectra of the *a*-IGZO bulk of unpassivated *a*-IGZO (green line) minus the passivation XPS profile.

Fig 4.12 shows the comparison of the Me 100 irradiated by XeCl ELA at 110 mJ/cm^2 (light purple line), furnace annealed Me 100 (red line), and O_2 annealed unpassivated sample (green line). A similar observation is also seen in the case of Me 100 subjected to XeCl ELA where in the binding energies of both furnace annealed and KrF ELA irradiated Me 100 are higher compared to unpassivated sample. However, in this case, the XeCl ELA introduced more H and C compared to the furnace annealed samples. These results further confirm the observation in the analysis of SIMS elemental profiles that ELA also introduces H and C into *a*-IGZO, although concentrated near the top few nm, and that it can approximate the effect of furnace annealing. This is despite ELA being

applied at a very short time compared to the non-selective heating induced by furnace annealing over a much longer time.

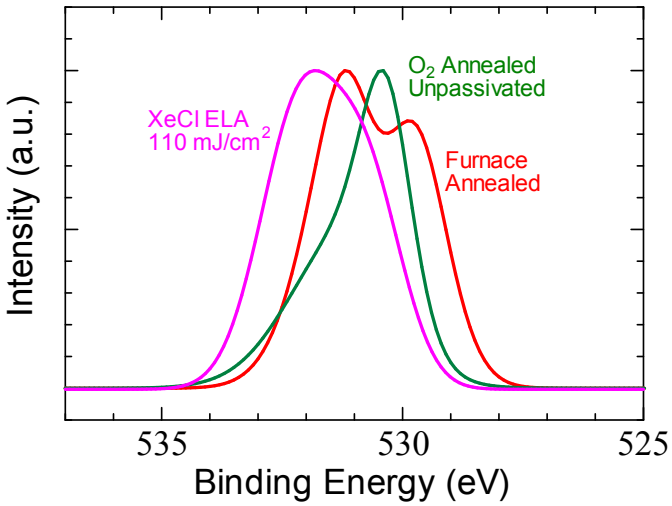

Fig. 4.12 Comparison of O1s XPS spectra in the *a*-IGZO layer of furnace annealed Me60/Ph 40 (blue solid line), Me 60 Ph 40 subjected to XeCl ELA at 110 mJ/cm^2 (purple dashed line) and unpassivated sample (green line).

Fig 4.13 shows the structural characterization by X-ray Diffraction (XRD, RINT-TTRIII/NM) of unpassivated *a*-IGZO irradiated by KrF ELA at 60 mJ/cm^2 (green line), Me 100 passivated *a*-IGZO irradiated by KrF ELA at 60 mJ/cm^2 (red line), and Me 60/Ph 40 passivated *a*-IGZO irradiated by KrF ELA at 80 mJ/cm^2 (blue line). All samples had identical Si substrates with thermally oxidized 100 nm SiO_2. The peak at ~50^o corresponds to the Si substrate, while the broad peak at ~33^o and 56^o corresponds to amorphous *a*-IGZO [48, 49]. No sharp peaks are observed at both the 33^o and 56^o positions suggesting that the *a*-IGZO films after ELA in these samples are largely amorphous. This implies that even if the induced temperatures at the *a*-IGZO layer is very high, the *a*-IGZO films are still amorphous since these induced high temperatures are

only present in a very short amount of time (~100 ns). This is similar to previous ELA results on unpassivated *a*-IGZO [43]. Maintaining the amorphous phase ensures that problems associated with crystalline oxide semiconductors such as non-uniformity and lower electrical characteristics because of the presence of grain boundaries can be avoided altogether. Table 4.I summarizes the density and roughness of *a*-IGZO measured by X-ray reflectivity (XRR, RINT-TTRIII/NM) under different process conditions annealed by KrF ELA, conventional, or both; unpassivated, Me 100 passivated or Me 60/Ph 40 passivated samples. In general, there was an increase in the density of *a*-IGZO films after being irradiated by KrF ELA. This suggests that more compact films are formed by irradiating with KrF ELA. Combining KrF ELA with AT annealing in the case of unpassivated *a*-IGZO barely changed the density compared to when only KrF ELA is applied. On the other hand, roughness of *a*-IGZO is improved when KrF ELA is combined with AT annealing. High density and good roughness in the *a*-IGZO is obtained after KrF ELA at 80 mJ/cm^2 of Me 60/Ph 40 passivated *a*-IGZO. These results show that aside from inducing a low temperature at the substrate, KrF ELA can form highly compact *a*-IGZO films with good roughness especially for the case of Me 60/Ph 40 passivated *a*-IGZO.

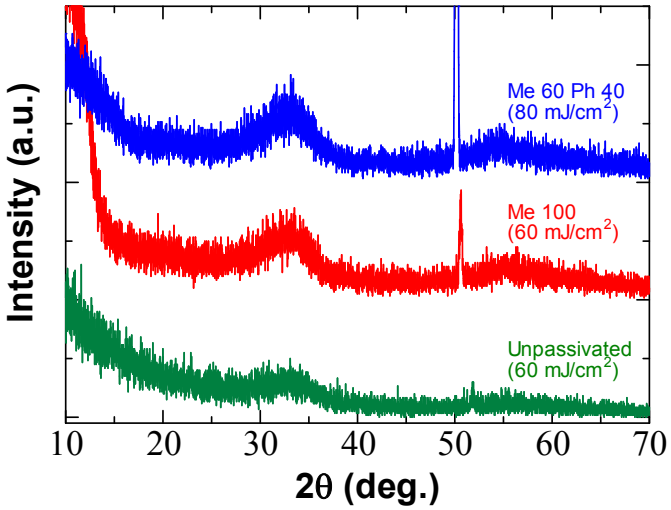

Fig. 4.13 Structure characterization of KrF ELA irradiated unpassivated *a*-IGZO at 60 mJ/cm^2 (green line), Me 100 passivated *a*-IGZO at 60 mJ/cm^2 (red line) and Me 60/Ph 40 passivated sample (blue line) by XRD using CuKα line.

Table 4.I Summary of changes in density and roughness of *a*-IGZO of conventional unpassivated *a*-IGZO [48], Me 60/Ph40 passivated *a*-IGZO irradiated by KrF ELA at 80 mJ/cm^2, unpassivated *a*-IGZO irradiated by KrF ELA at 60 mJ/cm^2, and unpassivated *a*-IGZO subjected to AT Annealing (300 ºC 2h) and irradiated by KrF ELA at 65 mJ/cm^2

	Density (g/cm^3)	**Roughness (nm)**
Conventional *a*-IGZO [48]	6.1	0.29
KrF ELA (60 mJ/cm^2) Unpassivated *a*-IGZO	7.11	0.80
KrF ELA (65 mJ/cm^2) + AT Annealing Unpassivated *a*-IGZO	7.13	0.59
KrF ELA (60 mJ/cm^2) Me 100 passivated *a*-IGZO	6.72	0.94
KrF ELA (80 mJ/cm^2) Me 60/Ph40 passivated *a*-IGZO	7.59	0.45

4.7 Summary

Developing flexible processes and technologies in the fabrication of *a*-IGZO based devices is a popular and important research topic for many research groups. For *a*-IGZO to be successfully used in next-generation devices, it should be fabricated at a low temperature while ensuring high performance and stability. In section 4.2, many conventional and low temperature annealing methods are discussed. Many groups have shown different methods to address the problem of lowering the process temperature but there are still issues in the lower performance observed in most of these processes. In addition, most of these devices employing low temperature processes are unpassivated. These problems can be solved by developing a low temperature annealing method or selective heating method that ensures high performance such as ELA on already-passivated *a*-IGZO TFTs.

ELA is introduced as a low temperature annealing alternative in section 4.3. While technically it is a high temperature method because of the high temperature it induces at the point of impact, its selective nature and the clever choice of fluence energies and materials can effectively restrict the high temperature in the upper layers. This effectively reduces the temperature at the substrate which is where the temperature should be absolutely reduced. Nevertheless, previous research on ELA of oxide TFTs dealt with unpassivated samples.

Two ELA methods are presented: XeCl ELA in section 4.4 and KrF ELA section 4.5. ELA is applied on already-passivated TFTs. The significance of this method is that the annealing process is performed as the last step in the fabrication process. Switching this process, for example, irradiating with ELA before the passivation and etching of contact holes will mean that an additional annealing step is needed after the passivation

and dry etching of the TFT. Annealing with ELA on already-passivated *a*-IGZO TFTs effectively replaced two high temperature annealing processes: AT annealing at 300 ^{o}C for 2h used for contact annealing and O_2 post annealing at 300 ^{o}C for 2h used for reversing etch and fabrication damage. Furthermore, the performance of both types of ELA is shown to be comparable to furnace annealed samples and superior to most low temperature annealing methods. The NP-PSQ passivation layers also ensure that these TFTs will have an effective barrier against ambient effects.

2D heat simulation by COMSOL Multiphysics is also introduced as an effective method to identify regions susceptible to degradation and to ensure that substrate temperature is low. The simulation explained why ELA at very small dimensions can induce degradation especially near the source/drain region when un-optimized ELA conditions are used. Therefore, 2D heat simulation is an important tool in optimizing fluence energies, selecting appropriate materials, and fabricating appropriate device sizes. The simulation also shows how the substrate temperature is kept low because of the appropriate choice of gate insulator material that acts as a buffer layer/heat suppressor.

Section 4.6 explains the effect of ELA on the elemental composition, chemical bonding, and mechanical structure of *a*-IGZO. ELA irradiation introduces a large amount of H and C into the *a*-IGZO layer similar to furnace annealing. Results show that ELA can approximate the effect of furnace annealing even if it is applied for a much shorter time compared furnace annealing. Analysis of XPS profiles, especially the depth profile, shows that the H and C introduced into the *a*-IGZO layer after ELA irradiation are concentrated in the top few nm and interface of *a*-IGZO with the passivation. XRD analysis shows that *a*-IGZO were amorphous after ELA irradiation even if it was exposed to very high temperatures. This is because the high temperature is only induced at a very

short time (~100 ns). Density and roughness results from XRR shows that highly compact films with good roughness can be formed by ELA. These results show the promise of ELA as a low temperature annealing alternative which is compatible with PSQ passivated *a*-IGZO TFTs. With this, highly reliable and high performance *a*-IGZO TFTs fabricated on flexible substrates can be realized.

References

[1] K. Nomura, H. Ohta, A. Takagi, T. Kamiya, M. Hirano, and H. Hosono, Nature, **432**, 488 (2004)

[2] P. Barquinha, R. Martins, L. Pereira, and E. Fortunato, E., Electronics with and on Paper, in Transparent Oxide Electronics: From Materials to Devices, John Wiley & Sons, Ltd, Chichester, UK (2012).

[3] E. Fortunato, P. Barquinha, and R. Martins, Adv. Mater., **24**, 2945 (2012).

[4] K. Nomura, A. Takagi, T. Kamiya, H. Ohta, M. Hirano, and H. Hosono, Jpn. J. Appl. Phys. **45** (2006) 4303.

[5] M. Mativenga, M. H. Choi, J. W. Choi, J. Jang, IEEE Elect. Dev. Lett., **32**, (2011) 70.

[6] J. K. Jeong, Semicond. Sci. Technol. **26**, (2011) 034008.

[7] H. Chen, Y. Cao, J. Zhang, and C. Zhou, Nature Commun., **5**, (2014), 4097.

[8] K. Nomura, T. Kamiya, H. Ohta, M. Hirano and H. Hosono, Appl. Phys. Lett., **93** (2008) 192107.

[9] K. Nomura, T. Kamiya, M. Hirano and H. Hosono, Appl. Phys. Lett., **95,** (2009) 013502.

[10] T. Kamiya and H. Hosono, NPG Asia Materials, **2**, (2010) 15.

[11] W.-T. Chen, S.-Y. Lo, S.-C. Kao, H.-W. Zan, C.-C. Tsai, J.-H. Lin, C.-H. Fang, and C.-C. Lee, IEE Elect. Dev. Lett., **32**, (2011), 1552.

[12] M. Kimura, T. Nakanishi, K. Nomura, T. Kamiya, and H. Hosono, Applied Physics Letters, **92**, (2008) 133512.

[13] J. H. Lim, J. H. Shim, J. H. Choi, J. Joo, K. Park, H. Jeon, M. R. Moon, D. Jung, H. Kim, and H.-J. Lee: Appl. Phys. Lett. **95** (2009) 012108.

[14] K. M. Kim, C. W. Kim, J.-S. Heo, H. Na, J. E. Lee, C. B. Park, J.-U. Bae, C.-D. Kim,

M. Jun, Y. K. Hwang, S. T. Meyers, A. Grenville, and D. A. Keszler: Appl. Phys. Lett. **99** (2011) 242109.

[15] C. Avis and J. Jang, J. Mater. Chem., **21**, (2011) 10649.

[16] P. K. Nayak, T. Busani, E. Elamurugu, P. Barquinha, R. Martins, Y. Hong, and E. Fortunato: Appl. Phys. Lett. **97** (2010) 183504.

[17] D.-H. Lee, Y.-J. Chang, G. S. Herman, and C.-H. Chang, Adv. Mater., **19**, (2007) 843.

[18] K. H. Ji, J.-I. Kim, H. Y. Jung, S. Y. Park, R. Choi, U. K. Kim, C. S. Hwang, D. Lee, H. Hwang and J. K. Jeong, Appl. Phys. Lett., **98**, (2011) 103509.

[19] M. N. Fujii, Y. Ishikawa, M. Horita and Y. Uraoka, ECS J. Solid Stat. Sci. Technol., **1**, (2014) Q3050.

[20] X. Yua, J. Smith, N. Zhou, L. Zeng, P. Guo, Y. Xia, A. Alvarez, S. Aghion, H. Lin, J. Yu, R. P. H. Chang, M. J. Bedzyk, R. Ferragut, T. J. Marks, and A. Facchetti, Proc. Natl. Acad. Sci. U.S.A., **112,** (2015) 3217.

[21] M.-C. Choi, Y. Kim, C.-S. Ha, Prog. Polym. Sci., **33**, (2008) 581.

[22] E. Fortunato, N. Correia, P. Barquinha, L. Pereira, G. Goncalves, and R. Martins, IEEE Elect. Dev. Lett., **29**, (2008) 988

[23] K.K. Banger, Y. Yamashita, K. Mori, R.L. Peterson, T. Leedham, J. Rickard, and H. Sirringhaus, Nature Mater., **10**, (2011) 45.

[24] M. G. Kim, M. G. Kanatzidis, A. Facchetti, and T. J. Marks, Nature Mater. **10**, (2011) 382–388.

[25] A. Hardy and M. K. Van Bael, Nature Mater. **10**, (2011) 340–341.

[26] S. Yang, J. Y. Bak, S.-M. Yoon, M. K. Ryu, H. Oh, C.-S. Hwang, G. H. Kim, S.-H. K. Park, and J. Jang, IEEE Elect. Dev. Lett. **32**, (2011) 1692.

[27] Y.-H. Kim, J.-S. Heo, T.-H. Kim, S. Park, M.-H. Yoon, J. Kim, M. S. Oh, G.-R. Yi, Y.-Y. Noh, and S. K. Park. Nature, **489**, (2012) 128.

[28] H.-W. Zan, W.-T. Chen, C.-W. Chou, C.-C. Tsai, C.-N. Huang, and H.-W. Hsueha, Electrochem. and Solid-Stat. Lett., **13** (2010) H144.

[29] I.-K. Lee, K. H. Lee, S. Lee, and W.-J. Cho, ACS Appl. Mater. Interfaces, **6**, (2014) 22680.

[30] C. S. Fuh, P. T. Liu, L. F. Teng, S. W. Huang, Y. J. Lee, H. P. Shieh, S. M. Sze, IEEE Elect. Dev. Lett., **34**, (2013) 1157.

[31] A. Gat, L. Gerzberg, J. F. Gibbons, T. J. Magee, J. Peng, and J. D. Hong, Appl. Phys. Lett., **33,** (1978) 775.

[32] T. Sameshima, S. Usui, and M. Sekiya, IEEE Elect. Dev. Lett., **7**, (1986), 276.

[33] S. Uchikoga and N. Ibaraki, Thin Solid Films, **383**, (2001) 19.

[34] H. Kuriyama, S.Kiyama S. Noguchi, T. Kuwahara, S. Ishida, T. Nohda, K. Sano, H. Iwata, H. Kawata, M. Osumi, S. Tsuda, S. Nakano and Y. Kuwano, Jpn. J. Appl. Phys., **30**, (1991) 3700.

[35] K. Sera, F. Okumura, H. Uchida, S. Itoh, S. Kaneko, and K. Hotta, IEEE Transact. on Elect. Dev., **36**, (1989), 2868.

[36] H. Kuriyama, T. Nohda, S. Ishida, T. Kuwahara, S. Noguchi, S. Kiyama, S. Tsuda and S. Nakano, Jpn. J. Appl. Phys., **32**, (1993) 6190.

[37] J. Im, H. J. Kim, and M. Thompson, Appl. Phys. Lett. **63**, (1993) 1969.

[38] P. M. Smith, P. G. Carey, and T. W. Sigmon, Appl. Phys. Lett., **70**, (1997) 342.

[39] M. Fujii, Y. Ishikawa, R. Ishihara, J. van der Cingel, M. R. T. Mofrad, M. Horita , and Y. Uraoka, Appl. Phys. Lett., **102**, (2013) 122107.

[40] C.-Y. Tsay and M.-C. Wang, Ceramics Int. **39,** (2013), 469.

[41] Y.-H. Yang, S.S. Yang, K.-S. Chou, IEEE Elect. Dev. Lett., **31**, (2010), 969.

[42] M. Nakata, K. Takechi, K. Azuma, E. Tokumitsu, H. Yamaguchi, and S. Kaneko, Appl. Phys. Exp., **2,** (2009) 021102.

[43] M. Nakata, K. Takechi, T. Eguchi, E. Tokumitsu, H. Yamaguchi and S. Kaneko, Jpn. J. Appl. Phys., **48,** (2009) 081607.

[44] B. D. Ahn, W. H. Jeong, H. S. Shin, D. L. Kim, H. J. Kim, J. K. Jeong, S.-H. Choi, and M.K.Han,Electrochem. Solid-Stat.Lett., **12**, (2009) H430-H432

[45] M. Nakata, K. Takechi, S. Yamaguchi, E. Tokumitsu, H. Yamaguchi, and S. Kaneko, Jpn. J. Appl. Phys., **48,** (2009) 115505.

[46] M. Nakata, H. Tsuji, Y. Fujisaki, H. Sato, Y. Nakajima, T. Takei, T. Yamamoto, and T. Kurita, Appl. Phys Lett. **103**, (2013) 142111.

[47] J. Förster and H. Vogt, Excimer Laser-Annealing of Amorphous Silicon Layers, Proc. of 2011 COMSOL Conference, Stuttgart, (2011).

[48] T. Kamiya, K. Nomura, and H. Hosono, J. Display Technol., **5** (2009) 273.

[49] K. Nomura, T. Kamiya, H. Ohta, T. Uruga, M. Hirano, and H. Hosono, Phys. Rev. B, **75**, (2007) 035212-1.

Chapter 5
Conclusion

5.1 Conclusions

Display devices are important both as a terminal and interface in modern information technology. The heart of the display is the TFT and fabricating high-performance TFTs with excellent stability is of utmost importance. Furthermore, there is a need for more advanced display applications such as transparent and flexible applications. It is therefore important to analyze degradation mechanisms in *a*-IGZO and develop methods to suppress degradation. Understanding reliability improvement mechanisms and how different elements introduced in *a*-IGZO affect its properties are also necessary. In addition, to realize transparent and flexible applications, developing an annealing process that ensures low temperature especially at the substrate is essential.

The most significant results that this study contributes are summarized as follows: first, organic-inorganic hybrid PSQ passivation layers fabricated by simple solution process are introduced and were shown to be highly reliable. Second, the effects of hydrogen, carbon, and fluorine, on the properties of *a*-IGZO are analyzed and their contributions in the reliability improvement in *a*-IGZO are detailed. Understanding the roles of these elements are significant since these elements, especially hydrogen and carbon, are often incorporated into *a*-IGZO during fabrication. Third, ELA is demonstrated as an alternative annealing method on already passivated *a*-IGZO TFTs which ensures low temperature at the substrate. The results in this thesis is essential in developing new materials for high performance and highly reliable *a*-IGZO TFTS for

transparent, printed, and flexible applications.

The backchannel is one of the most vulnerable areas of the TFT because of several ambient effects that contribute to degradation. In chapter 2, the role of passivation layers in inhibiting ambient effects and ensuring highly reliable *a*-IGZO TFTs are discussed. A new class of transparent organic-inorganic hybrid passivation layers based on PSQ is introduced as an alternative to popular inorganic passivation layers. These NP-PSQ passivation layers are fabricated by solution process making them attractive for future printed transparent applications. NP-PSQ passivation layers are shown to have good surface roughness comparable and even better to some inorganic passivation layers. In addition, these layers have excellent hydrophobicity that makes them appealing in water repellant applications. Furthermore, bias stress tests (PBS, NBS, and NBIS) and humidity stress show the excellent reliability of *a*-IGZO TFTs passivated by these passivation layers. Through SIMS and XPS analyses, the roles of H and C in improving the reliability of *a*-IGZO are also detailed in chapter 2. It was shown that H occupies V_O to reduce the V_O concentration. However, H can also form OH which can cause hump effect. Therefore, it is important to find methods to either control the OH amount or suppress its effect. C was shown to form acceptor states ($C_{Zn} + 2O_i$) to reduce the V_{th} shift during NBIS and capture photo-generated electrons that drift towards the backchannel. The excess oxygen from $C_{Zn} + 2O_i$ can also suppress the OH activity to some extent. Clarifying the effect of H and C is important since H and C are common materials that are incorporated into semiconductors during fabrication especially of organic materials.

Most passivation layers including NP-PSQ passivation layers need dry etching to form the contact holes. However, process damage such as in dry etching can affect the characteristics of *a*-IGZO. It therefore makes sense to develop a passivation layer that

eschews dry etching. In chapter 3, P-PSQ is presented as a photosensitive organic-inorganic hybrid passivation layer. In this case, it retains the excellent reliability that is typical of PSQ passivation layers while at the same time not needing any dry etching. Bias stress and humidity stress results again proved the superb reliability of P-PSQ. In addition, the P-PSQ passivation process further simplifies the already simple fabrication process in fabricating NP-PSQ. What sets even P-PSQ passivation apart from NP-PSQ is that it does not suffer from hump effect typical of organic-based passivation layers. In effect, it has the superb performance expected of inorganic materials while utilizing a simple solution and photosensitive process that makes it attractive in transparent printed applications.

The key addition of F to P-PSQ, as shown in the SIMS analysis, helped in the suppression of the hump effect and contributed in the reliability of *a*-IGZO TFTs. F like H can occupy the V_O further reducing the V_O concentration. Aside from this, F can also substitute and stabilize weakly bonded O by preferentially bonding with Zn to form a stronger Zn-F bond. Moreover, F can suppress the hump effect by forming a strong secondary bond with OH effectively neutralizing the H dissociation that occurs during stress, especially NBS. Understanding the roles of F and P-PSQ are crucial in developing advanced materials with new functionalities.

The development of flexible processes is integral in the development of next-generation *a*-IGZO devices. To achieve flexibility, the major requirement is ensuring a low temperature at the substrate region. An annealing process that induce heat localization has an advantage over a process that just lowers the annealing temperature since *a*-IGZO still requires up to 400 ^oC to have a high performance and stability. Successful methods to lower the temperature to less than 300 ^oC often employ special

precursors that produce their own fuel/heat in an exothermic process or precursors that decompose when exposed to UV irradiation. ELA is presented as an alternative annealing method that ensures low temperature at the substrate. XeCl or KrF ELA irradiation of *a*-IGZO TFTs passivated with transparent NP-PSQ passivation layers reversed damage caused by etching and more importantly improved their transfer characteristics. ELA led to a low V_{th} and enhanced the mobility to ~13 cm^2/Vs. These electrical characteristics are comparable to furnace annealed samples and much better than other low temperature annealing alternatives that typically produce TFTs with mobility less than 10 cm^2/Vs. 2D heat simulation also identified the vulnerable areas of *a*-IGZO TFTs during ELA. Identifying these areas can explain the size dependence of the electrical characteristics after ELA and help in properly optimizing process conditions when performing ELA on TFTs with small dimensions. The 2D heat simulation also helps ensure that substrate temperature during ELA will be low. Therefore, 2D heat simulation is an important tool in the optimization of fluence energies, fabrication of appropriate device sizes, and selection of optimal materials for *a*-IGZO TFTs that will be applied for flexible applications.

The effect of incorporation of H and C during ELA was confirmed by SIMS and XPS analysis. Even if ELA is only performed in a very short time, it was able to approximate the effect of furnace annealing which is typically applied in a longer time in a non-selective manner. XPS depth profile analysis reveals that the C and H introduced into the *a*-IGZO are concentrated near the interface and the top few nm. XRD results show that the *a*-IGZO retains its amorphous manner even after ELA of 80mJ/cm^2. This is because the *a*-IGZO is only exposed to the high temperature during a very short time. At the same time, during the entire ELA duration, the temperature at the substrate layer is still very low. Through XRR analysis, ELA irradiation is shown to form high quality

dense films with good roughness. These results show how crucial ELA is in the realization of *a*-IGZO in flexible applications. Successfully annealing already-passivated *a*-IGZO TFTs with ELA, while ensuring low substrate temperature, demonstrates the realization of highly reliable and high performance *a*-IGZO TFTs for transparent flexible applications.

5.2 Suggestions for future work

This study was able to successfully show two types of organic-inorganic hybrid passivation layers that can be fabricated by solution process. Both NP-PSQ and P-PSQ passivation were shown to have superb performance while utilizing a simpler fabrication process. These two types of passivation layers are attractive in the fabrication of *a*-IGZO TFTs for more advanced printed applications. Furthermore, this thesis was able to clarify the roles of C, H, and F in *a*-IGZO TFTs. Another significant result in this thesis is that ELA is shown to be an effective low temperature annealing process for already passivated *a*-IGZO TFTs. However, there are still issues and challenges that need to be clarified.

1. Development of all-printed oxide TFTs.

This study shows that printed passivation layers with superb performance can be fabricated. Developing an all-printed oxide TFT necessitates the development of gate insulators that can be fabricated by solution or printing process. Solution process oxide semiconductors and printed electrodes have been demonstrated before. PSQ is a good candidate as a printed gate insulator because of its insulating properties and excellent stability. However, efforts are needed to further lower the thickness of PSQ and reduce the H in PSQ. This is because a large amount of H in the gate insulator promotes

instability in *a*-IGZO because it can form extra donor states and generate additional electron traps. In addition, lowering the thickness of PSQ to ~100-200 nm ensures a high enough capacitance which leads to lower voltage needed to operate the TFT. Developing an all-printed oxide TFT also requires understanding the roles of H and organic materials in *a*-IGZO TFTs.

2. Fabrication of passivated oxide TFTs on flexible substrates such as paper.

This study has successfully shown that the temperatures induced by ELA in the substrate layer is very low that even paper can be used as substrate material. The problem is that PSQ still needs a baking process at 300 ^{o}C which can be lowered to as low as 230 ^{o}C. Nevertheless, *a*-IGZO TFTs passivated with NP-PSQ still had bad characteristics before ELA, even though it was already baked on a hot plate at 300 ^{o}C to form the passivation layer. In this suggestion, ELA can be used as the sole annealing process by completely bypassing the baking process and allowing ELA to selectively heat the NP-PSQ passivation. This is possible since Me 60/Ph 40 can absorb a portion of the KrF laser energy and because the temperature induced at the passivation-channel interface is very high. Naturally, new fluence energies will be needed to optimize this process. By following this process, passivated *a*-IGZO TFTs can be fabricated on flexible substrates such as paper.

An advantage of fabricating passivated oxide TFTs on any flexible substrate is its potential application in roll-to-roll (R2R) process. This advantage becomes more appealing in combination with the potential of developing printable materials to fabricate all-printed oxide TFTs on a flexible substrate. In this way, materials will be printed sequentially to form the *a*-IGZO TFT structure and then subsequently annealed with a

single shot of an excimer laser as the roll moves. This R2R process is especially attractive for efficient and low-cost mass production of *a*-IGZO TFTs on flexible substrates.

3. Advanced applications of ELA such as in highly reliable and high performance self-aligned a-IGZO TFTs.

By capitalizing on the location selectivity of ELA, more advanced applications of ELA can be realized. This includes developing a self-align process to further improve the performance of *a*-IGZO TFTs. A self-align process will increase the conductivity of *a*-IGZO that is directly overlapped with the source and drain regions, thus improving the contact of *a*-IGZO with the electrodes and reducing contact resistance. Performing this method is possible using PSQ passivation and employing a top gate structure. By coating the PSQ as a gate insulator over the *a*-IGZO and using the top gate electrode as a mask, ELA will only irradiate specific areas and the introduction of H into *a*-IGZO from PSQ will increase its conductivity. This is aside from the increase in conductivity induced by the selective heating due to ELA.

Advanced laser technologies and other laser wavelengths can also be used in ELA to further optimize the performance and reliability of passivated *a*-IGZO TFTs. For instance, an excimer laser with a longer wavelength such as XeF (351 nm) can allow for the use of P-PSQ as a passivation layer in *a*-IGZO TFTs irradiated by ELA. This is because P-PSQ has low transmittance at wavelengths lower than 300 nm but has transmittance greater than 80% at wavelengths greater than 350 nm. Advanced laser technologies such as multi-photon laser techniques can also be used to further modulate the wavelength. However, conditions such as interference and fluence energy optimization should be considered. Nevertheless, with these technologies, ELA can

enhance the electrical properties and reliability of *a*-IGZO TFTs at far lower substrate temperatures compared to conventional annealing methods.

List of publications

A. Academic journals

1. **Juan Paolo Bermundo**, Yasuaki Ishikawa, Haruka Yamazaki, Toshiaki Nonaka, Mami N. Fujii, and Yukiharu Uraoka, "Highly Reliable Photosensitive Organic-Inorganic Hybrid Passivation Layers for *a*-InGaZnO Thin-Film Transistors", Appl. Phys. Lett., submitted.
2. **Juan Paolo Bermundo**, Yasuaki Ishikawa, Haruka Yamazaki, Toshiaki Nonaka, and Yukiharu Uraoka, "Highly Reliable Polysilsesquioxane Passivation Layer for *a*-InGaZnO Thin-Film Transistors" ECS J. Sol. Stat. Sci. and Technol., **3(2)** (2014), Q16.

B. Peer-reviewed conference proceedings

1. **Juan Paolo Bermundo**, Yasuaki Ishikawa, Haruka Yamazaki, Toshiaki Nonaka, and Yukiharu Uraoka; "Highly reliable passivation layer for a-InGaZnO thin-film transistors fabricated using polysilsesquioxane", Mat. Res. Soc. Symp. Proc., **1633** (2014), 118.

Presented Works

A. Presentations at international conference

1. **Juan Paolo Bermundo**, Yasuaki Ishikawa, Mami N. Fujii, Michiel van der Zwan, Toshiaki Nonaka, Ryoichi Ishihara, Hiroshi Ikenoue, and Yukiharu Uraoka, "XeCl and KrF Excimer Laser Annealing of Oxide Thin-Film Transistors with Hybrid

Passivation Layer", 11th International Thin-Film Transistor Conference (ITC 2015), Rennes, France, February (2015).

2. **Juan Paolo Bermundo**, Yasuaki Ishikawa, Mami N. Fujii, Michiel van der Zwan, Toshiaki Nonaka, Ryoichi Ishihara, and Yukiharu Uraoka, "Excimer Laser Annealing of Amorphous Oxide Thin-film Transistors Passivated with Hybrid Passivation Layer", The 21st International Display Workshops (IDW '14), Niigata, Japan, December (2014).
3. Yasuaki Ishikawa, **Juan Paolo Bermundo***, Haruka Yamazaki, Mami Fujii, and Yukiharu Uraoka, "Interface Control toward Highly Reliable Amorphous InGaZnO Thin-Film Transistors", The 14th International Meeting on Information Displays (IMID 2014), Daegu, Korea, August (2014). **[Invited], ***speaker/presenter*
4. **Juan Paolo Bermundo**, Yasuaki Ishikawa, Haruka Yamazaki, Toshiaki Nonaka, and Yukiharu Uraoka, "Reliability Improvement in Amorphous InGaZnO Thin Film Transistors Passivated by Photosensitive Polysilsesquioxane Passivation Layer", Proceedings of The 21st International Workshop on Active-matrix Flat Panel Displays and Devices (AMFPD '14), Kyoto, Japan, July (2014).
5. **Juan Paolo Bermundo**, Yasuaki Ishikawa, Haruka Yamazaki, Toshiaki Nonaka, and Yukiharu Uraoka, " Highly reliable passivation layer for a-InGaZnO thin-film transistors fabricated using polysilsesquioxane", Proceedings of the 2013 Materials Research Society Fall Meeting & Exhibit (MRS Fall 2013), Boston, Massachusetts, USA, December (2013).
6. **Juan Paolo Bermundo**, Yasuaki Ishikawa, Haruka Yamazaki, Toshiaki Nonaka, and Yukiharu Uraoka, "Highly stable a-InGaZnO thin film transistors passivated by polysilsesquioxane-based passivation layer", GIST-NCTU-NAIST International Joint

Symposium 2013 (GNN 2013), Nara, Japan, November (2013). **[Best Poster Award]**

7. **Juan Paolo Bermundo**, Yasuaki Ishikawa, Haruka Yamazaki, Toshiaki Nonaka, and Yukiharu Uraoka, "Effect of reactive ion etching and post-annealing conditions on the characteristics and reliability of a-InGaZnO thin-film transistors with polysilsesquioxane based passivation layer", Proceedings of The 13th International Meeting on Information Display (IMID 2013), Daegu, Korea, August (2013)
8. **Juan Paolo Bermundo**, Yasuaki Ishikawa, Haruka Yamazaki, Toshiaki Nonaka, and Yukiharu Uraoka, "Reliability of Amorphous InGaZnO Thin-Film Transistors Passivated by Polysilsesquioxane-Based Passivation Layer", Proceedings of The 20th International Workshop on Active-matrix Flat Panel Displays and Devices (AM-FPD '13), Kyoto, Japan, July (2013)
9. **Juan Paolo Bermundo**, Yasuaki Ishikawa, Haruka Yamazaki, Toshiaki Nonaka, and Yukiharu Uraoka, "Influence of Polysilsesquioxane-based Passivation Layer on the Electrical Characteristics and Stability of *a*-IGZO thin film transistors", The 9th International Thin-Film Transistor Conference (ITC 2013), Tokyo, Japan, March (2013)

B. Presentations at domestic conference

1. **Juan Paolo Bermundo**, Yasuaki Ishikawa, Mami N. Fujii, Michiel van der Zwan, Hiroshi Ikenoue, Ryoichi Ishihara, Toshiaki Nonaka, and Yukiharu Uraoka, " Low temperature excimer laser annealing of a-InGaZnO thin-film transistors passivated by hybrid organic-inorganic passivation layer", The 62nd Japan Society of Applied Physics Spring Meeting 2015 (JSAP Spring 2015), Kanagawa, Japan, March (2015)
2. **Juan Paolo Bermundo**, Yasuaki Ishikawa, Haruka Yamazaki, Kulchaisit Chaiyanan,

Mami Fujii, Toshiaki Nonaka, and Yukiharu Uraoka, " Suppression of hump effect in a-InGaZnO thin-film transistors passivated by novel photosensitive passivation layer", The 75th Japan Society of Applied Physics Autumn Meeting (JSAP Autumn 2014), Hokkaido, Japan, September (2014)

3. **Juan Paolo Bermundo**, Yasuaki Ishikawa, Haruka Yamazaki, Toshiaki Nonaka, and Yukiharu Uraoka, " Effect of polysilsesquioxane passivation layer on the dark and illuminated negative bias stress of amorphous InGaZnO thin-film transistors", The 60th Japan Society of Applied Physics Spring Meeting (JSAP Spring 2013), Kanagawa, Japan, March (2013)

C. Related presentations

1. Chaiyanan Kulchaisit, Mami N. Fujii, Haruka Yamazaki, **Juan Paolo Bermundo,** Masahiro Horita, Yasuaki Ishikawa, and Yukiharu Uraoka, “Improvement of the Reliability of Bottom Gate Amorphous InGaZnO Thin-Film Transistors with Siloxane Layer”, 11th International Thin-Film Transistor Conference (ITC 2015), Rennes, France, February (2015)
2. Haruka Yamazaki, Yasuaki Ishikawa, Mami N. Fujii, **Juan Paolo Bermundo,** Eiji Takahashi, Yasunori Andoh, and Yukiharu Uraoka, “Chemical Analysis of Fluorine in Highly Reliable Oxide Thin Film Transistor with Silicon Nitride Gate Insulator”, The 21st International Display Workshops (IDW ’14), Niigata, Japan, December (2014).
3. Chaiyanan Kulchaisit, Mami Fujii, Yoshihiro Ueoka, **Juan Paolo Bermundo,** Masahiro Horita, Yasuaki Ishikawa, and Yukiharu Uraoka, “Reliability of Bottom

Gate Amorphous InGaZnO Thin-Film Transistors with Siloxane Passivation Layer", The 2014 International Meeting for Future of Electron Devices Kansai (IMFEDK 2014), Kyoto, Japan, June (2014)

4. Yoshihiro Ueoka, Yasuaki Ishikawa, **Juan Paolo Bermundo,** Haruka Yamazaki, Satoshi Urakawa, Yukihiro Osada, Masahiro Horita, and Yukiharu Uraoka, "Unique property of a-InGaZnO/Ag Interface on Thin-Film Transistor", Proceedings of The 20th International Workshop on Active-Matrix Flatpanel Displays and Devices (AM-FPD'13), Kyoto, Japan, July (2013).

Supplements

A. Parameters for 2D Heat Transfer Simulation by COMSOL MULTIPHYSICS Simulation

Additional details used in the 2D heat simulation such as the waveform (Fig A.1) and variables (Table A.I) are given below. See section 4.4.3 for the in-depth discussion.

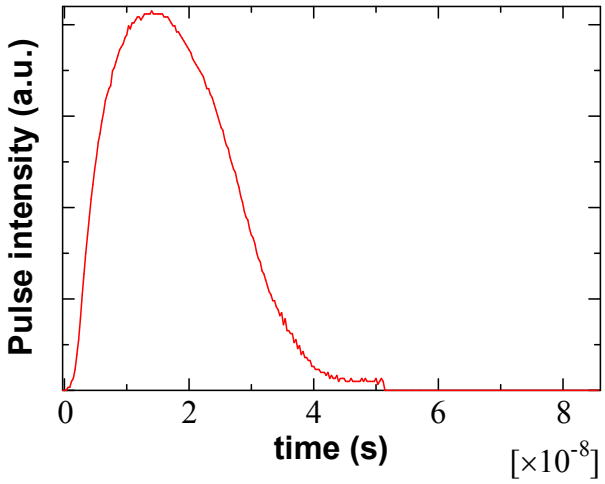

Fig A.1. XeCl waveform, p(t), used in the simulation

Table A.I. Variables used in the 2D heat simulation

	Value	Comments
Wsub	100[um]	Width of substrate
tsub	0.3[um]	thickness of Si substrate
toxide	100[nm]	thickness of SiO_2
tchannel	70[nm]	thickness of IGZO
Wchannel	70[um]	Width of channel
Wsource	20[um]	Width of source
tMo	80[nm]	Mo thickness
tPt	20[nm]	Pt thickness
Elas	0.08[J/cm^2]	laser fluence [joule/cm^2]

T0	273[K]	Substrate temperature
K_IGZO	0.011[W/cm/K]	thermal conductivity of IGZO
C_IGZO	0.44[J/g/K]	specific heat capacity of IGZO
rho_IGZO	6.1[g/cm^3]	mass density of IGZO
alpha_IGZO	1.128e5[1/cm]	absorption of IGZO at 308nm
Ref_IGZO	0.098	Reflectivity of IGZO at 308 nm
alpha_Pt	9.138e5[1/cm]	absorption of Pt
Ref_Pt	0.47	Reflectivity of Pt

Acknowledgements

I have always been fascinated by the Japanese kanji for thank you, 有り難う. The first two kanjis mean “to exist/there is” and the latter two kanjis denote “difficult times”. I have always wondered why the literal meaning has something to do with “difficult to exist” or “having difficulty” until the real meaning and origin of the kanji was explained to me. 有り難う means that because something is “difficult to have” or “special/rare”, we have to appreciate and be thankful for receiving it. In the same light, being given this opportunity to research is special, and for this I am very thankful.

Producing something, much less a thesis, is never done alone. I had a lot of help from many people. First, I would like to express my deepest gratitude to Prof. Yukiharu Uraoka, my principal adviser, for his supervision, kind encouragement, guidance, and for giving me this opportunity. I have always been thankful of being granted this opportunity to do research.

I am also very thankful to Prof. Ichiro Yamashita and Assoc. Prof. Hiroyuki Katsuki for their supervision, valuable advice, suggestions, and critical comments to improve this thesis. I am also deeply indebted to Assoc. Prof. Yasuaki Ishikawa for the valuable discussions, critical advice, suggestions, and helpful comments.

I also very much appreciate the helpful advice and discussions I had with Asst. Prof. Mami N. Fujii. I also express my thanks to Asst. Prof. Masahiro Horita and Asst. Prof. Mutsunori Uenuma for the technical help and advice.

I also sincerely thank Ms. Yukiko Morita for her wonderful support and kindness. I am also very thankful for the technical assistance and advice I received from Mr. Noritake Koike, Mr. Yasuo Okajima, Mr. Shouhei Katao, and Mr. Kazuhiro Miyake.

I want to sincerely thank Assoc. Prof. Ryoichi Ishihara, Ing. Michel van der Zwan,

Ing. Johan van der Cingel, and all the members of the Delft Institute of Microsystems and Microelectronics (DIMES) in Delft University of Technology (Delft, Netherlands) for letting me use the XeCl laser system, the technical assistance, discussions, and for welcoming me during my stay in Delft. I am also very thankful to Assoc. Prof. Hiroshi Ikenoue for the opportunity to use the KrF laser system and the technical assistance.

I am also deeply grateful to Dr. Yoshihiro Ueoka and Ms. Haruka Yamazaki for their introduction and training on device fabrication and for the numerous discussions on thin-film transistors. I am also thankful to Mr. Satoshi Urakawa for the discussions on device physics and the future of devices. I also would like to thank members of the thin-film transistors/film device group, Mr. Yukihiro Osada, Ms. Kahori Kise, Mr. Kulchaisit Chaiyanan, Ms. Hiromi Okada, and Mr. Yang Liu for the helpful discussions. I also thank Mr. Daisuke Hishitani for his assistance on the KrF laser system.

I am also very thankful to my seniors Dr. Emi Machida, Dr. Li Lu, Dr. Yumi Kawamura, Dr. Masahiro Mitani, Dr. Shigekazu Tomai, Dr. Masato Hiramatsu, Dr. Koji Yamasaki, Dr. Satoshi Saijo, and Dr. Takahiko Doe for their helpful advice. I wish to thank Mr. Koji Yoshitsugu, Mr. Hiroki Kamitake, Mr. Takahiko Ban, Mr. Yana Mulyana, Mr. Shinji Araki, Mr. Seiya Yoshinaga, Mr. Keisuke Kado, Mr. Chao He, Mr. Kyohei Nabesaka, and Mr. Yunjian Jiang and all members of the laboratory for their assistance.

I also want to express my deepest gratitude to Dr. Toshiaki Nonaka and his colleagues for the discussions on passivation and providing the precursor materials.

Finally, I am very much thankful to my parents, brothers, friends, and to Jennifer, for their encouragement, understanding, love, and support.

June, 2015

Juan Paolo BERMUNDO